Cell

Article

A fin-loop-like structure in GPX4 underlies neuroprotection from ferroptosis

Graphical abstract

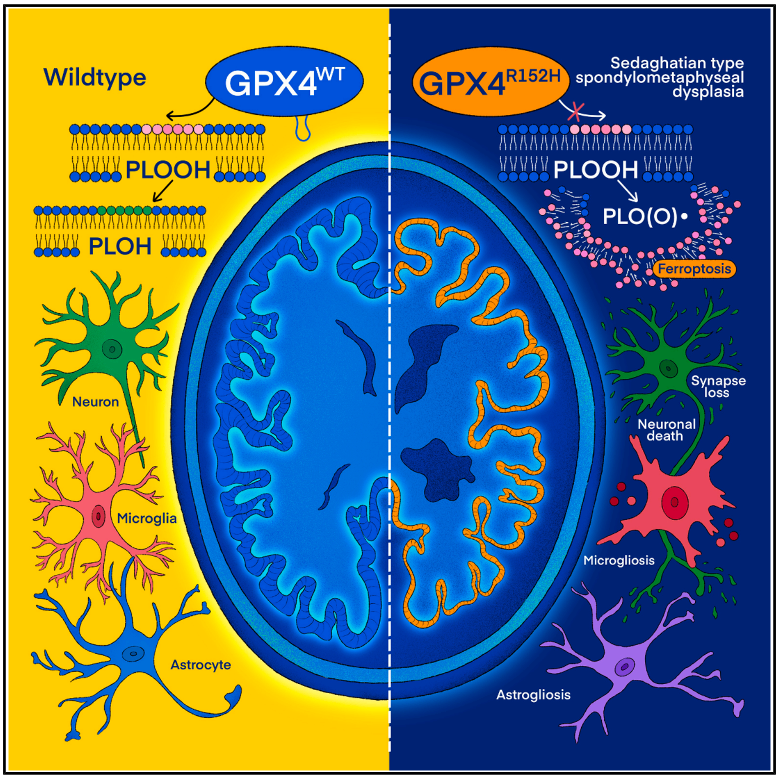

Highlights

- A fin-loop-like structure in GPX4 anchors the enzyme to membranes to block ferroptosis
- The R152H mutation collapses the fin-loop, impairing neuronal protection
- Patient-derived neurons and organoids show ferroptosis-driven degeneration
- Conditional mouse models link GPX4 loss of function to Alzheimer's-like signatures

Authors

Svenja M. Lorenz, Adam Wahida,
Mark J. Bostock, ...,
Ashok Kumar Jayavelu,
Grzegorz M. Popowicz, Marcus Conrad

Correspondence

marcus.conrad@helmholtz-munich.de

In brief

A fin-like structural loop in GPX4 is critical for anchoring the enzyme to cellular membranes, thereby preventing ferroptosis. A patient-associated R152H mutation destabilizes this loop, leading to ferroptotic neurodegeneration in human cells and mouse models and revealing Alzheimer's-like molecular signatures. These findings position ferroptosis as a critical driver (and potential therapeutic target) of neurodegenerative disease.

Lorenz et al., 2026, Cell *189*, 1–20
January 8, 2026 © 2025 The Authors. Published by Elsevier Inc.
https://doi.org/10.1016/j.cell.2025.11.014

CellPress

Please cite this article in press as: Lorenz et al., A fin-loop-like structure in GPX4 underlies neuroprotection from ferroptosis, Cell (2026), https://doi.org/10.1016/j.cell.2025.11.014

Cell

CellPress
OPEN ACCESS

Article

A fin-loop-like structure in GPX4 underlies neuroprotection from ferroptosis

Svenja M. Lorenz,[1,45] Adam Wahida,[1,43,44,45] Mark J. Bostock,[2,3,45] Tobias Seibt,[1,4,45] André Santos Dias Mourão,[2,45] Anastasia Levkina,[1,46] Dietrich Trümbach,[1,46] Mohamed Soudy,[5,46] David Emler,[1,46] Nicola Rothammer,[6] Marcel S. Woo,[6] Jana K. Sonner,[6] Mariia Novikova,[1] Bernhard Henkelmann,[1] Maceler Aldrovandi,[1] Daniel F. Kaemena,[7,8] Eikan Mishima,[1,9] Perrine Vermonden,[1] Zhi Zong,[1] Deng Cheng,[1] Toshitaka Nakamura,[1] Junya Ito,[1,10] Sebastian Doll,[1] Bettina Proneth,[1] Erika Bürkle,[1] Francesca Rizzollo,[11,12] Abril Escamilla Ayala,[13,14] Valeria Napolitano,[2] Marta Kolonko-Adamska,[2] Stefan Gaussmann,[2,3] Juliane Merl-Pham,[15] Stefanie Hauck,[15] Anna Pertek,[16] Tanja Orschmann,[16] Emily van San,[17] Tom Vanden Berghe,[17] Daniela Hass,[18] Adriano Maida,[18] Joris M. Frenz,[19] Lohans Pedrera,[20,21]

(Author list continued on next page)

[1]Institute of Metabolism and Cell Death, Helmholtz Zentrum München, Neuherberg, Germany
[2]Institute of Structural Biology, Molecular Targets and Therapeutics Center, Helmholtz Munich, Neuherberg, Germany
[3]Bavarian NMR Center and Department of Bioscience, TUM School of Natural Sciences, Technical University of Munich, Garching, Germany
[4]Transplant Center, LMU University Hospital, LMU Munich, Munich, Germany
[5]Centre for Systems Biomedicine (LCSB), University of Luxembourg, Esch-sur-Alzette, Luxembourg
[6]Institute of Neuroimmunology and Multiple Sclerosis, University Medical Center Hamburg-Eppendorf, Hamburg, Germany
[7]Institute of Virology, Helmholtz Zentrum München, Neuherberg, Germany
[8]Institute of Virology, School of Medicine, Technical University of Munich, Munich, Germany
[9]Department of Redox Molecular Medicine, Tohoku University Graduate School of Medicine, Sendai, Japan
[10]Laboratory of Food Function Analysis, Tohoku University Graduate School of Agricultural Science, Sendai, Japan
[11]Cell Death Research and Therapy Group, Department of Cellular and Molecular Medicine, KU Leuven, Leuven, Belgium
[12]VIB-KU Leuven Center for Cancer Biology Research, Leuven, Belgium
[13]VIB-KU Leuven Center for Brain & Disease Research, Light Microscopy Expertise Unit & VIB BioImaging Core, Leuven, Belgium
[14]KU Leuven Department of Neurosciences, Leuven Brain Institute, Leuven, Belgium
[15]Metabolomics and Proteomics Core Facility, Helmholtz Zentrum München, Neuherberg, Germany
[16]iPSC Core Facility, Helmholtz Zentrum München, Neuherberg, Germany
[17]Department of Biomedical Sciences, University of Antwerp, Antwerp, Belgium
[18]Institute for Diabetes and Cancer, Helmholtz Zentrum München, Neuherberg, Germany
[19]Clinical Cooperation Unit Pediatric Leukemia, DKFZ and Department of Pediatric Oncology, Hematology and Immunology, University of Heidelberg, Heidelberg, Germany
[20]Institute for Genetics, University of Cologne, Cologne, Germany
[21]CECAD Cluster of Excellence, University of Cologne, Cologne, Germany
[22]Department of Molecular Neurobiology, Groningen Institute for Evolutionary Life Sciences, University of Groningen, Groningen, the Netherlands
[23]Institute of Experimental Genetics and German Mouse Clinic, Helmholtz Zentrum München, German Research Center for Environmental Health, Neuherberg, Germany
[24]Experimental Genetics, TUM School of Life Sciences, Technische Universität München, Freising, Germany
[25]German Center for Diabetes Research (DZD), Neuherberg, Germany
[26]Department of Pediatrics, Division of Genetics, University of California, San Diego and Rady Children's Hospital, San Diego, San Diego, CA, USA
[27]Rady Children's Institute for Genomic Medicine, San Diego, CA, USA
[28]Department of Pediatric Radiology, Institute of Radiology, Charité – Universitätsmedizin Berlin, Freie Universität Berlin and Humboldt-Universität, Berlin, Germany
[29]Institute of Developmental Genetics, Helmholtz Zentrum München, Neuherberg, Germany
[30]TUM School of Life Sciences, Technische Universität München, Freising-Weihenstephan, Germany
[31]Department of Neurology, Ulm University, Ulm, Germany

(Affiliations continued on next page)

SUMMARY

Ferroptosis, driven by uncontrolled peroxidation of membrane phospholipids, is distinct from other cell death modalities because it lacks an initiating signal and is surveilled by endogenous antioxidant defenses. Glutathione peroxidase 4 (GPX4) is the guardian of ferroptosis, although its membrane-protective function remains poorly understood. Here, structural and functional analyses of a missense mutation in GPX4 (p.R152H), which

Please cite this article in press as: Lorenz et al., A fin-loop-like structure in GPX4 underlies neuroprotection from ferroptosis, Cell (2026), https://doi.org/10.1016/j.cell.2025.11.014

Amalia Dolga,[22] Markus Kraiger,[23] Martin Hrabé de Angelis,[23,24,25] Helmut Fuchs,[23] Gregor Ebert,[7,8] Jerica Lenberg,[26,27] Jennifer Friedman,[26,27] Carolin Scale,[28] Patrizia Agostinis,[11,12] Annemarie Zimprich,[23,29] Daniela Vogt-Weisenhorn,[29] Lillian Garrett,[23,29] Sabine M. Hölter,[23,29] Wolfgang Wurst,[29,30] Enrico Glaab,[5] Jan Lewerenz,[31] Bastian Popper,[32] Christian Sieben,[33] Petra Steinacker,[31,34] Hans Zischka,[35,36] Ana J. Garcia-Saez,[20,21] Anna Tietze,[37] Sanath Kumar Ramesh,[38] Scott Ayton,[39] Michelle Vincendeau,[7,8] Manuel A. Friese,[6] Kristen Wigby,[26,27] Michael Sattler,[2,3] Matthias Mann,[40] Irina Ingold,[1] Ashok Kumar Jayavelu,[19,40,41] Grzegorz M. Popowicz,[2,47] and Marcus Conrad[1,42,47,48,*]

[32]Biomedical Center, Core Facility Animal Models, Medical Faculty, LMU Munich, Martinsried, Germany
[33]Nanoscale Infection Biology Group, Helmholtz Centre for Infection Research, Braunschweig, Germany
[34]Department of Neurology, Martin-Luther-University of Halle-Wittenberg, Halle, Germany
[35]Institute of Molecular Toxicology and Pharmacology, Helmholtz Munich, German Research Center for Environmental Health, Neuherberg, Germany
[36]Institute of Toxicology and Environmental Hygiene, TUM School of Medicine and Health, Technical University of Munich, Munich, Germany
[37]Institute of Neuroradiology, Charité – Universitätsmedizin Berlin, Freie Universität Berlin and Humboldt-Universität zu Berlin, Berlin, Germany
[38]CureGPX4.org, Seattle, WA, USA
[39]Florey Institute of Neuroscience and Mental Health, University of Melbourne, Parkville, MEL, Australia
[40]Department of Proteomics and Signal Transduction, Max Planck Institute of Biochemistry, Martinsried, Germany
[41]Hopp Children's Cancer Center Heidelberg KiTZ, Heidelberg, Germany
[42]Translational Redox Biology, TUM Natural School of Sciences, Technical University of Munich, Garching, Germany
[43]Molecular Signaling and Cell Death Unit, VIB-UGent Center for Inflammation Research, Flanders Institute for Biotechnology, Ghent, Belgium
[44]Department of Biomedical Molecular Biology, Ghent University, Ghent, Belgium
[45]These authors contributed equally
[46]These authors contributed equally
[47]Senior author
[48]Lead contact
*Correspondence: marcus.conrad@helmholtz-munich.de

https://doi.org/10.1016/j.cell.2025.11.014

causes early-onset neurodegeneration, revealed that this variant disrupts membrane anchoring without considerably impairing its catalytic activity. Spatiotemporal *Gpx4* deletion or neuron-specific GPX4^{R152H} expression in mice induced degeneration of cortical and cerebellar neurons, accompanied by progressive neuroinflammation. Patient induced pluripotent stem cell (iPSC)-derived cortical neurons and forebrain organoids displayed increased ferroptotic vulnerability, mirroring key pathological features, and were sensitive to ferroptosis inhibition. Neuroproteomics revealed Alzheimer's-like signatures in affected brains. These findings highlight the necessity of proper GPX4 membrane anchoring, establish ferroptosis as a key driver of neurodegeneration, and provide the rationale for targeting ferroptosis as a therapeutic strategy in neurodegenerative disease.

INTRODUCTION

The progressive loss of neurons is a recurring feature of neurodegenerative diseases, a diverse group of disorders characterized by cognitive decline, motor impairment, and, in many cases, premature death.[1–4] Although neuronal death is a shared endpoint, each neurodegenerative condition presents with distinct pathological hallmarks, many of which have been proposed as causal drivers and therapeutic targets.[4] Over the past few decades, genome-wide association studies (GWASs) have identified genetic susceptibilities associated with these diseases. These, in turn, have served as the rationale for broad efforts to match molecular mechanisms with precision therapeutic strategies.[1,5–8] But despite these insights, neuronal loss, the most salient feature, remains insufficiently explained, particularly with respect to the upstream pathways that drive cell death.[9,10] Because a mechanistic understanding of how neurons die and the downstream consequences of this process are critical for rational intervention in most neurodegenerative diseases, this lack of knowledge remains a major barrier to the development of effective therapies.

Genome-wide sequencing efforts, on the other hand, have accelerated the discovery of rare, deleterious, and highly penetrant variants in children with syndromic presentations, offering a direct route to infer gene function from human pathology.[11] One example involves glutathione peroxidase 4 (GPX4), a selenoenzyme now recognized as the central regulator of ferroptosis, a non-apoptotic, iron-dependent form of cell death implicated in diverse diseases.[12–18] As such, pathogenic variants in GPX4 have been linked to Sedaghatian-type spondylometaphyseal dysplasia (SSMD), an ultra-rare autosomal recessive disorder characterized by severe neurodegeneration and skeletal abnormalities.[19] Since its first clinical account in 1980,[20] only a handful of SSMD cases have been reported, all converging on mutations in *GPX4* and highlighting the indispensable role of ferroptosis surveillance in maintaining neuronal integrity.[21]

RESULTS

The GPX4^{R152H} allele triggers ferroptosis

SSMD (OMIM #250220) is an ultra-rare and typically lethal disorder characterized by severe chondrodysplasia, delayed

Please cite this article in press as: Lorenz et al., A fin-loop-like structure in GPX4 underlies neuroprotection from ferroptosis, Cell (2026), https://doi.org/10.1016/j.cell.2025.11.014

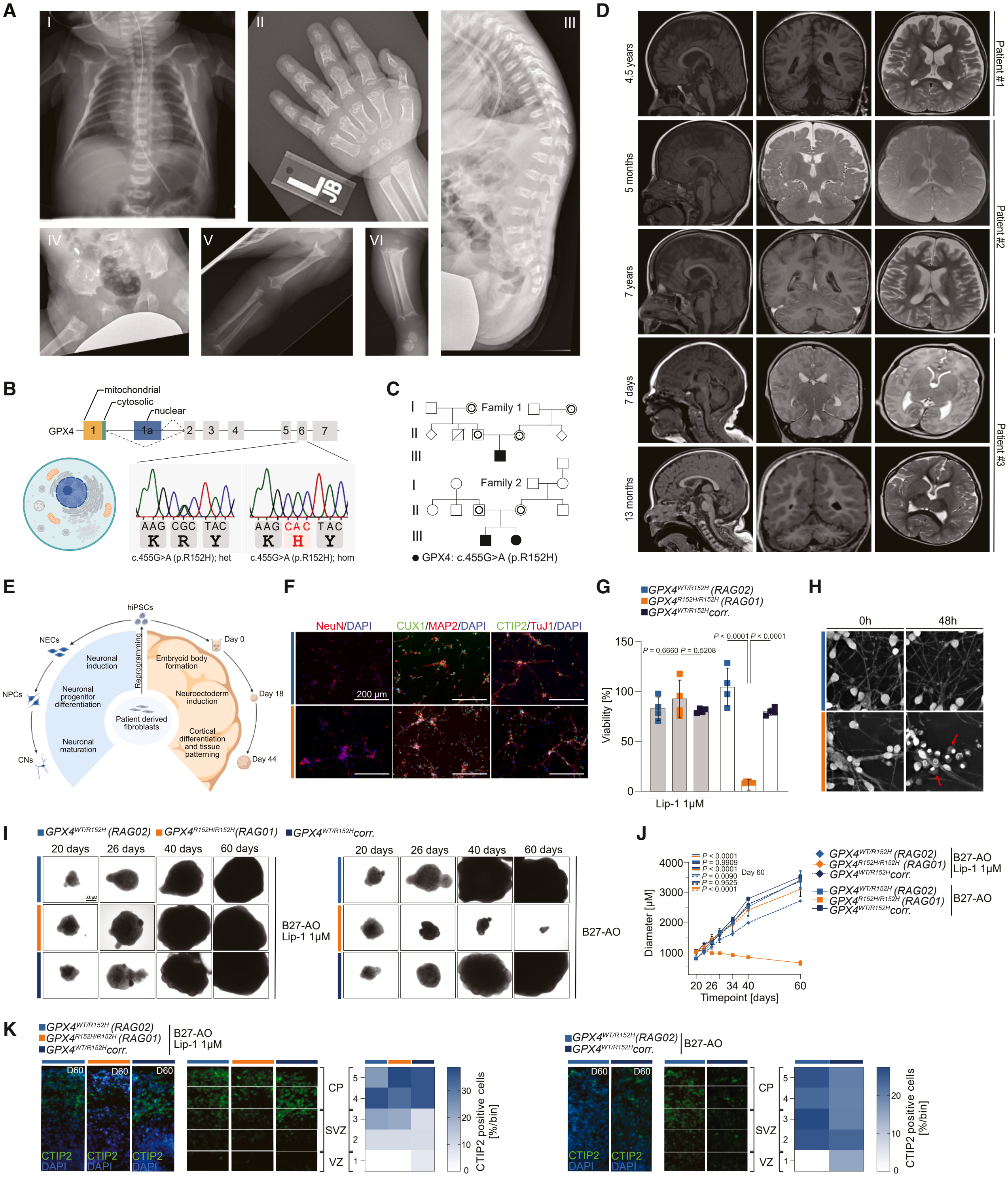

Figure 1. The GPX4^{R152H} allele triggers ferroptosis

(A) X-ray analyses of patient #3. Small thorax and squaring of the inferior scapulae (I); shortening and widening of the metacarpals and phalanges (II); platyspondyly and increased intervertebral spaces (III); flat acetabular roof, small iliac wings, and irregular iliac crests (IV); disproportional long fibulas (V); and irregular metaphyses with cupping of all extremity bones (V/VI).

(B) Gene map of *GPX4* depicting genetic localization of the R152H missense variant as detected by NGS and confirmed through Sanger sequencing of primary cells of patient #3 and his heterozygous parent, of which the chromatograms of the affected alleles are displayed (see STAR Methods for genotyping primer).

(legend continued on next page)

epiphyseal ossification, and irregular iliac crests (Figure 1A).[19] In most cases, infants with SSMD present with severe hypotonia and cardiorespiratory problems, leading to early postnatal death.[19] Notably, these patients suffer from severe central nervous system (CNS) defects, encompassing mental, behavioral, and motor impairment.[19,20] Although several loss-of-function mutations in GPX4 have been reported, the identification of a missense variant (c.455G>A; p.R152H) (Figure 1B) in three patients from two unrelated families (Figure 1C), each presenting with a protracted hypomorphic disease course, provided an opportunity to investigate ferroptosis-driven disease in humans.[22] Radiographic evaluation revealed a constellation of skeletal abnormalities characteristic of SSMD, including irregular metaphyses with cupping of all long bones, squaring of the inferior scapulae, mild rhizomelia, disproportionately elongated fibulas, and shortening and widening of the metacarpals and phalanges. Additional features included flat acetabular roofs, small iliac wings, irregular iliac crests, platyspondyly, widened intervertebral spaces, and a relatively small thoracic cage (Figure 1A).

Notably, we assessed neuroanatomical involvement beyond these disease-defining skeletal features using magnetic resonance imaging (MRI) (Figure 1D). All patients exhibited cerebellar atrophy of variable severity, and in two of the three children, supratentorial cortical atrophy was also observed. Myelination was appropriate for age in all cases, and no major cerebral malformations were detected. The progressive nature of neurodegeneration during childhood argued against a primary developmental defect but in favor of an ongoing degenerative process in homozygous *Gpx4*^{R152H} carriers. This resulting strict requirement for homozygosity to manifest with SSMD symptoms reinforced the notion of pathogenicity of the R152H variant, albeit milder than that associated with biallelic truncating *Gpx4* mutations,[19] yet consistent with a hypomorphic allele retaining partial function. These findings suggested that R152H strongly impairs, but does not fully abrogate, GPX4 function, potentially unveiling previously unrecognized mechanisms of GPX4 regulation. Thus, although the syndromology resembled SSMD, it remained unresolved whether the R152H variant alone was sufficient to cause disease and, equally important, whether the homozygous *Gpx4*^{R152H} genotype could trigger ferroptosis in neurons.

To dissect the functional consequences of *Gpx4*^{R152H} carriership, we first employed a series of *in vitro* models derived from primary fibroblasts from one homozygous patient and his heterozygous father. Only patient-derived fibroblasts carrying homozygous *Gpx4*^{R152H} (RAG01) exhibited rapid cell death with characteristic ferroptotic morphology, unless rescued by radical-trapping antioxidants (RTAs) such as Trolox (Figure S1A), a water-soluble vitamin E analog, or liproxstatin-1 (Lip-1),[14] a bona fide ferroptosis inhibitor (Figure S1B). Dying cells exhibited pronounced membrane damage (Figure S1C) and elevated lipid peroxidation, as measured by BODIPY 581/591 C11 (Figure S1D) staining, despite unaltered GPX4 expression (Figure S1E) and catalytic activity (Figure S1F). In contrast, fibroblasts derived from the heterozygous father (*GPX4*$^{WT/R152H}$; RAG02) were resistant against washout of Trolox (Figure S1A) or Lip-1 (Figure S1B).

To study the neuronal vulnerability of the R152H variant, these fibroblasts were first reprogrammed into human induced pluripotent stem cells (hiPSCs) (Figure 1E). Both heterozygous (*GPX4*$^{WT/R152H}$) and homozygous (*GPX4*$^{R152H/R152H}$) hiPSC lines exhibited comparable reprogramming efficiencies and pluripotency, as indicated by the expression of octamer-binding protein 4 (OCT4), SRY-box transcription factor 2 (SOX2), Lin-28 homolog A (LIN28), and NANOG expression (Figure S1G). Next, we stepwise directed hiPSC lines via neuronal progenitor cells (NPCs) to cerebral cortical neurons (CNs) (Figure 1E), as confirmed by expression of neuronal identity markers CTIP2

(C) The pedigrees of both affected families depict the carrier status of the R152H allele. Roman lettering denotes generational transmittance of the respective allele.

(D) T1- and T2-weighted magnetic resonance images (MRI) of three affected patients carrying a deleterious mutation in GPX4, displaying progressive cerebellar atrophy of varying degrees in all three patients, as well as atrophy of the supratentorial parenchyma in patients #1 and #2. The figure denotes the respective ages of diagnostic interventions at the corresponding patient's age.

(E) Graphical representation of the generation of cortical neurons derived from human induced pluripotent stem cells (hiPSCs) from patient-derived RAG01 and RAG02 cells, as well as a workflow depicting the generation of forebrain organoids thereof.

(F) Immunofluorescent staining of cortical neurons (CNs) from *GPX4*$^{WT/R152H}$ (RAG02) and G*PX4*$^{R152H/R152H}$ (RAG01) for CTIP2 (BCL11 transcription factor B), cut-like homeobox 1 (CUX1), TuJ1 (neuron-specific class III β-tubulin), microtubule-associated protein 2 (MAP2), and neuronal nuclei (NeuN), verifying expression of neuronal identity markers (see STAR Methods for staining and analysis methods of this sample). Scale bar indicates 200 μm.

(G) Viability as measured with or without Lip-1 (1 μM) from CNs derived from heterozygous mutant *GPX4*$^{WT/R152H}$ (RAG02) hiPSCs, mutant *GPX4*$^{R152H/R152H}$ (RAG01) hiPSCs, or *GPX4*$^{WT/R152H}$*corr*. hiPSCs. Results represent at least three independent experiments, and statistical analysis was performed using a two-way ANOVA and post hoc analysis using Tukey's test. Shaded colors indicated treatment with Lip-1, as indicated in the figure caption.

(H) Representative live-cell imaging recordings from heterozygous *GPX4*$^{WT/R152H}$ (RAG02) and homozygous *GPX4*$^{R152H/R152H}$ (RAG01) hiPSCs. After 48 h of incubation without Lip-1, *GPX4*$^{R152H/R152H}$ CNs undergo cell death.

(I) Bright-field images of forebrain organoids derived from heterozygous *GPX4*$^{WT/R152H}$ (RAG02), homozygous *GPX4*$^{R152H/R152H}$ (RAG01), and *GPX4*$^{WT/R152H}$*corr*. hiPSCs. *GPX4*$^{R152H/R152H}$ organoids started showing signs of degeneration from day 26, followed by complete death until day 60, when cultured without Lip-1 supplementation (right). Scale bar indicates 500 μm.

(J) Diameter changes of forebrain organoids derived from heterozygous *GPX4*$^{WT/R152H}$ (RAG02) and homozygous *GPX4*$^{R152H/R152H}$ (RAG01) hiPSCs show signs of degeneration of mutant *GPX4*$^{R152H/R152H}$ without Lip-1 supplementation, as evidenced by significant diameter reduction. Statistical analysis was performed using a two-way ANOVA and post hoc analysis using Tukey's test.

(K) Left: immunofluorescent stainings of CTIP2 of *GPX4*$^{WT/R152H}$ (RAG02), *GPX4*$^{R152H/R152H}$ (RAG01), and *GPX4*$^{WT/R152H}$*corr*. forebrain organoids (day 60) verified cortical layer formation in all samples cultured in B27-AO with Lip-1 supplementation (left) and show distribution along five bins, with bin 1 representing the ventricular zone (VZ), bins 2–3 the subventricular zone (SVZ), and bins 4–5 the cortical plate (CP). Right: immunofluorescent stainings of CTIP2 of *GPX4*$^{WT/R152H}$ (RAG02) and *GPX4*$^{WT/R152H}$*corr*. forebrain organoids (day 60) verified cortical layer formation in both samples cultured in B27-AO without Lip-1 supplementation (left) and show distribution along five bins, with bin 1 representing the VZ, bins 2–3 the SVZ, and bins 4–5 the CP.

See also Figures S1–S3.

(BCL11 transcription factor B), CUX1 (cut-like homeobox 1), neuron-specific class III β-tubulin (TuJ1), microtubule-associated protein 2 (MAP2) and neuronal nuclei (NeuN) (Figure 1F). Akin to the findings in fibroblasts, death of neurons derived from *GPX4*$^{R152H/R152H}$ could be rescued by the ferroptosis inhibitor Lip-1, supporting ferroptosis-driven demise, whereas *GPX4*$^{WT/R152H}$ and the CRISPR-Cas9-corrected control of *GPX4*$^{R152/R152H}$ to *GPX4*$^{WT/WT}$ (*GPX4*$^{R152/WT}$*corr.*) remained unaffected (Figures 1G and 1H; Video S1). These findings establish a patient-derived *in vitro* platform to model ferroptosis-driven neurodegeneration and reveal that the GPX4^{R152H} variant compromises neuronal resilience.

Leveraging this resource, these patient-derived hetero- and homozygous hiPSCs were further used to investigate the impact of the *GPX4*$^{R152H/R152H}$ genotype on forebrain development by performing forebrain organoid differentiation (Figure 1E).[23] During early neuroectodermal induction (days 0–18), Lip-1 was included as an RTA to prevent cell death, allowing for the normal formation of neuroepithelial structures in both genotypes. At day 18, organoids were transferred into a differentiation medium lacking RTA (B27-supplement without antioxidants and Lip-1) to evaluate developmental defects caused by ferroptosis in the *GPX4*$^{R152H/R152H}$ genotype. In the absence of Lip-1, *GPX4*$^{R152H/WT}$ (RAG02) and *GPX4*$^{R152H/WT}$*corr.*, organoids continued to grow and develop into mature forebrain organoids (Figure 1I). In contrast, *GPX4*$^{R152H/R152H}$ (RAG01) organoids failed to thrive under this condition. Instead, these organoids exhibited signs of degeneration by day 26, with complete decomposition and halted growth at days 40–60 (Figure 1J). Notably, supplementation of the medium with Lip-1 rescued this phenotype. Proper cortical layer formation was verified by the expression of CTIP2 (Figure 1K). In line with recent findings, supplementation of RTA affects proper cortical lamination,[24] leading to a disorganized and diffuse distribution of CTIP2$^+$ neurons in *GPX4*$^{R152H/WT}$ organoids cultured without RTA. In the presence of Lip-1, CTIP2$^+$ neurons in all organoids displayed a sharply organized cortical plate (CP). For the quantification of several organoids, we divided the developing cortex into five equal bins,[23,24] with bin 1 representing the ventricular zone (VZ), bins 2–3 the subventricular zone (SVZ), and bins 4–5 the CP. Organoids maintained in Lip-1 medium exhibited a pattern with enriched CTIP2$^+$ neurons in bins 4–5, reflecting successful cortical lamination (Figure 1K).

Having established its pathogenic effect *in vitro* by triggering ferroptosis, we next sought to study the pathological underpinnings of the GPX4^{R152H} variant causing SSMD *in vivo*. To this end, we generated transgenic mice carrying the identical variant in the murine ortholog *Gpx4* (*Gpx4*$^{R152H/WT}$) (Figure S2A). However, intercross of *Gpx4*$^{R152H/WT}$ mice did not yield viable *Gpx4*$^{R152H/R152H}$ offspring, indicating embryonic lethality of *Gpx4*$^{R152H/R152H}$ mice (Figures S2B and S2C). Analyzing embryos dissected from heterozygous *Gpx4*$^{R152H/WT}$ breedings at different gestational days revealed that homozygous *Gpx4*$^{R152H/R152H}$ embryos die during gastrulation (E7.5) (Figure S2B), in analogy to homozygous *Gpx4*$^{-/-}$ embryos.[13,25] To exclude strain-dependent effects (as observed earlier for a mouse line expressing a homozygous *Gpx4*$^{U46C/U46C}$ allele[21]), we crossed knockin mice from the C57BL/6J background on the 129S2/SvPasCrl strain (F1), which yielded the same phenotype, indicating that the observed lethality is unrelated to genetic background (Figure S2D). Thus, considering that SSMD patients carrying the *GPX4*^{R152H} variant are born, we hypothesize the presence of still-unidentified compensatory programs or suppressor genes in humans, enabling the survival of homozygous *GPX4*^{R152H} individuals.

Due to the early embryonic lethal phenotype of *Gpx4*$^{R152H/R152H}$ mice, this model was not helpful for further in-depth investigations on the pathophysiological effects of the R152H variant. To bypass embryonic lethality, *Gpx4*$^{R152H/WT}$ mice were crossbred with whole-body tamoxifen (TAM)-inducible *Gpx4*$^{fl/fl}$ *Rosa26CreER*$^{T2+/tg}$ mice to generate *Gpx4*$^{R152H/fl}$*Rosa26 CreER*$^{T2+/tg}$ mice (Figure S2E).[14] Previously, we showed that TAM-inducible GPX4 null mice develop acute renal failure and die around 10–12 days after TAM administration due to widespread ferroptosis of renal proximal tubule epithelial cells.[14] Treatment of *Gpx4*$^{R152H/fl}$*Rosa26CreER*$^{T2+/tg}$ mice with TAM caused the same pathophysiological phenotype as in *Gpx4*$^{fl/fl}$*Rosa26-CreER*$^{T2+/tg}$ mice (Figures S2F–S2J). This included widespread cell death of renal tubular epithelial cells, as indicated by positive signals for TUNEL (terminal deoxynucleotidyl transferase dUTP nick-end labeling) and the kidney damage marker kidney injury molecule-1 (KIM-1), as well as positive staining for the lipid peroxidation breakdown marker 4-hydroxynonenal (4-HNE) (Figure S2G). This phenotype was accompanied by serum chemistry analyses indicating renal damage (Figure S2H), as well as body weight loss (Figure S2I), and early death of mice (Figure S2J).

To corroborate the ferroptotic origin of tissue damage due to the GPX4^{R152H} genotype, we performed (oxy)lipidomics analysis to detect oxidized phospholipids (Figure S2L; Table S1, sheet 1), which, by definition, precede ferroptosis.[14,26,27] Indeed, liquid chromatography-tandem mass spectrometry (LC-MS/MS) analysis revealed the presence of numerous oxidized phospholipid species, primarily long-chain phosphatidylethanolamines containing multiple isomers of oxidized arachidonic acid (20:4), docosahexaenoic acid (22:6), and linoleic acid (18:2). These results resemble those observed during either genetic deletion or pharmacological inhibition of GPX4.[27,28] In summary, these data show that the R152H variant does not compensate for the loss of wild-type (WT) GPX4 *in vitro* and *in vivo*.

GPX4^{R152H} is associated with the collapse of a hydrophobic finloop

Although our findings indicate that the R152H variant cannot compensate for the loss of the WT *Gpx4* allele *in vivo*, despite preserved mRNA and protein expression, it plausibly explains ferroptosis in previously reported truncating SSMD variants. Immunoblot analysis confirmed that, although truncating mutations abolished GPX4 protein expression, the R152H variant was stably expressed at levels comparable to WT (Figure S3A) but did not rescue ferroptosis (Figures S3C–S3F). To test whether the lack of rescue was due to increased protein instability, we performed a cycloheximide chase assay in the presence of (1*S*,3*R*)-RSL3 (RSL3), a covalent inhibitor of GPX4 (Figure S3B). No significant differences in degradation kinetics were observed between WT and GPX4^{R152H}, suggesting that the pathogenicity of the missense variant is not due to altered

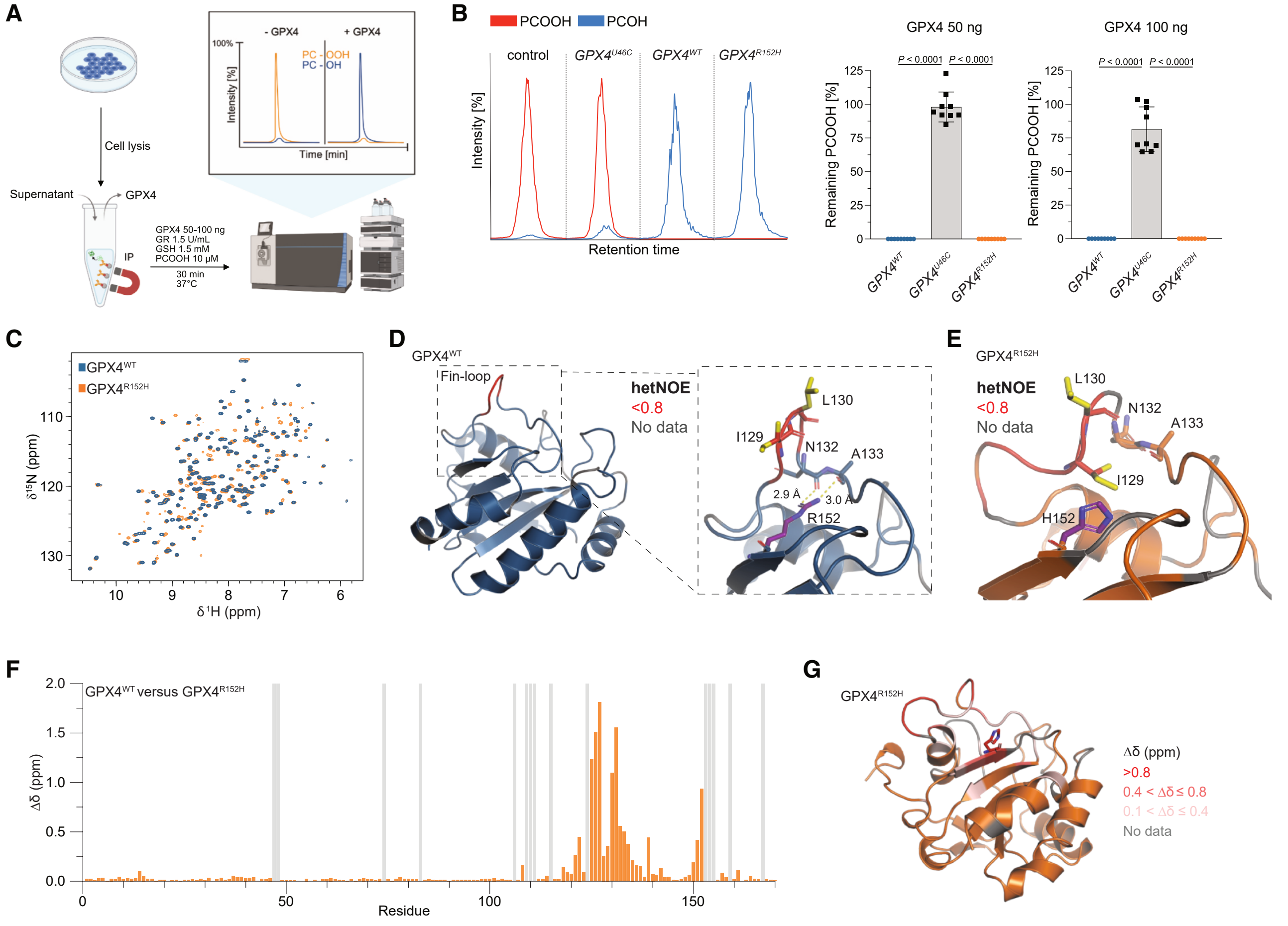

Figure 2. GPX4^{R152H} is associated with the collapse of a hydrophobic fin-loop

(A) Graphical abstract depicting the workflow of the activity measurement of GPX4 and mutants according to Nakamura et al.[29]

(B) LC-MS/MS intensity peaks and normalized quantification of remaining PCOOH and PCOH in the activity reaction mix without enzymes (control) and in the presence of GPX4^{U46C}, GPX4^{WT}, and GPX4^{R152H} enzymes. Mutant GPX4^{R152H} shows the same PCOOH-reducing activity as GPX4^{WT} control. Results are representative of three independent experiments, and statistical analysis was performed using a one-way ANOVA and post hoc analysis using Tukey's test.

(C) Overlay of ^{1}H-^{15}N HSQC spectra for GPX4^{WT} and GPX4^{R152H}.

(D) {^{1}H}-^{15}N Heteronuclear NOE data are plotted on the GPX4^{WT} crystal structure (PDB: 2OBI[32]). Residues with a heteronuclear NOE value < 0.8 (Figure S5A) are shown in red and indicate that the polypeptide backbone of the fin-loop in GPX4^{WT} shows fast ps-ns timescale motions. The zoom region shows the interaction of the Arg152 guanidino side chain (purple) with the backbone of Asn132 and Ala133 (sticks) in GPX4^{WT}. This interaction helps stabilize the fin-loop.

(E) {^{1}H}-^{15}N Heteronuclear NOE data are plotted on the crystal structure of GPX4^{R152H}. Residues with a heteronuclear NOE value < 0.8 (Figure S5B) are shown in red and indicate that the polypeptide backbone of the fin-loop shows fast ps-ns timescale motions in GPX4^{R152H}. Mutation of Arg152 to His leads to loss of stabilization of the fin-loop, with the side chain of I129 occupying the space where, in GPX4^{WT}, R152 forms side-chain-to-backbone hydrogen bonds with Asn132 and Ala133.

(F) Chemical shift perturbations (CSPs), Δδ, for backbone amide residues of GPX4^{WT} and GPX4^{R152H}. Gray bars indicate unassigned residues.

(G) Significant amide CSPs (Δδ) for backbone amides of residues in GPX4^{WT} and GPX4^{R152H} from (F) are plotted on the GPX4^{R152H} crystal structure.

See also Figures S4–S6.

protein stability but instead arises from a distinct functional impairment.

To directly assess the catalytic function of disease-relevant GPX4 variants, we implemented a refined enzyme activity assay based on native, affinity-purified GPX4 from mammalian cells (Figure 2A).[29] This approach circumvents key limitations of conventional assays, which did not indicate altered activity of the GPX4^{R152H} variant in cells or tissue (Figures S1F and S2K), including non-specific background from whole-cell lysates and potential artifacts from bacterial GPX4 expression systems, often yielding dysfunctional protein. Hence, using LC-MS/MS-based quantification of lipid peroxide reduction, we incubated affinity-purified GPX4^{WT}, GPX4^{R152H}, or the GPX4^{U46C} variant (as a control) with phosphatidylcholine hydroperoxide (PCOOH),[30,31] the physiological substrate of GPX4. Thus, we monitored the conversion of 1-palmitoyl-2-13(S)-hydroperoxyoctadecadienoyl-*sn*-glycero-3-phosphocholine (PCOOH, 10 µM) to 1-palmitoyl-2-13(S)-hydroxyoctadecadienoyl-*sn*-glycero-3-phosphocholine (PCOH) by GPX4 (50 or 100 ng) (Figure 2B). Strikingly, the GPX4^{R152H} variant exhibited enzymatic activity similarly to WT,

Please cite this article in press as: Lorenz et al., A fin-loop-like structure in GPX4 underlies neuroprotection from ferroptosis, Cell (2026), https://doi.org/10.1016/j.cell.2025.11.014

indicating that its pathogenicity does not stem from impaired catalysis.

Because WT and GPX4^{R152H} displayed comparable expression, protein stability, and enzyme activity, we then asked whether structural changes in the GPX4^{R152H} mutant could account for the lack of its anti-ferroptotic function. To this end, we expressed and purified GPX4^{WT} and its mutant counterpart (both with the catalytic selenocysteine mutated to cysteine, U46C, in *Escherichia coli* [*E. coli*] for higher yields). 2D ^{1}H,^{15}N solution NMR spectra for GPX4^{WT} and GPX4^{R152H} showed well-dispersed peaks for both variants (Figures 2C, S4A, and S4B), indicating that the mutant protein is well folded and both variants do not differ regarding global conformational changes. Next, backbone NMR chemical shifts of GPX4^{WT} and GPX4^{R152H} were assigned, and {^{1}H}-^{15}N heteronuclear NOE (hetNOE) relaxation data were acquired to measure fast ps-ns timescale motions. Both constructs showed comparable hetNOE values > 0.8, consistent with a well-structured protein and comparable to previously reported data for GPX4^{U46C} (Figures 2D, 2E, S5A, and S5B).[33] Lower hetNOE values (<0.8) around residue 130 indicated a more flexible region (with fast ps-ns timescale motions), mapping to a hydrophobic patch and loop on the crystal structure, which is slightly reduced for GPX4^{R152H}, suggesting moderately increased loop flexibility (Figures 2D, 2E, S5A, and S5B). Chemical shift perturbations (CSPs) were calculated between the GPX4^{WT} and GPX4^{R152H} spectra (Figure 2F) and plotted on the GPX4^{R152H} structure (Figure 2G), confirming that the spectral changes mapped primarily to the hydrophobic patch and loop region around residue 130 (Figures 2F, 2G, and S4B). At the same time, the rest of the protein is unperturbed. Due to the appearance of this loop region protruding from the surface of the protein, akin to a surfboard fin, we nickname this the "fin-loop" (Figure 2D). A previous study of GPX4^{R152H} postulated a destabilizing effect of the mutation on the fin-loop.[22] We, therefore, solved the crystal structure of the R152H mutant (Figure 2E). The structure shows that the changes in the fin-loop arise from the loss of the sidechain guanidino group of R152, which forms two sidechain-backbone hydrogen bonds with N132 and A133 in the WT at the base of the fin-loop (Figures 2D and 2E). The mutation of arginine to histidine (R152H) breaks this interaction, destabilizing the loop region, which collapses onto the GPX4 core.

Notably, two conserved hydrophobic amino acids (I129 and L130) flanked by G128 and G131, which point out from the loop into the solvent in GPX4^{WT}, exhibit large structural perturbations in GPX4^{R152H}, with I129 filling the space occupied by the R152 side chain in GPX4^{WT} and packing adjacent to the histidine side chain (Figures 2D, 2E, and 3A). Thus, we confirmed that R152 is critical for stabilizing the base of the hydrophobic fin-loop in an extended conformation protruding from the surface of GPX4^{WT} into the solvent. The presence of the highly conserved, solvent-exposed hydrophobic I129 and L130 residues at the tip of the fin-loop is unusual and led us to consider their functional role. As the global structure of GPX4 remained unaffected, and *in vitro* measurements showed that the enzymatic activity was unchanged for GPX4^{R152H}, we concluded that changes to the fin-loop do not impact its activity (Figure 2B). Instead, we hypothesized that, given its pronounced hydrophobicity, the fin-loop mediates proper positioning and localization of GPX4 to membranes.

A hydrophobic fin-loop mediates membrane binding of GPX4

To probe the importance of the fin-loop for membrane targeting, we sought to assess this interaction with membrane-mimicking bicelles. Bicelles are a well-validated tool mimicking the properties of cell membranes, consisting of a central discoidal bilayer region composed of long-chain lipids flanked by shorter-chain lipids.[34,35] GPX4 has previously been shown to interact with micelles and lipid bilayers, including bicelles, with the interaction proposed to occur through a cationic patch.[33,36] We titrated GPX4^{WT} and GPX4^{R152H} with 1,2-dimyristoyl-*sn*-glycero-3-phosphocholine (DMPC):1,2-diheptanoyl-*sn*-glycero-3-phosphocholine (D7PC) bicelles, q = 0.2, recording ^{1}H,^{15}N HSQC spectra. CSP and intensity changes were assessed for 4.3 μM bicelles (0.05×, 200 μM DMPC) and 8.6 μM bicelles (0.1×, 400 μM DMPC) (Figures 3B, S6A, and S6B). CSP changes upon titrating bicelles were minimal for the WT and GPX4^{R152H} constructs, consistent with the low protein:bicelle ratio (Figures S6A and S6B). Plotting the changes for GPX4^{WT} showed that these changes map to the fin-loop region, indicating that this region interacts with the bicelles (Figure S6A). The lack of large-scale CSPs indicates the absence of global structural perturbations in the presence of bicelles. Notably, spectral changes for GPX4^{R152H} were considerably smaller (Figure S6B).

Therefore, we assessed signal intensity changes in the presence of bicelles to assess the line broadening of NMR signals due to interactions with the membrane mimic. A significantly reduced intensity ratio of 0.7 is observed for all residues across the structured core of the protein when comparing conditions ± bicelles for GPX4^{WT} in the presence of 0.05× bicelles (Figures 3B left and 3C). Furthermore, the intensity ratio in the fin-loop region dropped to around 0.2. At 0.1× bicelles, core residues showed an even weaker intensity ratio of around 0.4, while the NMR signals were broadened beyond detection for the fin-loop, and their intensity could not be assessed. These data suggest that the fin-loop mediates the interaction with the bicelles. Because the interaction between GPX4 and bicelles will increase the overall tumbling time of the complex, the intensity of all residues will be affected due to the increased effective correlation time; direct interaction between the fin-loop and bicelles would further decrease the intensity in this region. In this model, only the fin-loop interacts directly with the bicelles, and interactions will be mediated via amino acid sidechains. Therefore, backbone amide CSPs are expected to be small. Compared with GPX4^{WT}, GPX4^{R152H} showed no significant CSPs, and the intensity ratio was approximately 1.0 across all the GPX4^{R152H} amide residues, indicating that GPX4^{R152H} does not interact with the membrane-mimicking bicelles (Figures 3B, middle, and S6B). Hence, these data support our hypothesis that the collapse of the fin-loop abrogates GPX4's interaction with lipid bilayers, akin to cell membranes.

We further hypothesized that, if the key interaction site for GPX4^{WT} with bicelles occurs through the fin-loop, removing hydrophobic residues from this loop would disrupt its interaction, even if the protruding loops' structure were to remain intact.

Please cite this article in press as: Lorenz et al., A fin-loop-like structure in GPX4 underlies neuroprotection from ferroptosis, Cell (2026), https://doi.org/10.1016/j.cell.2025.11.014

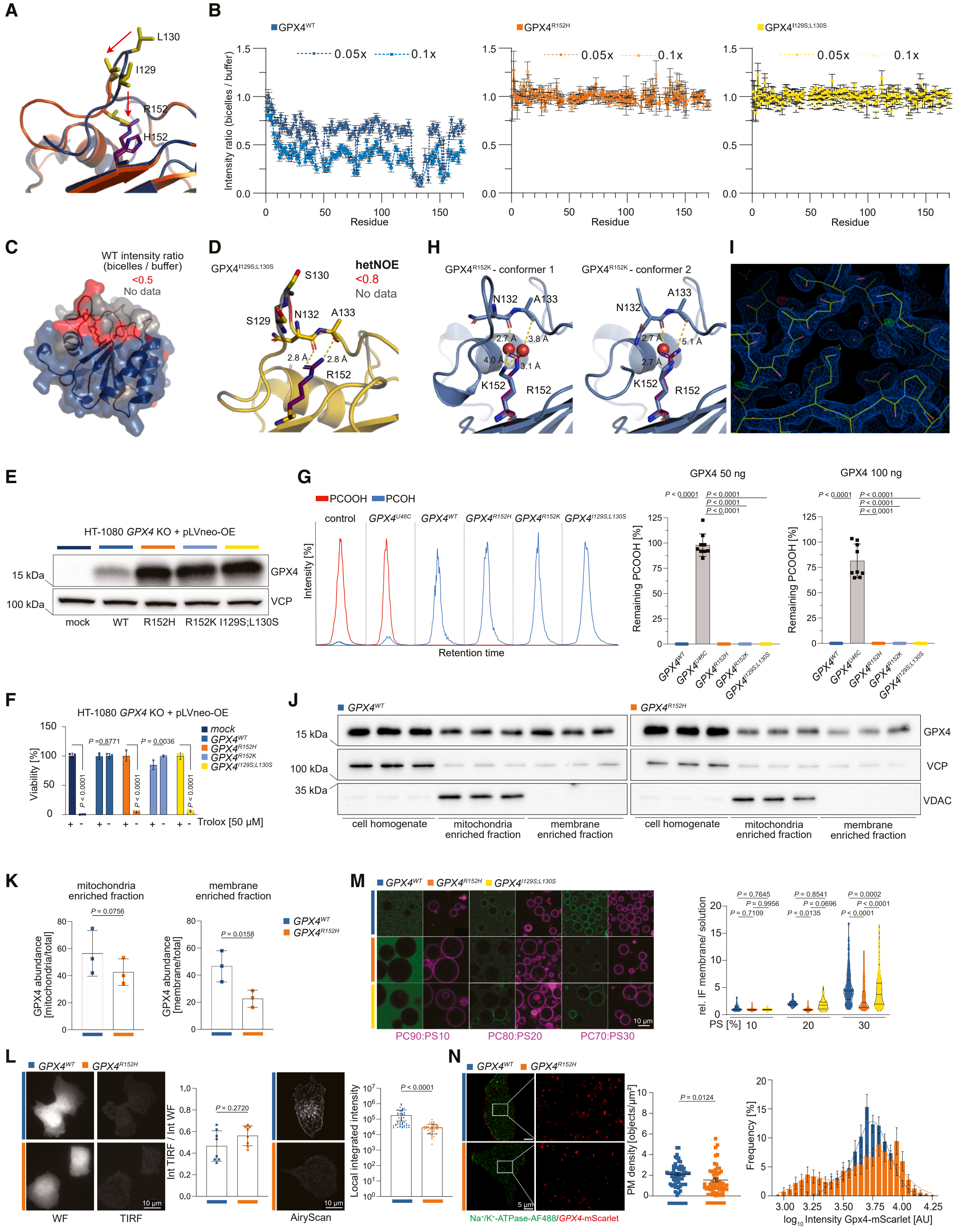

(legend on next page)

Therefore, we mutated the hydrophobic isoleucine and leucine residues (I129 and L130) to serines, producing the GPX4$^{I129S;L130S}$ mutant. ^{1}H,^{15}N HSQC spectra for this mutant overlaid well with the GPX4^{WT} spectrum, confirming that the overall fold of the GPX4$^{I129S;L130S}$ mutant is unaffected by the mutation (Figures S4A and S4C). hetNOE values for GPX4$^{I129S;L130S}$ showed that the protein backbone is well structured (values > 0.8). At the same time, a drop below 0.8 for the fin-loop region (residue 130) confirmed the flexibility of this region (Figure S5C), which is comparable to the WT protein. CSP analysis showed that CSPs are localized in the fin-loop region (Figure S4C). As a further validation, we determined the GPX4$^{I129S;L130S}$ mutant's crystal structure. The X-ray structure overlaid almost exactly with the GPX4^{WT} structure (RSMD 0.18 Å), including the fin-loop region (Figure 3D). This confirms that the introduced mutations do not disrupt the structure of the protruding fin-loop despite changing its lipophilicity and that R152 in this variant supports the loop through the side-chain-backbone hydrogen bonds as in the WT protein. Nevertheless, upon titration of bicelles, the CSP and intensity plots were comparable to the data for GPX4^{R152H} and not GPX4^{WT} (Figures 3B right and S6C). The intensity ratio was approximately 1.0 for all residues in GPX4$^{I129S;L130S}$, indicating no change in the overall tumbling of the protein and no interaction with bicelles. These data support our hypothesis that the protruding, hydrophobic fin-loop mediates the interaction of GPX4^{WT} with membranes, which can be disrupted by changing the polarity of the fin-loop or by disrupting the overall loop structure, as in

Figure 3. A hydrophobic fin-loop mediates membrane binding of GPX4

(A) Overlay of the GPX4^{WT} crystal structure (PDB: 2OBI) and GPX4^{R152H} showing the structural changes in the loop region of GPX4^{R152H}. The Ile129 side chain fills the space occupied by Arg152 in the wild-type (WT) protein. Residues Ile129 and Leu130 are colored yellow.

(B) Intensity ratios (bicelle intensity/buffer intensity) for backbone amide NMR signals of GPX4^{WT} (left), GPX4^{R152H} (middle), and GPX4$^{I129S;L130S}$ (right) in the presence of varying molar ratios of c7:c14-PC bicelles. Intensity ratios < 1 indicate line broadening of the amide signals in the presence of bicelles.

(C) Residues showing an intensity ratio (bicelle intensity/buffer intensity) < 0.5 for GPX4^{WT} in the presence of 0.05× bicelles in (B) (left), indicative of the binding surface with the membrane mimic, located to the fin-loop region and are colored red on the surface of GPX4^{WT} (PDB: 2OBI).

(D) {^{1}H}-^{15}N Heteronuclear NOE results are plotted on the crystal structure of GPX4$^{I129S;L130S}$. Ile129 and Leu130 are colored yellow. Residues with a heteronuclear NOE value < 0.8 (Figure S5C) are shown in red, indicating that the polypeptide backbone of the fin-loop in GPX4$^{I129S;L130S}$ shows fast ps-ns timescale motions. The fin-loop in the GPX4$^{I129S;L130S}$ mutant is stabilized by Arg152 via side-chain-to-backbone H-bonds to Asn132 and Ala133 but contains polar serine residues. Arg152 is highlighted in purple.

(E) Representative immunoblot analysis comparing the protein expression of GPX4 and loading control VCP in human HT-1080 *GPX4^{KO}* cells transfected with a pLVneo expression vector carrying a scrambled vector (mock), *GPX4^{WT}*, mutant *GPX4^{R152H}*, mutant *GPX4^{R152K}*, or mutant *GPX4$^{I129S;L130S}$*.

(F) Viability was measured with or without Trolox (50 μM) in HT-1080 *GPX4^{KO}* cells carrying either a scrambled vector (mock), *GPX4^{WT}*, mutant *GPX4^{R152H}*, mutant *GPX4^{R152K}*, or mutant *GPX4$^{I129S;L130S}$*. Results are representative of at least three independent experiments, and a two-way ANOVA followed by a Tukey's post hoc test was performed.

(G) Left: LC-MS intensity peaks of remaining PCOOH and PCOH in the activity reaction mix without enzymes (control) and in the presence of GPX4^{U46C}, GPX4^{WT}, GPX4^{R152H}, GPX4^{R152K}, and GPX4$^{I129S;L130S}$ enzymes. Right: normalized quantification of remaining PCOOH and PCOH in the activity reaction mix without enzymes (control) and in the presence of GPX4^{U46C}, GPX4^{WT}, GPX4^{R152H}, GPX4^{R152K}, and GPX4$^{I129S;L130S}$ enzymes. All GPX4^{R152H}, GPX4^{R152K}, and GPX4$^{I129S;L130S}$ mutants show the same PCOOH-reducing activity as the GPX4^{WT} control. Results are representative of three independent experiments, and statistical analysis was performed using a one-way ANOVA and post hoc analysis using Tukey's test.

(H) Crystal structure of GPX4^{R152K} showing the two loop conformers observed in the asymmetric unit. Left: conformer 1 shows that Lys152 interacts with Asn132 and Ala133 via two structural water molecules, which mimic the Arg152 side chain in GPX4^{WT}, stabilizing the fin-loop. Right: conformer 2 shows that the fin-loop is unresolved and only one structural water molecule is observed, which does not fully mimic the Arg152 side chain, suggesting that this causes loop destabilization.

(I) Electron density map for GPX4^{R152K}, conformer 1. In the R152K mutant, the hydrogen bond network stabilizing the fin-loop base is partially rescued by two water molecules. Interestingly, these water molecules assume positions nearly identical to those of the guanidine group in the WT. The fin-loop collapse is prevented, although its stability is reduced compared with WT.

(J) Immunoblot analysis of mitochondria- and membrane-enriched fractions isolated from HT-1080 *GPX4^{KO}*cells expressing GPX4^{WT} and GPX4^{R152H} shows a reduction in GPX4^{R152H} levels in the membrane-enriched fraction. An aliquot of each sample was loaded three times, representing technical replicates of one representative experiment. VDAC, a mitochondrial protein, is accumulated in mitochondria-enriched fractions, while VCP, a predominantly cytosolic protein, is present in both 10,000 × *g* and 100,000 × *g* pellet fractions to a lesser extent than in the cell homogenates.

(K) HT-1080 *GPX4^{KO}* cells expressing GPX4^{WT} and GPX4^{R152H} show a reduction in GPX4^{R152H} levels in the plasma-membrane-enriched fraction. Statistical analysis was performed using a Student's *t* test.

(L) Stable cell lines expressing mScarlet-fused GPX4^{WT} or GPX4^{R152H} were imaged to assess membrane localization. Left: total internal reflection fluorescence (TIRF) microscopy and widefield imaging were used to compare the distribution of GPX4 variants. Quantification of mScarlet fluorescence revealed no significant redistribution of GPX4^{R152H} from the plasma membrane (PM) to internal membranes, consistent with subcellular fractionation data. Statistical analysis was performed using a Kolmogorov-Smirnov test. Right: AiryScan super-resolution microscopy of the basal PM showed that GPX4^{WT} localized to discrete nanodomains, while GPX4^{R152H} exhibited a diffuse and uniform pattern. These findings indicate that the R152H mutation impairs membrane clustering without fully abolishing membrane association, suggesting altered spatial organization as a mechanism for reduced anti-ferroptotic activity. Statistical analysis was performed using a Mann-Whitney test.

(M) Confocal microscopy images of giant unilamellar vesicles (GUVs) made of phosphatidylcholine (PC) and phosphatidylserine (PS) at different proportions containing 0.1% of 1,1′-dioctadecyl-3,3,3′,3′-tetramethylindocarbocyanine perchlorate (DiI) (magenta) after 1 h of incubation with the fluorescently labeled version of GPX4^{WT}, GPX4^{R152H}, or GPX4$^{I129S;L130S}$ with Atto 488 (5 μM) (green). Each dot represents one GUV. Between 55 and 440 vesicles from 3 independent experiments were analyzed in each condition. Statistical analysis was performed with two-way ANOVA with Tukey's post hoc test.

(N) Left: representative SIM images and quantifications of PM sheets of GPX4-mScarletWT and GPX4^{R152H}-mScarlet Pfa1 cells. Staining of Na$^+$/K$^+$-ATPase (in green) was used to create a mask of the PM for GPX4 quantifications. Scale bar, 5 μm. Center: PM density of Gpx4-mScarlet. Statistical analysis was performed using an unpaired Student's *t* test. Right: histograms showing intensity of GPX4-mScarlet signal in the PM. Values plotted are the mean ± SEM from three biological replicates (*n* = 57 and *n* = 55 cells imaged for GPX4-mScarletWT and GPX4^{R152H}-mScarlet, respectively).

See also Figures S4–S6.

Please cite this article in press as: Lorenz et al., A fin-loop-like structure in GPX4 underlies neuroprotection from ferroptosis, Cell (2026), https://doi.org/10.1016/j.cell.2025.11.014

GPX4^{R152H}. To investigate its behavior *in vitro*, we stably expressed the artificial GPX4$^{I129S;L130S}$ variant in HT-1080 *GPX4^{KO}* cells (Figure 3E). In line with our hypothesis, the replacement of WT GPX4 with the double mutant phenocopied the effect observed for GPX4^{R152H} with rapid induction of ferroptosis, which could be prevented by treatment with Trolox, supporting the notion that GPX4$^{I129S;L130S}$ cannot prevent ferroptosis *in vitro* (Figure 3F).

To perform a sufficiency experiment and test whether GPX4's anti-ferroptotic function could be restored through conservative substitution at position 152, we generated a variant in which the WT arginine (R152) was replaced by lysine (R152K). Expression of GPX4^{R152K} in ferroptosis-sensitized cells fully rescued cell viability and preserved enzyme activity comparable to GPX4^{WT}, suggesting that lysine can functionally substitute for arginine in this context (Figures 3E–3G and S6D). To investigate the structural basis of this rescue, we solved the crystal structure of GPX4^{R152K} at 2.0 Å resolution (Figures 3H and 3I). The asymmetric unit contained two protein molecules, revealing distinct conformational states of the fin-loop (Figures 3H and S6E). In one molecule, the fin-loop adopted an extended configuration reminiscent of the WT enzyme, but with weaker and slightly distorted electron density, indicative of increased flexibility. Notably, two ordered water molecules bridged the lysine side chain (K152) with N132 and A133, partially mimicking the hydrogen-bonding pattern established by the guanidinium group of R152 in the WT protein. Conversely, the second molecule showed a fully disordered fin-loop with no interpretable electron density, stabilized only by a single water molecule in the void left by the missing guanidinium group (Figures 3H and 3I). These findings indicate that the R152K substitution partially restores fin-loop stabilization via water-mediated interactions but lacks the structural rigidity conferred by the native arginine. Nevertheless, this limited stabilization is sufficient to preserve GPX4 membrane engagement and ferroptosis suppression, emphasizing the critical role of loop integrity.

So far, our data indicate that GPX4's binding ability to membranes is mediated by two collaborating structural components: the presence of hydrophobic amino acids located at the outer side of GPX4 and the arginine residue stabilizing the fin-loop by the network of polar interactions within the core of the protein. To further evaluate the impact of the R152H mutation on GPX4 membrane association, we next employed orthogonal biochemical and imaging approaches. First, we performed subcellular fractionation in HT-1080 *GPX4^{KO}* cells stably expressing either GPX4^{WT} or GPX4^{R152H}. Following cell homogenization and multistep differential centrifugation, we isolated mitochondrial- and membrane-enriched fractions (Figure S6F). Quantification of immunoblot analysis revealed a consistent reduction in GPX4^{R152H} levels in the plasma-membrane-enriched fraction compared with GPX4^{WT}, normalized to total input (Figures 3J and 3K). GPX4 levels in the mitochondria-enriched fraction remained unchanged, although a mild downward trend was observed in cells expressing the R152H variant.

Next, we utilized stable cell lines expressing GPX4-mScarlet fusion proteins to assess membrane association in intact cells (Figure 3L). Total internal reflection fluorescence (TIRF) microscopy, which selectively visualizes the plasma membrane, was employed alongside widefield imaging. A comparison of mScarlet signal intensity in TIRF versus widefield mode revealed no significant redistribution of GPX4^{R152H} to internal membranes, consistent with the subcellular fractionation data (Figure 3L left). To interrogate changes in membrane organization at higher resolution, we performed AiryScan super-resolution microscopy focusing on the basal plasma membrane (Figure 3L right). Whereas GPX4^{WT} formed discrete, clustered nanodomains, the R152H variant displayed a diffuse and homogenous distribution. These results suggest that although the R152H mutation does not completely abrogate membrane association, it disrupts the lateral organization and possibly the membrane residency dynamics of GPX4. Together, these data demonstrate that GPX4^{R152H} exhibits impaired, but not absent, membrane association. The loss of nanoscopic clustering provides a mechanistic basis for the reduced anti-ferroptotic function of this variant, underscoring the importance of proper membrane anchoring and spatial organization for GPX4 function.

To confirm these data in a more physiological setting, we determined the membrane binding of GPX4^{R152H} or the control mutant GPX4$^{I129S;L130S}$ to giant unilamellar vesicles (GUVs) as a function of membrane lipid composition (Figure 3M). We incubated WT and mutant enzymes with GUVs containing an increasing concentration of brain phosphatidylserines (PS), which, unlike egg phosphatidylcholines (PCs), have a net negative charge. We used fluorescently labeled versions of the three proteins with Atto 488 to directly visualize the binding of the enzymes to the GUVs by confocal microscopy. Quantitative analysis showed that the enhanced membrane binding of GPX4^{WT} by electrostatic interactions could not be rescued in the GPX4^{R152H} mutant, and only to a lesser extent in the GPX4$^{I129S;L130S}$ mutant, indicating that the hydrophobic interactions of the fin-loop with the lipid bilayer are dominant for binding to cell-like membranes (Figure 3M).

Finally, to address the capability of GPX4^{R152H} to bind to the cell membrane, we performed structured illumination microscopy (SIM) of Pfa1 cells expressing either the R152H mutant or the WT enzyme (Figure 3N). In line with our previous findings, binding was decreased in cells expressing the mutant, suggesting that either complete loss due to genetic deletion or truncating mutations, or the inability of GPX4 to bind to the inner layers of the cell membrane, could trigger ferroptosis *in vitro* and *in vivo*. Altogether, these data demonstrate that the ultra-rare R152H mutant impedes the correct targeting of GPX4^{R152H} to cell membranes, profoundly hampering its anti-ferroptotic role.

GPX4 critically affords cortical and cerebellar neuron integrity

Having defined the structural basis by which GPX4 interacts with membranes to prevent phospholipid peroxidation and ferroptosis, we next assessed its functional relevance in the CNS, a tissue particularly vulnerable to GPX4 deficiency and a prominent site of pathology in SSMD and GPX4^{R152H}-associated disease. Previous studies have demonstrated an essential role for GPX4 in neuronal survival,[13,21] yet existing models do not allow for the temporal resolution of neuronal loss. To overcome this, we employed a TAM-inducible, glutamatergic neuron-specific Cre driver line (*Camk2aCreER$^{T2+/tg}$*). This line was crossed with

Please cite this article in press as: Lorenz et al., A fin-loop-like structure in GPX4 underlies neuroprotection from ferroptosis, Cell (2026), https://doi.org/10.1016/j.cell.2025.11.014

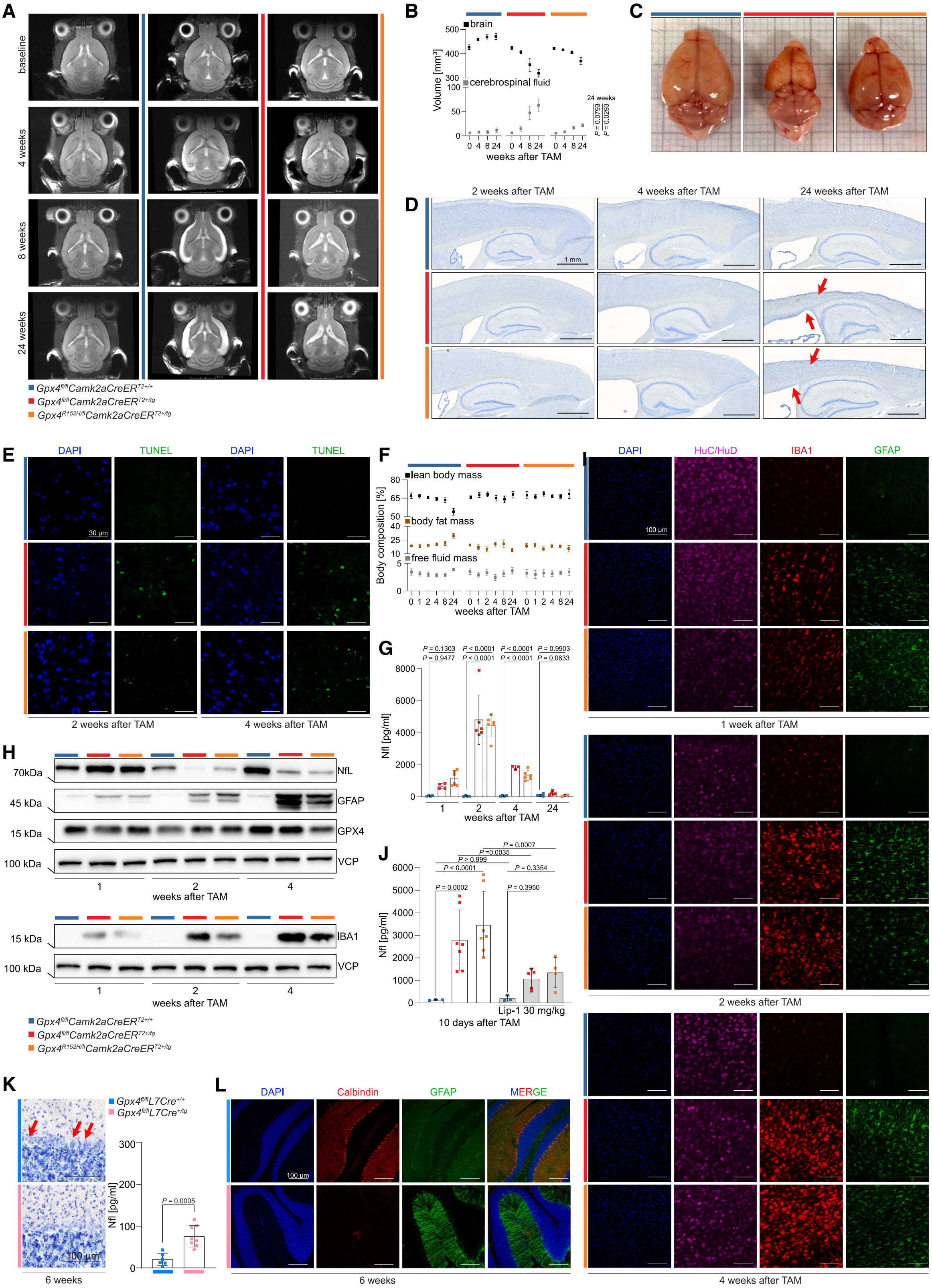

(legend on next page)

Please cite this article in press as: Lorenz et al., A fin-loop-like structure in GPX4 underlies neuroprotection from ferroptosis, Cell (2026), https://doi.org/10.1016/j.cell.2025.11.014

either *Gpx4*$^{fl/fl}$ or *Gpx4*$^{R152H/fl}$ mice, generating both complete knockout (KO) and patient-mimicking alleles expressed selectively in forebrain glutamatergic neurons (Figure S7A).

TAM administration led to progressive cortical neurodegeneration in both *Gpx4*$^{fl/fl}$*Camk2aCreER*$^{T2+/tg}$ and *Gpx4*$^{R152H/fl}$*Camk2aCreER*$^{T2+/tg}$ mice (Figures 4A–4D), with the latter exhibiting a milder, hypomorphic phenotype, akin to the clinical presentation of classical SSMD patients versus carriers of the R152H variant. MRI and gross brain inspection revealed widespread cortical atrophy (Figures 4A–4C), mirrored by Nissl staining (Figure 4D), which showed thinning and disorganization of cortical layers. TUNEL staining confirmed widespread cell death within cortical structures (Figure 4E). Compared with WT, *Gpx4*$^{fl/fl}$*Camk2aCreER*$^{T2+/tg}$ and *Gpx4*$^{R152H/fl}$*Camk2aCreER*$^{T2+/tg}$ mice showed no body weight gain despite preserved body composition (Figure 4F), indicating a central, rather than a peripheral, origin of the wasting phenotype. As mobility and rearing capacity declined, affected mice required food placed on cage bedding to ensure feeding. Impairment in motor skills, determined by rotarod and other motoric tests, precluded short-term memory determination in the Y-maze and was evident within 2 weeks post TAM (Figure S7B). Notably, no sex differences were observed across all phenotypic measures.

To extend our analysis beyond CNs, we generated a cerebellum-specific KO using the L7Cre driver (Figures S7C and S7D), mainly targeting Purkinje cells from postnatal day 6 until full recombinase activity around days 21–24. *Gpx4*$^{fl/fl}$ *L7Cre*$^{+/tg}$ mice were born normally and were indistinguishable from their WT littermates. From 6 weeks of age, *Gpx4*-deficient mice exhibited an abnormal gait and developed a pronounced ataxic phenotype (Video S2). Histological analysis revealed near-complete loss of calbindin^{+} Purkinje neurons, accompanied by pronounced astrogliosis, providing a mechanistic correlate for the observed motor dysfunction (Figures 4K and 4L). These findings are consistent with prior results from *Gpx4*$^{fl/fl}$ *Tα1-Cre* mice, which exhibited cerebellar hypoplasia and Purkinje cell loss but succumbed too early to assess post-developmental effects.[37] In contrast, the *L7Cre* model permits evaluation of cerebellar ferroptosis in the mature brain.

Neurofilament light chain (NfL) is an axonal structural protein and an established marker of neuronal damage in the plasma and cerebrospinal fluid (CSF), and it is being tested for clinical implementation in patients with neurological symptoms who suffer from neurodegenerative disease.[38–40] Thus, we measured NfL levels in plasma to determine whether neuronal loss could be monitored systemically. NfL was robustly elevated in *Gpx4*$^{fl/fl}$ *Camk2aCreER*$^{T2+/tg}$ and *Gpx4*$^{R152H/fl}$*Camk2aCreER*$^{T2+/tg}$ mice as early as 1 week post TAM, peaking at 60-fold above control levels by week 2, mirroring biomarkers used in human neurodegenerative disease (Figure 4G). We performed transmission

Figure 4. GPX4 is essential for cortical and cerebellar neuron integrity

(A) Representative brain MRI data over an observation period of 24 weeks after TAM injection showing atrophy in the cortical region associated with an increase in cerebrospinal fluid (CSF) within the subarachnoid space, conspicuous as early as 4 weeks after TAM in *Gpx4*$^{fl/fl}$*Camk2aCreER*$^{T2+/tg}$ mice compared with baseline measurement and *Gpx4*$^{fl/fl}$*Camk2aCreER*$^{T2+/+}$ control mice. In *Gpx4*$^{R152H/fl}$*Camk2aCreER*$^{T2+/tg}$ mice, a slight increase in the volume of the lateral ventricles can be seen starting from week 4 after TAM. The ventricles continue to enlarge, with the largest dimensions visible at 24 weeks, whereas the brain atrophy is less severe compared with *Gpx4*$^{fl/fl}$*Camk2aCreER*$^{T2+/tg}$ mice (n = 3 males per genotype).

(B) Volumetry by manual segmentation of the MRI data into brain and CSF discloses progressive atrophy in *Gpx4*$^{fl/fl}$*Camk2aCreER*$^{T2+/tg}$ and *Gpx4*$^{R152H/fl}$*Camk2aCreER*$^{T2+/tg}$ mice. Statistical analysis was performed with two-way ANOVA with Tukey's post hoc test.

(C) Macroscopic image of whole brains from *Gpx4*$^{fl/fl}$*Camk2aCreER*$^{T2+/+}$, *Gpx4*$^{fl/fl}$*Camk2aCreER*$^{T2+/tg}$, and *Gpx4*$^{R152H/fl}$*Camk2aCreER*$^{T2+/tg}$ mice dissected 24 weeks post TAM.

(D) Nissl staining of sagittal brain sections of *Gpx4*$^{fl/fl}$*Camk2aCreER*$^{T2+/+}$, *Gpx4*$^{fl/fl}$*Camk2aCreER*$^{T2+/tg}$, and *Gpx4*$^{R152H/fl}$*Camk2aCreER*$^{T2+/tg}$ mice after TAM injection revealed distinct signs of morphological alterations in cortical structures, such as loss of cortical layers, massive cortical atrophy as indicated by red arrows, and an increase in the volume of the ventricles. The scale bar indicates 1 mm.

(E) Representative TUNEL staining of cortical structures of *Gpx4*$^{fl/fl}$*Camk2aCreER*$^{T2+/+}$, *Gpx4*$^{fl/fl}$*Camk2aCreER*$^{T2+/tg}$, and *Gpx4*$^{R152H/fl}$*Camk2aCreER*$^{T2+/tg}$ mice with DAPI counterstain at 2 and 4 weeks after TAM injection. Scale bar indicates 10 μm.

(F) Body composition analysis measured lean and fat mass and free fluid and revealed conserved body composition in *Gpx4*$^{fl/fl}$*Camk2aCreER*^{T2} and *Gpx4*$^{R152H/fl}$*Camk2aCreER*^{T2} mice. Values plotted are the mean ± SD from biological replicates ($n \geq 5$ per genotype). Statistical analysis was performed using a one-way ANOVA with Tukey's post hoc test.

(G) Neurofilament light chain (NfL) levels were determined in plasma samples derived from *Gpx4*$^{fl/fl}$*Camk2aCreER*$^{T2+/+}$, *Gpx4*$^{fl/fl}$*Camk2aCreER*$^{T2+/tg}$, and *Gpx4*$^{R152H/fl}$*Camk2aCreER*$^{T2+/tg}$ mice (n numbers are indicated in the figure, and each dot represents an individual mouse) using a Simoa or Ella automated immunoassay system. Measurement was performed at the indicated time points after TAM induction. Statistical analysis was performed using a one-way ANOVA with Tukey's post hoc test.

(H) Representative immunoblot analysis from bulk cortical tissue of *Gpx4*$^{fl/fl}$*Camk2aCreER*$^{T2+/+}$, *Gpx4*$^{fl/fl}$*Camk2aCreER*$^{T2+/tg}$, and *Gpx4*$^{R152H/fl}$*Camk2aCreER*$^{T2+/tg}$ mice comparing expression of NfL, GFAP, GPX4, and IBA1 at 1, 2, and 4 weeks after TAM injection. VCP expression was used as a loading control.

(I) Immunohistochemical analysis showing neuronal loss (stained by HuC/HuD), widespread astrogliosis (stained by GFAP), and microgliosis (stained by IBA1) in cortical tissues of *Gpx4*$^{fl/fl}$*Camk2aCreER*$^{T2+/tg}$ and *Gpx4*$^{R152H/fl}$*Camk2aCreER*$^{T2+/tg}$ mice compared with *Gpx4*$^{fl/fl}$*Camk2aCreER*$^{T2+/+}$. Scale bar indicates 100 μm.

(J) NfL levels were determined in plasma samples derived from Lip-1-treated (30 mg/kg Lip-1 for 10 days) and vehicle-treated *Gpx4*$^{fl/fl}$*Camk2aCreER*$^{T2+/+}$, *Gpx4*$^{fl/fl}$*Camk2aCreER*$^{T2+/tg}$, and *Gpx4*$^{R152H/fl}$*Camk2aCreER*$^{T2+/tg}$ mice, showing significantly reduced neuronal cell death upon Lip-1 treatment. Statistical analysis was performed using two-way ANOVA with Tukey's post hoc test (n numbers are indicated in the figure, with each dot representing an individual mouse).

(K) Nissl staining of sagittal brain sections of *Gpx4*$^{fl/fl}$*L7Cre*$^{+/+}$ and *Gpx4*$^{fl/fl}$*L7Cre*$^{+/tg}$ mice, revealing loss of the Purkinje cell layer in the cerebellum of *Gpx4*$^{fl/fl}$ *L7Cre*$^{+/tg}$ mice at 6 weeks, as indicated by red arrows. Scale bar indicates 100 μm. NfL levels in plasma samples derived from 6-week-old *Gpx4*$^{fl/fl}$*L7Cre*$^{+/tg}$ mice are significantly elevated compared with WT controls. Statistical analysis was performed using unpaired Student's *t* test (n numbers are indicated in the figure, with each dot representing an individual mouse).

(L) Immunohistochemical analysis showing complete loss of Calbindin^{+} Purkinje cells and astrogliosis (stained by GFAP) in cerebellar tissues of 6-week-old *Gpx4*$^{fl/fl}$*L7Cre*$^{+/tg}$ mice compared with *Gpx4*$^{fl/fl}$*L7Cre*$^{+/+}$ mice. Scale bar indicates 50 μm.

See also Figure S7.

Please cite this article in press as: Lorenz et al., A fin-loop-like structure in GPX4 underlies neuroprotection from ferroptosis, Cell (2026), https://doi.org/10.1016/j.cell.2025.11.014

electron microscopy of the sciatic nerve to exclude peripheral nervous system degeneration, which showed no structural abnormalities (Figure S7E). Because ultrasensitive immunoassays are optimized for human use, we performed an unbiased plasma proteomics survey across 1, 2, and 4 weeks post TAM for *Gpx4*$^{fl/fl}$*Camk2aCreER*$^{T2+/tg}$ mice. In addition to the confirmation of upregulated NfL, 77 proteins were differentially expressed (Figures S7F and S7G; Table S1, sheet 3), including neural cell adhesion molecule 1 (NCAM1) and immune-related factors such as hemopexin (Hpx) and C-reactive protein (CRP), consistent with a neurodegenerative and neuroinflammatory signature. Together, these data establish a critical, non-redundant role for GPX4 in cortical and cerebellar neuron survival, linking ferroptotic stress to functional impairment in the CNS, and provide a tractable *in vivo* system for studying the molecular basis of GPX4-related neurodegeneration.

Because neuronal cells dying by ferroptosis may exert a cell-nonautonomous impact on neighboring cells, a series of experiments were conducted to address the fate of non-neuronal brain cells, such as astrocytes and immune cells, in WT and *Gpx4*$^{fl/fl}$ *Camk2aCreER*$^{T2+/tg}$ mice. Immunofluorescent imaging and immunoblot analysis showed that neuronal cell death was, in fact, accompanied by progressive massive astrogliosis (as determined by glial fibrillary acidic protein [GFAP] staining), followed by marked microgliosis (as determined by allograft inflammatory factor 1 [IBA1] staining) (Figures 4H and 4I). Interestingly, a time-resolved analysis revealed that, although GFAP expression had already increased 1 week after neuronal GPX4 deletion and remained constantly high thereafter (Figures 4H, upper, and 4I), robust immunostaining against IBA1 was detectable only at 2 weeks and culminated at 4 weeks after KO induction (Figures 4H, middle and lower, and 4I). These findings suggest that the initial wave of cell death triggered a monophasic immunologic reaction, possibly contributing to the overall destruction of cortical mass, resembling neurodegeneration in human disease.

To obtain a more detailed assessment of the immune cell populations infiltrating the *Gpx4* KO brain, we performed a granular FACS-based analysis of the total brain hemispheres (Figure S7H). An initial analysis revealed no qualitative changes between WT and KO animals. Likewise, the distribution of common lineages discriminating between the major immune cell classes did not demonstrate any significant change (Figure S7I). However, the absolute number of CD45^{+} infiltrating cells was significantly higher in the KO cortex compared with WT controls 4 weeks after TAM induction (Figure S7J). These changes favor a neuroinflammatory component, potentially exacerbating the detrimental effects of neuronal *Gpx4* deletion. Notably, tissue-resident immune cells, i.e., microglia, are reported to evolve strongly during neurodegeneration.[41] The expression and morphology of microglia alter strongly during activation in disease states (Figure S7K). Importantly, their activation state has been reported to be governed by strong fluctuations correlating with disease severity. Because our immunophenotyping approach did not uncover qualitative changes beyond the elevated influx of immune cells of hematopoietic origin, we performed a differential staining protocol reflecting the varying activation states of microglia in the brain (Figures S7L and S7M). This analysis revealed that, strikingly, loss of GPX4 exerted a potent activation effect on microglia. Specifically, although homeostatic WT microglia expressing purinergic receptor P2Y12 (P2RY12), C-X3-C motif chemokine receptor 1 (CX3CR1), and lymphocyte antigen 6 family member C1 (Ly6C) were the predominant subtypes in WT mice, genetic deletion of *Gpx4* triggered their polarization into so-called disease-associated microglia (DAM) expressing triggering receptor expressed on myeloid cells 2 (TREM2), beta-2-microglobulin (B2M), CD80, and major histocompatibility complex class II (MHC class II), while downregulating homeostatic markers[41,42] (Figure S7N). These findings suggest that our model reflects changes in immune landscapes very similar to other models of neurodegeneration,[43] which are, however, independent of *Gpx4* deficiency.

Notably, NfL increased significantly as early as 1 week after TAM treatment (Figure 4G). This elevation preceded detectable gliosis, as confirmed by immunoblot and immunohistochemistry analysis of activation markers (Figures 4H and 4I). Microglial and astrocytic activation emerged only thereafter, suggesting that gliosis is secondary to ferroptosis-driven neuronal injury rather than an initiating event. These findings support the concept that targeting ferroptosis upstream of neuroinflammation may yield beneficial therapeutic outcomes compared with interventions directed solely at downstream glial responses. To test this hypothesis directly, we treated *Gpx4*-deficient mice with Lip-1, a gold-standard ferroptosis inhibitor.[14] 10 days of treatment with 30 mg/kg Lip-1 significantly reduced neuronal cell death and restored serum NfL levels to near baseline (Figure 4J). This pharmacological rescue confirms ferroptosis as the primary driver of neurodegeneration in our models and demonstrates that ferroptosis inhibition can preserve neuronal integrity *in vivo*. Together, these results functionally link ferroptotic stress to neuronal loss and establish a tractable therapeutic strategy to mitigate neurodegeneration in *GPX4*-deficient states.

Neuroproteomic profiling links GPX4 deficiency to dementia-like molecular signatures

Given the robust neuroinflammatory response observed in our neuron-specific *Gpx4* KO model, we sought to explore the broader molecular landscape and its relevance to human neurodegenerative disease. To this end, we conducted a series of unbiased, label-free MS-based proteomic analyses of cortical tissue collected at 1, 2, and 4 weeks following TAM-induced *Gpx4* deletion (Figure S8A). Principal-component analysis and hierarchical clustering revealed a clear temporal separation, with the most pronounced molecular divergence occurring at 4 weeks, coinciding with the peak of neurodegeneration and glial activation (Figures 5A and S8B; Table S1, sheet 3). Differential expression analysis identified a growing set of deregulated proteins over time (Table S1, sheet 5–7), and pathway enrichment analysis (adjusted $p < 0.05$) revealed that the Kyoto Encyclopedia of Genes and Genomes (KEGG) "Alzheimer's disease" (AD) pathway, together with other neurodegenerative disorders, emerged as one of the most prominently enriched signatures at the 4-week time point (Figure 5B; Table S1, sheets 8–10). Among the top upregulated proteins were apolipoprotein E (APOE) and clusterin (CLU, also known as apolipoprotein J [APOJ]), which

Please cite this article in press as: Lorenz et al., A fin-loop-like structure in GPX4 underlies neuroprotection from ferroptosis, Cell (2026), https://doi.org/10.1016/j.cell.2025.11.014

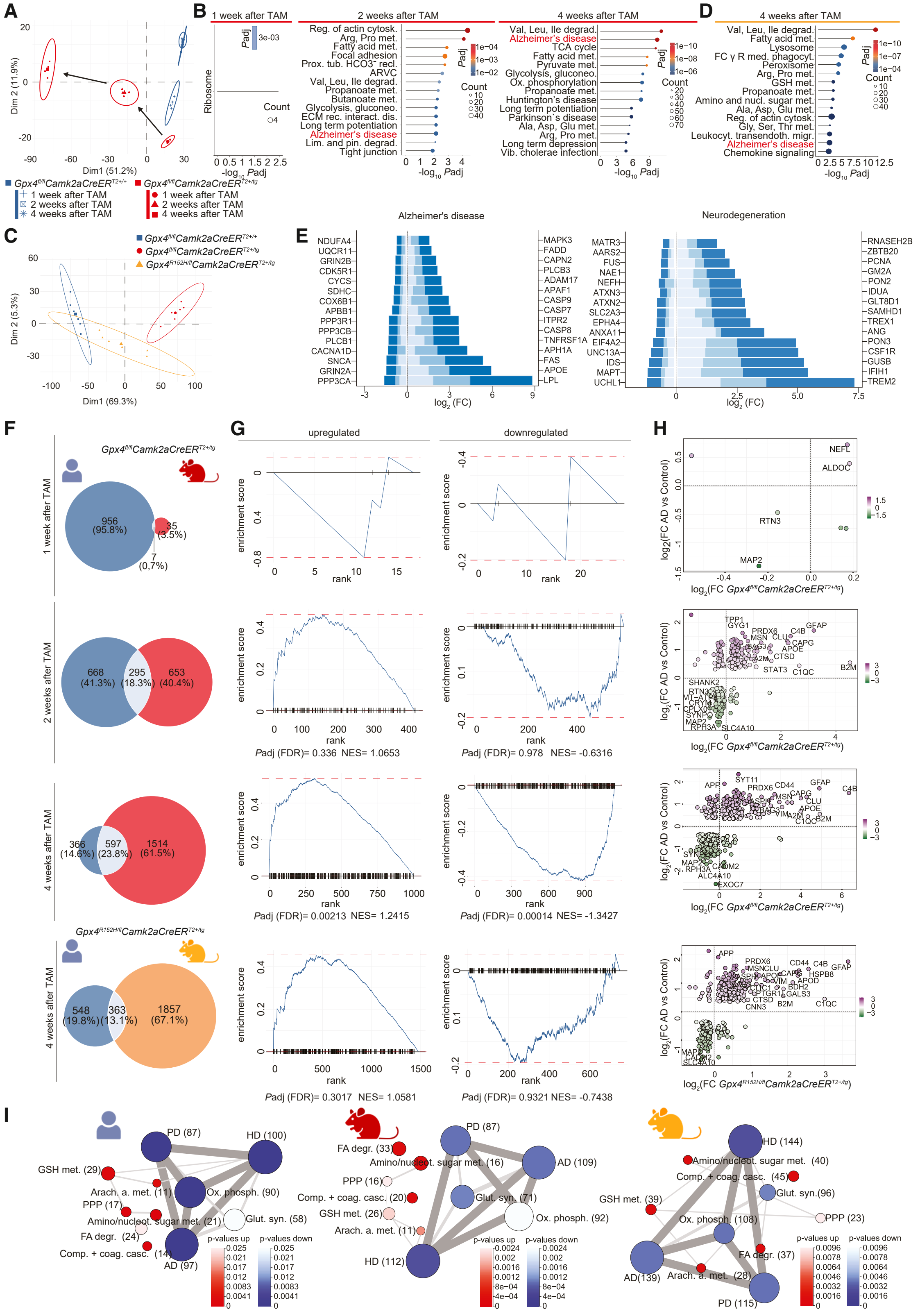

(legend on next page)

are canonical AD-associated markers implicated in lipid metabolism and neuroinflammation (Figure 5H). To contextualize these findings, we applied weighted gene co-expression network analysis (WGCNA), which identified a central module driven by neuron-specific changes, distinct from glial-derived signatures (Figures S9A–S9I). These modules were strongly associated with pathways underlying the progression of neurodegenerative diseases. To further validate the translational relevance of our models, we extended these analyses to *Gpx4*$^{R152H/fl}$*Camk2aCreER*$^{T2+/tg}$ mice (Figures 5C and 5D). At 4 weeks post induction, proteomic profiling of the cortical tissue of these patient-mimicking knockin mice revealed molecular changes that mimicked the full *Gpx4* KO, including the same AD-enriched modules and key signature proteins, albeit in a hypomorphic manner (Figure 5E).

These data reinforce the hypomorphic nature of the *R152H* variant and establish a mechanistic continuum between the genetic models and the human clinical phenotype. To benchmark our findings against those of human disease, we leveraged a meta-analysis comprising eight independent proteomic datasets from AD patients, spanning multiple brain regions and cohort sizes. Gene set enrichment and pathway network analyses revealed a substantial overlap between the murine and human datasets, with shared upregulation of proteins related to neurodegeneration and inflammation (Figures 5F–5H and S10). Using the Piano framework further confirmed nearly identical biological network engagement between *Gpx4*-deficient mice and AD brains. Together, these results position GPX4 deficiency as a monogenic model of neurodegeneration that converges molecularly with complex, late-onset human disease. The ability of *Gpx4*^{R152H} knockin mice to recapitulate these AD-like signatures further bridges the gap between inherited ferroptotic vulnerability and common neurodegenerative phenotypes (Figure 5I; Table S1, sheets 11 and 12).

DISCUSSION

Here, we dissect the structural and functional impact of a homozygous *GPX4* missense variant (p.R152H) found in three patients suffering from the ultra-rare autosomal recessive disorder SSMD. Intriguingly, despite its preserved protein expression and catalytic activity, the GPX4^{R152H} variant invariably failed to suppress ferroptosis *in vitro* or *in vivo*. Using high-resolution NMR spectroscopy and X-ray crystallography, we identified a structural mechanism underlying this failure to suppress ferroptosis: the R152H substitution effectively destabilizes a fin-like hydrophobic loop, which proved critical for engaging with lipid membranes. We find that this collapse impairs GPX4's ability to interact with lipid bilayers, its quintessential site of action. Consistent with this study's proposed model, site-directed mutagenesis of neighboring hydrophobic residues (I129 and L130) recapitulated this effect, highlighting the importance of the fin-loop and local hydrophobicity in averting ferroptosis. Substituting R152 with a lysine (R152K) partially restored the fin-loop stabilization via water-mediated hydrogen bonds, which suggests that even modest structural compensation at this site is

Figure 5. Neuroproteomic profiling links GPX4 deficiency to dementia-like molecular signatures

(A) Principal-component analysis (PCA) of *Gpx4*$^{fl/fl}$*Camk2aCreER*$^{T2+/+}$ and *Gpx4*$^{fl/fl}$*Camk2aCreER*$^{T2+/tg}$ mouse cortex samples at 1, 2, and 4 weeks after TAM injection.

(B) Topmost-enriched KEGG pathways of significantly regulated proteins (p adj. < 0.05) for *Gpx4*$^{fl/fl}$*Camk2aCreER*$^{T2+/+}$ versus *Gpx4*$^{fl/fl}$*Camk2aCreER*$^{T2+/tg}$ mouse cortex 1, 2, and 4 weeks after TAM injection, represented by lollipop charts. The size of the dot "count" indicates the number of regulated proteins in the corresponding pathway. The category AD is significantly overrepresented 2 weeks after TAM injection.

(C) PCA of *Gpx4*$^{fl/fl}$*Camk2aCreER*$^{T2+/+}$*,* *Gpx4*$^{fl/fl}$*Camk2aCreER*$^{T2+/tg}$, and *Gpx4*$^{R152H/fl}$*Camk2aCreER*$^{T2+/tg}$ mouse cortex samples at 4 weeks after TAM injection.

(D) Topmost-enriched KEGG pathways of significantly regulated proteins (p adj. < 0.05) for *Gpx*$^{R152H/fl}$*Camk2aCreER*$^{T2+/tg}$ mouse cortex 4 weeks after TAM injection, represented by lollipop charts. The size of the dot count indicates the number of regulated proteins in the corresponding pathway. The category AD is significantly overrepresented 4 weeks after TAM injection.

(E) Bar plot showing $\log_2$ fold change ($\log_2$(FC)) in gene expression levels for the top 30 differentially expressed genes among *Gpx4*$^{fl/fl}$*Camk2aCreER*$^{T2+/tg}$ (KO), *Gpx4*$^{R152H/fl}$*Camk2aCreER*$^{T2+/tg}$ (mutant), and *Gpx4*$^{fl/fl}$*Camk2aCreER*$^{T2+/+}$ (WT) groups. Each gene displays three comparisons: KO versus WT (dark blue), mutant versus WT (medium blue), and KO versus mutant (light blue). Positive values indicate upregulation, and negative values indicate downregulation relative to the stated comparator group.

(F) Venn diagrams showing the intersection of significantly expressed proteins derived from the published meta-analysis of AD studies (blue set) and from *Gpx4*$^{fl/fl}$ *Camk2aCreER*$^{T2+/+}$ versus *Gpx4*$^{fl/fl}$*Camk2aCreER*$^{T2+/tg}$ cortical samples (red set) 1, 2, and 4 weeks after TAM injection, as well as *Gpx4*$^{fl/fl}$*Camk2aCreER*$^{T2+/+}$ versus *Gpx4*$^{R152H/fl}$*Camk2aCreER*$^{T2+/tg}$ cortical samples (orange set) 4 weeks after TAM injection. Percentages refer to the sum of all proteins from both datasets. The overlap between the human dataset and mouse datasets increases from 0.7 % at week 1 to 18.3 % at week 2 and 23.8 % at week 4 after TAM injection. The overlap between the human dataset and dataset of the mutant mice amounts to 13.1 % at week 4 after TAM injection.

(G) Enrichment plot of the AD meta-analysis dataset from 456 upregulated proteins (left) and 507 downregulated proteins (right) evaluating separately significantly upregulated and downregulated proteins in *Gpx4*$^{fl/fl}$*Camk2aCreER*$^{T2+/+}$ versus *Gpx4*$^{fl/fl}$*Camk2aCreER*$^{T2+/tg}$ cortical samples at 1, 2, and 4 weeks after TAM injection, as well as *Gpx4*$^{fl/fl}$*Camk2aCreER*$^{T2+/+}$ versus *Gpx4*$^{R152H/fl}$*Camk2aCreER*$^{T2+/tg}$ cortical samples at 4 weeks after TAM injection. The red dashed line shows the maximum deviation from zero of the enrichment score. The fast gene set enrichment analysis (FGSEA) curves of upregulated and downregulated AD proteins revealed significant enrichment, respectively, for up- and downregulated mouse proteins 4 weeks after TAM injection (i.e., calculated p adjusted from the FGSEA program: p adj. = 0.0021 for upregulated and p adj. = 0.0001 for downregulated proteins).

(H) Scatterplot showing the $\log_2$ FC in AD versus control from the reanalyzed meta-analysis on the y axis and the $\log_2$ FC in *Gpx4*$^{fl/fl}$*Camk2aCreER*$^{T2+/+}$ and *Gpx4*$^{fl/fl}$*Camk2aCreER*$^{T2+/tg}$ mice in the cortex on the x axis for 1, 2, and 4 weeks after TAM treatment as well as the $\log_2$ FC in *Gpx4*$^{R152H/fl}$*Camk2aCreER*$^{T2+/tg}$ mice in the cortex on the x axis for 4 weeks after TAM treatment.

(I) Network of KEGG pathways generated by gene set analysis (GSA) of the Piano program for the published AD meta-analysis (left), for *Gpx4*$^{fl/fl}$*Camk2aCreER*$^{T2+/+}$ versus *Gpx4*$^{fl/fl}$*Camk2aCreER*$^{T2+/tg}$ mice, 2 weeks after TAM injection (middle), and for *Gpx4*$^{fl/fl}$*Camk2aCreERT2*$^{+/+}$ versus *Gpx4*$^{R152H/fl}$*Camk2aCreERT2*$^{+/tg}$ mice, 4 weeks after TAM injection (right). Comparison of all three networks reveals high similarity of the occurrence of neurodegenerative diseases (i.e., AD, PD, and HD) as well as the direction of their regulation.

See also Figures S7–S10.

Please cite this article in press as: Lorenz et al., A fin-loop-like structure in GPX4 underlies neuroprotection from ferroptosis, Cell (2026), https://doi.org/10.1016/j.cell.2025.11.014

sufficient to preserve function and effectively prevent ferroptosis. Thus, our findings importantly resolve a longstanding question in ferroptosis: how does GPX4 anchor to membranes to detoxify phospholipid hydroperoxides? Although membrane-binding motifs have been described in other lipid-processing enzymes, such as phospholipases, our results now cement GPX4 as the primordial sentinel of lipid peroxidation, which relies on a hydrophobic structural motif to spatially control its function.

Our patient-derived models and conditional knockin mice establish that the *GPX4*^{R152H} variant acts as a hypomorphic allele, insufficient to suppress ferroptosis yet less severe than the biallelic truncating mutations that cause embryonic lethality.[19,20] Using a series of TAM-inducible, neuron-specific *Gpx4* KO or *Gpx4*^{R152H} knockin models, we demonstrate that glutamatergic neurons undergo progressive ferroptosis-driven degeneration, culminating in cortical atrophy, motor impairment, and neuroinflammation. These phenotypes closely phenocopy the clinical presentation of SSMD patients and, more broadly, share the molecular features of neurodegenerative disorders such as AD. Indeed, spatiotemporal proteomic profiling of *Gpx4*-deficient brains revealed a strong convergence with AD-associated signatures, including the strong upregulation of APOE and CLU, alongside other typical immune cell markers. However, despite the induction of astro- and microgliosis that we observed following neuronal ferroptosis, we caution against assuming a universal link between cell death and inflammation. For example, apoptotic cell death during brain development does not trigger an inflammatory reaction, and, similarly, *Gpx4*-null kidneys or liver show moderate levels of inflammation.[14,44] These findings illustrate the context-dependent immunogenicity of cell death and suggest that ferroptotic lipid peroxidation, particularly in the brain, may uniquely disrupt tissue homeostasis. Moreover, we show that *Gpx4*-null mice exhibit protein expression patterns not exclusively shared by AD patients but that overlap with signatures from Huntington's disease (HD), Parkinson's disease (PD), and amyotrophic lateral sclerosis (ALS). This convergence was also observed in ferroptosis-relevant metabolic pathways, including glutathione (GSH), arachidonic acid metabolism, and the pentose phosphate pathway. Together, these shared perturbations propose a broader role for ferroptosis in neurodegeneration, previously hypothesized but now supported by direct *in vivo* evidence. Perhaps it is difficult at this time to address direct comparisons of human AD in its early stages, but our data provide a foundation for the kinds of comparative analyses that will be crucial for eventual therapeutic design. Lastly, as this study does not provide conclusive evidence for either the role of neuroinflammation as a driving force or as a consequence of neurodegeneration, our data demonstrate that ferroptosis is sufficient to trigger a cell-nonautonomous inflammatory tissue reaction. These insights emphasize the pathogenic nature of ferroptosis in the brain and underscore its promise as a therapeutic target across neurodegenerative diseases.

Limitations of the study

This study defines a structural mechanism by which GPX4 correctly positions itself at membranes to prevent ferroptosis, establishing ferroptosis as a central driver of neurodegeneration in the context of an inherited *GPX4*^{R152H} variant. However, several limitations remain. First, although patient-derived iPSC models and conditional mouse genetics enabled interrogation of disease mechanisms in a human-relevant and cell-type-specific context, the embryonic lethality of homozygous *Gpx4*^{R152H} mice hampered our ability to explore developmental contributions and tissue-specific compensation in a constitutive setting. Second, although our structural, biochemical, and proteomic data strongly implicate impaired membrane association as the central pathogenic mechanism, *in vivo* imaging of GPX4 at neuronal membranes is lacking and will be essential to fully define the kinetics and topology of this interaction *in situ*. Third, while neurodegeneration in *Gpx4*-deficient brains captured proteomic and inflammatory signatures reminiscent of human neurodegeneration, the extent to which ferroptosis represents a convergent or distinct pathway in human disease remains unresolved. This, in turn, calls for future studies addressing how the cysteine-GSH-selenium-GPX4 axis might be impaired in neurodegeneration. Finally, although we demonstrate rescue with ferroptosis inhibitors *in vitro* and *in vivo*, pharmacologic targeting of ferroptosis in humans remains untested. Future studies integrating longitudinal *in vivo* imaging, single-cell multi-omics, and translational trial platforms will be crucial for validating the clinical tractability of ferroptosis inhibition in neurodegenerative disorders.

RESOURCE AVAILABILITY

Lead contact

Further information and requests for resources and reagents should be directed to, and will be fulfilled by, the lead contact, Marcus Conrad (marcus.conrad@helmholtz-munich.de).

Materials availability

Reagents, plasmids, and cell and mouse lines generated in this study are available from the lead contact, with a completed materials transfer agreement, upon request.

Data and code availability

- The structure coordinates have been deposited in PDB with accession codes PDB: 9RF1, 8Q8J, 8Q8N.
- This paper does not report original code.
- The mass spectrometry proteomics data have been deposited to the ProteomeXchange Consortium via the PRIDE[45] partner repository with the dataset identifier PXD071158.
- NMR assignments have been deposited in the BMRB under accession codes BMRB: 52110, 52111, 52112, 52113.
- Original western blot images have been deposited at Mendeley (DOI: https://doi.org/10.17632/38hgzfn46t.1) and are publicly available as of the date of publication. Microscopy data reported in this paper will be shared by the lead contact upon request.
- Any additional information required to reanalyze the data reported in this paper is available from the lead contact upon request.

ACKNOWLEDGMENTS

We thank Gunter Schutz and co-workers (DKFZ Heidelberg) for kindly providing the *Camk2aCreER*^{T2} transgenic mice. We are highly indebted to Katja Michaela Boxleitner, Monika Stadler, Jonas Wanninger, and Nicole Fritz for their excellent technical assistance and to all animal caretakers for their invaluable support in animal maintenance. We acknowledge Alexa Bartle for creating the graphical abstract. We also acknowledge the contributions of

Dr. Sibylle Sabrautzki and Dr. Julia Zorn, our animal welfare officers. We are grateful to Dr. Sam Asami and Dr. Gerd Gemmecker (Bavarian NMR Center, BNMRZ Garching) for support with NMR experiments, and we acknowledge the use of the crystallization platform at the Helmholtz Munich. We thank Igor Paron and Mario Oroshi from the Department of Proteomics and Signal Transduction at the MPI for Biochemistry for their excellent mass spectrometry and technical support. All MS-based proteomic studies were supported by the Department of Proteomics and Signal Transduction at the Max Planck Institute for Biochemistry and the Metabolomics and Proteomics Core of Helmholtz Munich. This work was supported by Deutsche Forschungsgemeinschaft (DFG) (CO 291/7-1, # 428858739 and the Priority Program SPP 2306 [CO 291/9-1, #461385412; CO 291/10-1, #461507177]) and PR 1752/3-1 to B. Proneth, as well as the German Federal Ministry of Education and Research (BMBF) VIP+ program NEUROPROTEKT (03VP04260), the BMBF program FERROPATH (B. Proneth) (01EJ2205B), and the European Research Council (ERC) under the European Union's Horizon 2020 research and innovation program (grant agreement no. GA 884754) to M.C. P.V. was supported by the Fond de Recherche Scientifique (F.R.S.-FNRS) (grant 40005227). Z.Z. was supported by an EMBO postdoctoral fellowship (EMBO ALTF 1318-2024) and P.V. was supported by a fellowship from Alexander von Humboldt-Stiftung. A.K.J was supported by DFG Emmy Noether Grant (JA 3274/1-1)

AUTHOR CONTRIBUTIONS

Conceptualization, A.W., G.M.P., I.I., M.J.B., M.C., S.A., S.M.L., S.K.R., T.S., and A.S.D.M.; methodology, A.K.J., B.H., D.C., J.I., M.J.B., and T.S.; formal analysis, A.S.D.M., A.W., D.E., D.T., E.G., E.M., J.I., M.A., M.J.B., M.S., M.S.W., S.M.L., and T.S.; investigation, A.D., A.E.A., A.J.G.-S., A.K.J., A.L., A.M., A.P., A.S.D.M., A.T., A.W., A.Z., B.H., B. Popper, B. Proneth, C. Scale, C. Sieben, D.C., D.E., D.H., D.V.-W., D.F.K., E.B., E.M., E.v.S., F.R., G.E., G.M.P., H.Z., H.F., I.I., J.I., J.M.F., J.K.S., J.M.-P., K.W., L.G., L.P., M.A., M.J.B., M.K., M.K.-A., M.N., M. Soudy, M.S.W., M.V., N.R., P.A., P.S., P.V., S.D., S.G., S.H., S.M.H., S.M.L., T.N., T.O., T.V.B., T.S., and V.N.; resources, G.M.P., J.F., J. Lenberg, K.W., M.C., M.A.F., M.M., M. Sattler, S.H., and S.K.R.; data curation, D.T., A.W., M.S.W., M.J.B., and A.K.J.; writing – original draft, A.W., D.E., D.T., G.M.P., M.C., S.M.L., and M.J.B.; writing – review and editing, A.W., A.S.D.M., M.C., S.M.L., T.S., M.J.B., M. Sattler, A.L., and Z.Z.; visualization, A.K.J., A.L., A.W., M.J.B., S.M.L., and T.S.; supervision, G.M.P., J. Lewerenz, M.C., M.H.d.A., S.H., M. Sattler, and W.W.; project administration, A.W., M.C., S.M.L., and T.S.; funding acquisition, M.C.

DECLARATION OF INTERESTS

M.C. and B. Proneth are co-founders and shareholders of ROSCUE Therapeutics GmbH and hold patents for some of the compounds described herein. M.J.B. is a current employee of AstraZeneca and has stock ownership and/or stock options or interests in the company.

STAR★METHODS

Detailed methods are provided in the online version of this paper and include the following:

- KEY RESOURCES TABLE
- EXPERIMENTAL MODEL AND METHOD DETAILS
  - ○ Patients
  - ○ Animals
  - ○ Cell lines
  - ○ Primary cell cultures
  - ○ iPSC culture
  - ○ Forebrain organoids
- METHOD DETAILS
  - ○ Human participants analysis
  - ○ MR Imaging
  - ○ Body composition
  - ○ Tissue and embryo dissection
  - ○ Hematoxylin and eosin (HE) staining
  - ○ Periodic acid–Schiff (PAS) Reaction
  - ○ Terminal deoxynucleotidyl transferase dUTP nick end labelling (TUNEL) staining
  - ○ Nissl staining
  - ○ Transmission electron microscopy
  - ○ Immunohistochemistry
  - ○ Immunocytochemistry
  - ○ Behavioral tests
  - ○ Measurement of functional blood parameters
  - ○ Single molecule array (Simoa® / Ella-NfL)
  - ○ Subcellular fractionation
  - ○ Reprogramming of *GPX4*-mutated donor fibroblasts
  - ○ Generation of an isogenic control line for the RAGO1 hiPSC line via CRISPR knock-in
  - ○ Differentiation to cortical neurons (CN)
  - ○ Forebrain organoids
  - ○ Generation of lentiviral particles for transduction of mammalian cells
  - ○ Stable expression of N-terminally FLAG-tagged human GPX4 mutants
  - ○ Cell viability assay
  - ○ Live-cell imaging
  - ○ Fluorescence microscopy
  - ○ Quantitative real-time PCR
  - ○ Determination of lipid peroxidation
  - ○ Immunoblotting
  - ○ GPX4 stability analysis
  - ○ Determination of GPX4 activity using affinity-purified enzyme
  - ○ Determination of GPX4 activity in crude cell lysates
  - ○ Isolation of CNS-Infiltrating immune cells and flow cytometry
  - ○ (Oxy)lipidomics analysis
  - ○ Expression of GPX4^{U46C} and mutants
  - ○ Structural analysis
  - ○ Bicelle titrations
  - ○ Structured illumination microscopy (SIM)
  - ○ Neuroproteomic analyses
  - ○ Cell type annotation of proteomics data
- QUANTIFICATION AND STATISTICAL ANALYSIS

SUPPLEMENTAL INFORMATION

Supplemental information can be found online at https://doi.org/10.1016/j.cell.2025.11.014.

Received: March 29, 2024
Revised: July 1, 2025
Accepted: November 6, 2025

REFERENCES

1. Knopman, D.S., Amieva, H., Petersen, R.C., Chételat, G., Holtzman, D.M., Hyman, B.T., Nixon, R.A., and Jones, D.T. (2021). Alzheimer disease. Nat. Rev. Dis. Primers *7*, 33. https://doi.org/10.1038/s41572-021-00269-y.
2. Colonna, M., and Brioschi, S. (2020). Neuroinflammation and neurodegeneration in human brain at single-cell resolution. Nat. Rev. Immunol. *20*, 81–82. https://doi.org/10.1038/s41577-019-0262-0.
3. Lewis, S. (2022). Untangling neurodegeneration. Nat. Rev. Neurosci. *23*, 582–583. https://doi.org/10.1038/s41583-022-00629-x.
4. Wilson, D.M., 3rd, Cookson, M.R., Van Den Bosch, L., Zetterberg, H., Holtzman, D.M., and Dewachter, I. (2023). Hallmarks of neurodegenerative diseases. Cell *186*, 693–714. https://doi.org/10.1016/j.cell.2022.12.032.
5. Cacace, R., Sleegers, K., and Van Broeckhoven, C. (2016). Molecular genetics of early-onset Alzheimer's disease revisited. Alzheimers Dement. *12*, 733–748. https://doi.org/10.1016/j.jalz.2016.01.012.
6. Lambert, J.C., Ibrahim-Verbaas, C.A., Harold, D., Naj, A.C., Sims, R., Bellenguez, C., DeStafano, A.L., Bis, J.C., Beecham, G.W., Grenier-Boley, B.,

et al. (2013). Meta-analysis of 74,046 individuals identifies 11 new susceptibility loci for Alzheimer's disease. Nat. Genet. *45*, 1452–1458. https://doi.org/10.1038/ng.2802.

7. Gatz, M., Reynolds, C.A., Fratiglioni, L., Johansson, B., Mortimer, J.A., Berg, S., Fiske, A., and Pedersen, N.L. (2006). Role of genes and environments for explaining Alzheimer disease. Arch. Gen. Psychiatry *63*, 168–174. https://doi.org/10.1001/archpsyc.63.2.168.
8. Karran, E., Mercken, M., and De Strooper, B. (2011). The amyloid cascade hypothesis for Alzheimer's disease: an appraisal for the development of therapeutics. Nat. Rev. Drug Discov. *10*, 698–712. https://doi.org/10.1038/nrd3505.
9. Moujalled, D., Strasser, A., and Liddell, J.R. (2021). Molecular mechanisms of cell death in neurological diseases. Cell Death Differ. *28*, 2029–2044. https://doi.org/10.1038/s41418-021-00814-y.
10. Korczyn, A.D., and Grinberg, L.T. (2024). Is Alzheimer disease a disease? Nat. Rev. Neurol. *20*, 245–251. https://doi.org/10.1038/s41582-024-00940-4.
11. Wright, C.F., FitzPatrick, D.R., and Firth, H.V. (2018). Paediatric genomics: diagnosing rare disease in children. Nat. Rev. Genet. *19*, 253–268. https://doi.org/10.1038/nrg.2017.116.
12. Yang, W.S., SriRamaratnam, R., Welsch, M.E., Shimada, K., Skouta, R., Viswanathan, V.S., Cheah, J.H., Clemons, P.A., Shamji, A.F., Clish, C.B., et al. (2014). Regulation of ferroptotic cancer cell death by GPX4. Cell *156*, 317–331. https://doi.org/10.1016/j.cell.2013.12.010.
13. Seiler, A., Schneider, M., Förster, H., Roth, S., Wirth, E.K., Culmsee, C., Plesnila, N., Kremmer, E., Rådmark, O., Wurst, W., et al. (2008). Glutathione peroxidase 4 senses and translates oxidative stress into 12/15-lipoxygenase dependent- and AIF-mediated cell death. Cell Metab. *8*, 237–248. https://doi.org/10.1016/j.cmet.2008.07.005.
14. Friedmann Angeli, J.P., Schneider, M., Proneth, B., Tyurina, Y.Y., Tyurin, V.A., Hammond, V.J., Herbach, N., Aichler, M., Walch, A., Eggenhofer, E., et al. (2014). Inactivation of the ferroptosis regulator Gpx4 triggers acute renal failure in mice. Nat. Cell Biol. *16*, 1180–1191. https://doi.org/10.1038/ncb3064.
15. Dixon, S.J., Lemberg, K.M., Lamprecht, M.R., Skouta, R., Zaitsev, E.M., Gleason, C.E., Patel, D.N., Bauer, A.J., Cantley, A.M., Yang, W.S., et al. (2012). Ferroptosis: an iron-dependent form of nonapoptotic cell death. Cell *149*, 1060–1072. https://doi.org/10.1016/j.cell.2012.03.042.
16. Zheng, J., and Conrad, M. (2025). Ferroptosis: when metabolism meets cell death. Physiol. Rev. *105*, 651–706. https://doi.org/10.1152/physrev.00031.2024.
17. Conrad, M., and Wahida, A. (2025). The many paths ascending to ferroptosis. Nat. Chem. Biol. *21*, 18–19. https://doi.org/10.1038/s41589-024-01794-z.
18. Dixon, S.J., and Olzmann, J.A. (2024). The cell biology of ferroptosis. Nat. Rev. Mol. Cell Biol. *25*, 424–442. https://doi.org/10.1038/s41580-024-00703-5.
19. Smith, A.C., Mears, A.J., Bunker, R., Ahmed, A., MacKenzie, M., Schwartzentruber, J.A., Beaulieu, C.L., Ferretti, E., , et al.; FORGE Canada Consortium, and Majewski, J. (2014). Mutations in the enzyme glutathione peroxidase 4 cause Sedaghatian-type spondylometaphyseal dysplasia. J. Med. Genet. *51*, 470–474. https://doi.org/10.1136/jmedgenet-2013-102218.
20. Sedaghatian, M.R. (1980). Congenital lethal metaphyseal chondrodysplasia: a newly recognized complex autosomal recessive disorder. Am. J. Med. Genet. *6*, 269–274. https://doi.org/10.1002/ajmg.1320060403.
21. Ingold, I., Berndt, C., Schmitt, S., Doll, S., Poschmann, G., Buday, K., Roveri, A., Peng, X., Porto Freitas, F., Seibt, T., et al. (2018). Selenium utilization by GPX4 is required to prevent hydroperoxide-induced ferroptosis. Cell *172*, 409–422.e21. https://doi.org/10.1016/j.cell.2017.11.048.
22. Liu, H., Forouhar, F., Seibt, T., Saneto, R., Wigby, K., Friedman, J., Xia, X., Shchepinov, M.S., Ramesh, S.K., Conrad, M., et al. (2022). Characterization of a patient-derived variant of GPX4 for precision therapy. Nat. Chem. Biol. *18*, 91–100. https://doi.org/10.1038/s41589-021-00915-2.
23. Padmanabhan Nair, V., Liu, H., Ciceri, G., Jungverdorben, J., Frishman, G., Tchieu, J., Cederquist, G.Y., Rothenaigner, I., Schorpp, K., Klepper, L., et al. (2021). Activation of HERV-K(HML-2) disrupts cortical patterning and neuronal differentiation by increasing NTRK3. Cell Stem Cell *28*, 1566–1581.e8. https://doi.org/10.1016/j.stem.2021.04.009.
24. Tschuck, J., Padmanabhan Nair, V., Galhoz, A., Zaratiegui, C., Tai, H.-M., Ciceri, G., Rothenaigner, I., Tchieu, J., Stockwell, B.R., Studer, L., et al. (2024). Suppression of ferroptosis by vitamin A or radical-trapping antioxidants is essential for neuronal development. Nat. Commun. *15*, 7611. https://doi.org/10.1038/s41467-024-51996-1.
25. Yant, L.J., Ran, Q., Rao, L., Van Remmen, H., Shibatani, T., Belter, J.G., Motta, L., Richardson, A., and Prolla, T.A. (2003). The selenoprotein GPX4 is essential for mouse development and protects from radiation and oxidative damage insults. Free Radic. Biol. Med. *34*, 496–502. https://doi.org/10.1016/S0891-5849(02)01360-6.
26. Kagan, V.E., Mao, G., Qu, F., Angeli, J.P.F., Doll, S., Croix, C.S., Dar, H.H., Liu, B., Tyurin, V.A., Ritov, V.B., et al. (2017). Oxidized arachidonic and adrenic PEs navigate cells to ferroptosis. Nat. Chem. Biol. *13*, 81–90. https://doi.org/10.1038/nchembio.2238.
27. Mishima, E., Ito, J., Wu, Z., Nakamura, T., Wahida, A., Doll, S., Tonnus, W., Nepachalovich, P., Eggenhofer, E., Aldrovandi, M., et al. (2022). A non-canonical vitamin K cycle is a potent ferroptosis suppressor. Nature *608*, 778–783. https://doi.org/10.1038/s41586-022-05022-3.
28. Nakamura, T., Hipp, C., Santos Dias Mourão, A., Borggräfe, J., Aldrovandi, M., Henkelmann, B., Wanninger, J., Mishima, E., Lytton, E., Emler, D., et al. (2023). Phase separation of FSP1 promotes ferroptosis. Nature *619*, 371–377. https://doi.org/10.1038/s41586-023-06255-6.
29. Nakamura, T., Ito, J., Mourão, A.S.D., Wahida, A., Nakagawa, K., Mishima, E., and Conrad, M. (2024). A tangible method to assess native ferroptosis suppressor activity. Cell Rep. Methods *4*, 100710. https://doi.org/10.1016/j.crmeth.2024.100710.
30. Ito, J., Nakamura, T., Toyama, T., Chen, D., Berndt, C., Poschmann, G., Mourão, A.S.D., Doll, S., Suzuki, M., Zhang, W., et al. (2024). PRDX6 dictates ferroptosis sensitivity by directing cellular selenium utilization. Mol. Cell *84*, 4629–4644.e9. https://doi.org/10.1016/j.molcel.2024.10.028.
31. Ito, J., Nakagawa, K., Kato, S., Hirokawa, T., Kuwahara, S., Nagai, T., and Miyazawa, T. (2015). Direct separation of the diastereomers of phosphatidylcholine hydroperoxide bearing 13-hydroperoxy-9Z,11E-octadecadienoic acid using chiral stationary phase high-performance liquid chromatography. J. Chromatogr. A *1386*, 53–61. https://doi.org/10.1016/j.chroma.2015.01.080.
32. Scheerer, P., Borchert, A., Krauss, N., Wessner, H., Gerth, C., Höhne, W., and Kuhn, H. (2007). Structural basis for catalytic activity and enzyme polymerization of phospholipid hydroperoxide glutathione peroxidase-4 (GPx4). Biochemistry *46*, 9041–9049. https://doi.org/10.1021/bi700840d.
33. Labrecque, C.L., and Fuglestad, B. (2021). Electrostatic drivers of GPx4 interactions with membrane, lipids, and DNA. Biochemistry *60*, 2761–2772. https://doi.org/10.1021/acs.biochem.1c00492.
34. Dürr, U.H.N., Gildenberg, M., and Ramamoorthy, A. (2012). The magic of bicelles lights up membrane protein structure. Chem. Rev. *112*, 6054–6074. https://doi.org/10.1021/cr300061w.
35. Warschawski, D.E., Arnold, A.A., Beaugrand, M., Gravel, A., Chartrand, É., and Marcotte, I. (2011). Choosing membrane mimetics for NMR structural studies of transmembrane proteins. Biochim. Biophys. Acta *1808*, 1957–1974. https://doi.org/10.1016/j.bbamem.2011.03.016.
36. Cozza, G., Rossetto, M., Bosello-Travain, V., Maiorino, M., Roveri, A., Toppo, S., Zaccarin, M., Zennaro, L., and Ursini, F. (2017). Glutathione peroxidase 4-catalyzed reduction of lipid hydroperoxides in membranes: The polar head of membrane phospholipids binds the enzyme and addresses the fatty acid hydroperoxide group toward the redox center.

Please cite this article in press as: Lorenz et al., A fin-loop-like structure in GPX4 underlies neuroprotection from ferroptosis, Cell (2026), https://doi.org/10.1016/j.cell.2025.11.014

Free Radic. Biol. Med. *112*, 1–11. https://doi.org/10.1016/j.freeradbiomed.2017.07.010.

37. Wirth, E.K., Bharathi, B.S., Hatfield, D., Conrad, M., Brielmeier, M., and Schweizer, U. (2014). Cerebellar hypoplasia in mice lacking selenoprotein biosynthesis in neurons. Biol. Trace Elem. Res. *158*, 203–210. https://doi.org/10.1007/s12011-014-9920-z.

38. Coppens, S., Lehmann, S., Hopley, C., and Hirtz, C. (2023). Neurofilament-light, a promising biomarker: Analytical, metrological and clinical challenges. Int. J. Mol. Sci. *24*, 11624. https://doi.org/10.3390/ijms241411624.

39. Yuan, A., and Nixon, R.A. (2021). Neurofilament proteins as biomarkers to monitor neurological diseases and the efficacy of therapies. Front. Neurosci. *15*, 689938. https://doi.org/10.3389/fnins.2021.689938.

40. Hofmann, A., Häsler, L.M., Lambert, M., Kaeser, S.A., Gräber-Sultan, S., Obermüller, U., Kuder-Buletta, E., la Fougere, C., Laske, C., Vöglein, J., et al. (2024). Comparative neurofilament light chain trajectories in CSF and plasma in autosomal dominant Alzheimer's disease. Nat. Commun. *15*, 9982. https://doi.org/10.1038/s41467-024-52937-8.

41. Keren-Shaul, H., Spinrad, A., Weiner, A., Matcovitch-Natan, O., Dvir-Szternfeld, R., Ulland, T.K., David, E., Baruch, K., Lara-Astaiso, D., Toth, B., et al. (2017). A unique microglia type associated with restricting development of Alzheimer's disease. Cell *169*, 1276–1290.e17. https://doi.org/10.1016/j.cell.2017.05.018.

42. Leng, F., and Edison, P. (2021). Neuroinflammation and microglial activation in Alzheimer disease: where do we go from here? Nat. Rev. Neurol. *17*, 157–172. https://doi.org/10.1038/s41582-020-00435-y.

43. Tastan, B., and Heneka, M.T. (2024). The impact of neuroinflammation on neuronal integrity. Immunol. Rev. *327*, 8–32. https://doi.org/10.1111/imr.13419.

44. White, L.D., and Barone, S., Jr. (2001). Qualitative and quantitative estimates of apoptosis from birth to senescence in the rat brain. Cell Death Differ. *8*, 345–356. https://doi.org/10.1038/sj.cdd.4400816.

45. Perez-Riverol, Y., Bandla, C., Kundu, D.J., Kamatchinathan, S., Bai, J., Hewapathirana, S., John, N.S., Prakash, A., Walzer, M., Wang, S., and Vizcaíno, J.A. (2025). The PRIDE database at 20 years: 2025 update. Nucleic Acids Res *53*, D543–D553. https://doi.org/10.1093/nar/gkae1011.

46. Doll, S., Freitas, F.P., Shah, R., Aldrovandi, M., da Silva, M.C., Ingold, I., Goya Grocin, A., Xavier da Silva, T.N., Panzilius, E., Scheel, C.H., et al. (2019). FSP1 is a glutathione-independent ferroptosis suppressor. Nature *575*, 693–698. https://doi.org/10.1038/s41586-019-1707-0.

47. Hameyer, D., Loonstra, A., Eshkind, L., Schmitt, S., Antunes, C., Groen, A., Bindels, E., Jonkers, J., Krimpenfort, P., Meuwissen, R., et al. (2007). Toxicity of ligand-dependent Cre recombinases and generation of a conditional Cre deleter mouse allowing mosaic recombination in peripheral tissues. Physiol. Genomics *31*, 32–41. https://doi.org/10.1152/physiolgenomics.00019.2007.

48. Casanova, E., Fehsenfeld, S., Mantamadiotis, T., Lemberger, T., Greiner, E., Stewart, A.F., and Schütz, G. (2001). A CamKIIα iCre BAC allows brain-specific gene inactivation: CamKIIα iCre BAC Allows Brain-Specific Gene Inactivation. Genesis *31*, 37–42. https://doi.org/10.1002/gene.1078.

49. Uus, A., Zhang, T., Jackson, L.H., Roberts, T.A., Rutherford, M.A., Hajnal, J.V., and Deprez, M. (2020). Deformable Slice-to-Volume Registration for Motion Correction of Fetal Body and Placenta MRI. IEEE Trans. Med. Imaging. *39*, 2750–2759. https://doi.org/10.1109/TMI.2020.2974844.

50. Fedorov, A., Beichel, R., Kalpathy-Cramer, J., Finet, J., Fillion-Robin, J.-C., Pujol, S., Bauer, C., Jennings, D., Fennessy, F., Sonka, M., et al. (2012). 3D Slicer as an image computing platform for the Quantitative Imaging Network. Magn. Reson. Imaging *30*, 1323–1341. https://doi.org/10.1016/j.mri.2012.05.001.

51. Pang, Z., Chong, J., Zhou, G., de Lima Morais, D.A., Chang, L., Barrette, M., Gauthier, C., Jacques, P.-É., Li, S., and Xia, J. (2021). MetaboAnalyst 5.0: narrowing the gap between raw spectra and functional insights. Nucleic Acids Res. *49*, W388–W396. https://doi.org/10.1093/nar/gkab382.

52. Kabsch, W. (2010). XDS. Acta Crystallogr., D *66*, 125–132. https://doi.org/10.1107/S0907444909047337.

53. Evans, P.R., and Murshudov, G.N. (2013). How good are my data and what is the resolution? Acta Crystallogr., D *69*, 1204–1214. https://doi.org/10.1107/S0907444913000061.

54. McCoy, A.J., Grosse-Kunstleve, R.W., Adams, P.D., Winn, M.D., Storoni, L.C., and Read, R.J. (2007). Phaser crystallographic software. J. Appl. Crystallogr. *40*, 658–674. https://doi.org/10.1107/S0021889807021206.

55. Emsley, P., Lohkamp, B., Scott, W.G., and Cowtan, K. (2010). Features and development of coot. Acta Crystallogr., D *66*, 486–501. https://doi.org/10.1107/S0907444910007493.

56. Murshudov, G.N., Vagin, A.A., and Dodson, E.J. (1997). Refinement of macromolecular structures by the maximum-likelihood method. Acta Crystallogr., D *53*, 240–255. https://doi.org/10.1107/S0907444996012255.

57. Afonine, P.V., Grosse-Kunstleve, R.W., Echols, N., Headd, J.J., Moriarty, N.W., Mustyakimov, M., Terwilliger, T.C., Urzhumtsev, A., Zwart, P.H., and Adams, P.D. (2012). Towards automated crystallographic structure refinement with phenix.refine. Acta Crystallogr., D *68*, 352–367. https://doi.org/10.1107/S0907444912001308.

58. Bostock, M.J., Holland, D.J., and Nietlispach, D. (2012). Compressed sensing reconstruction of undersampled 3D NOESY spectra: application to large membrane proteins. J. Biomol. NMR *54*, 15–32. https://doi.org/10.1007/s10858-012-9643-4.

59. Vranken, W.F., Boucher, W., Stevens, T.J., Fogh, R.H., Pajon, A., Llinas, M., Ulrich, E.L., Markley, J.L., Ionides, J., and Laue, E.D. (2005). The CCPN data model for NMR spectroscopy: development of a software pipeline. Proteins *59*, 687–696. https://doi.org/10.1002/prot.20449.

60. Tyanova, S., Temu, T., Sinitcyn, P., Carlson, A., Hein, M.Y., Geiger, T., Mann, M., and Cox, J. (2016). The Perseus computational platform for comprehensive analysis of (prote)omics data. Nat. Methods *13*, 731–740. https://doi.org/10.1038/nmeth.3901.

61. Cox, J., and Mann, M. (2008). MaxQuant enables high peptide identification rates, individualized p.p.b.-range mass accuracies and proteome-wide protein quantification. Nat. Biotechnol. *26*, 1367–1372. https://doi.org/10.1038/nbt.1511.

62. Cox, J., Hein, M.Y., Luber, C.A., Paron, I., Nagaraj, N., and Mann, M. (2014). Accurate proteome-wide label-free quantification by delayed normalization and maximal peptide ratio extraction, termed MaxLFQ. Mol. Cell. Proteomics *13*, 2513–2526. https://doi.org/10.1074/mcp.M113.031591.

63. Lê, S., Josse, J., and Husson, F. (2008). FactoMineR: An R Package for Multivariate Analysis. J. Stat. Softw. *25*, 1–18. https://doi.org/10.18637/jss.v025.i01.

64. Gu, Z., Eils, R., and Schlesner, M. (2016). Complex heatmaps reveal patterns and correlations in multidimensional genomic data. Bioinformatics *32*, 2847–2849. https://doi.org/10.1093/bioinformatics/btw313.

65. Smedley, D., Haider, S., Durinck, S., Pandini, L., Provero, P., Allen, J., Arnaiz, O., Awedh, M.H., Baldock, R., Barbiera, G., et al. (2015). The BioMart community portal: an innovative alternative to large, centralized data repositories. Nucleic Acids Res. *43*, W589–W598. https://doi.org/10.1093/nar/gkv350.

66. Yu, G., Wang, L.-G., Han, Y., and He, Q.-Y. (2012). clusterProfiler: an R package for comparing biological themes among gene clusters. Omics *16*, 284–287. https://doi.org/10.1089/omi.2011.0118.

67. Liberzon, A., Birger, C., Thorvaldsdóttir, H., Ghandi, M., Mesirov, J.P., and Tamayo, P. (2015). The Molecular Signatures Database (MSigDB) hallmark gene set collection. Cell Syst. *1*, 417–425. https://doi.org/10.1016/j.cels.2015.12.004.

68. Balduzzi, S., Rücker, G., and Schwarzer, G. (2019). How to perform a meta-analysis with R: a practical tutorial. Evid. Based Ment. Health *22*, 153–160. https://doi.org/10.1136/ebmental-2019-300117.

69. Kanehisa, M., Furumichi, M., Sato, Y., Kawashima, M., and Ishiguro-Watanabe, M. (2023). KEGG for taxonomy-based analysis of pathways and

Please cite this article in press as: Lorenz et al., A fin-loop-like structure in GPX4 underlies neuroprotection from ferroptosis, Cell (2026), https://doi.org/10.1016/j.cell.2025.11.014

genomes. Nucleic Acids Res. *51*, D587–D592. https://doi.org/10.1093/nar/gkac963.

70. Langfelder, P., and Horvath, S. (2008). WGCNA: an R package for weighted correlation network analysis. BMC Bioinform. *9*, 559. https://doi.org/10.1186/1471-2105-9-559.
71. Franzén, O., Gan, L.-M., and Björkegren, J.L.M. (2019). PanglaoDB: a web server for exploration of mouse and human single-cell RNA sequencing data. Database (Oxford) *2019*, baz046. https://doi.org/10.1093/database/baz046.
72. Erdmann, G., Schütz, G., and Berger, S. (2007). Inducible gene inactivation in neurons of the adult mouse forebrain. BMC Neurosci. *8*, 63. https://doi.org/10.1186/1471-2202-8-63.
73. Barski, J.J., Dethleffsen, K., and Meyer, M. (2000). Cre recombinase expression in cerebellar Purkinje cells. Genesis *28*, 93–98. https://doi.org/10.1002/1526-968X(200011/12)28:3/4<93::AID-GENE10>3.0.CO;2-W.
74. Kuklisova-Murgasova, M., Quaghebeur, G., Rutherford, M.A., Hajnal, J.V., and Schnabel, J.A. (2012). Reconstruction of fetal brain MRI with intensity matching and complete outlier removal. Med. Image Anal. *16*, 1550–1564. https://doi.org/10.1016/j.media.2012.07.004.
75. Fuchs, H., Aguilar-Pimentel, J.A., Amarie, O.V., Becker, L., Calzada-Wack, J., Cho, Y.-L., Garrett, L., Hölter, S.M., Irmler, M., Kistler, M., et al. (2018). Understanding gene functions and disease mechanisms: Phenotyping pipelines in the German Mouse Clinic. Behav. Brain Res. *352*, 187–196. https://doi.org/10.1016/j.bbr.2017.09.048.
76. Hölter, S.M., Garrett, L., Einicke, J., Sperling, B., Dirscherl, P., Zimprich, A., Fuchs, H., Gailus-Durner, V., Hrabě de Angelis, M., and Wurst, W. (2015). Assessing cognition in mice. Curr. Protoc. Mouse Biol. *5*, 331–358. https://doi.org/10.1002/9780470942390.mo150068.
77. Garrett, L., Zhang, J., Zimprich, A., Niedermeier, K.M., Fuchs, H., Gailus-Durner, V., Hrabě de Angelis, M., Vogt Weisenhorn, D., Wurst, W., and Hölter, S.M. (2015). Conditional reduction of adult born doublecortin-positive neurons reversibly impairs selective behaviors. Front. Behav. Neurosci. *9*, 302. https://doi.org/10.3389/fnbeh.2015.00302.
78. Kabiri, Y., Eberhagen, C., Schmitt, S., Knolle, P.A., and Zischka, H. (2021). Isolation and electron microscopic analysis of liver cancer cell mitochondria. Methods Mol. Biol. *2277*, 277–287. https://doi.org/10.1007/978-1-0716-1270-5_17.
79. Shi, Y., Kirwan, P., and Livesey, F.J. (2012). Directed differentiation of human pluripotent stem cells to cerebral cortex neurons and neural networks. Nat. Protoc. *7*, 1836–1846. https://doi.org/10.1038/nprot.2012.116.
80. Matyash, V., Liebisch, G., Kurzchalia, T.V., Shevchenko, A., and Schwudke, D. (2008). Lipid extraction by methyl-tert-butyl ether for high-throughput lipidomics. J. Lipid Res. *49*, 1137–1146. https://doi.org/10.1194/jlr.D700041-JLR200.
81. Chong, J., Wishart, D.S., and Xia, J. (2019). Using MetaboAnalyst 4.0 for comprehensive and integrative metabolomics data analysis. Curr. Protoc. Bioinform. *68*, e86. https://doi.org/10.1002/cpbi.86.
82. Bracher, A., Morozov, V., and Mourao, A. (2018). Munich Crystallography BAG (European Synchrotron Radiation Facility). https://doi.org/10.15151/ESRF-ES-2113997880.
83. Agirre, J., Atanasova, M., Bagdonas, H., Ballard, C.B., Baslé, A., Beilsten-Edmands, J., Borges, R.J., Brown, D.G., Burgos-Mármol, J.J., Berrisford, J.M., et al. (2023). The CCP4 suite: integrative software for macromolecular crystallography. Acta Crystallogr. D Struct. Biol. *79*, 449–461. https://doi.org/10.1107/S2059798323003595.
84. Sattler, M., Schleucher, J., and Griesinger, C. (1999). Heteronuclear multidimensional NMR experiments for the structure determination of proteins in solution employing pulsed field gradients. Prog. Nucl. Magn. Reson. Spectrosc. *34*, 93–158. https://doi.org/10.1016/S0079-6565(98)00025-9.
85. Farrow, N.A., Muhandiram, R., Singer, A.U., Pascal, S.M., Kay, C.M., Gish, G., Shoelson, S.E., Pawson, T., Forman-Kay, J.D., and Kay, L.E. (1994). Backbone dynamics of a free and phosphopeptide-complexed Src homology 2 domain studied by 15N NMR relaxation. Biochemistry *33*, 5984–6003. https://doi.org/10.1021/bi00185a040.
86. Gaussmann, S., Gopalswamy, M., Eberhardt, M., Reuter, M., Zou, P., Schliebs, W., Erdmann, R., and Sattler, M. (2021). Membrane interactions of the peroxisomal proteins PEX5 and PEX14. Front. Cell Dev. Biol. *9*, 651449. https://doi.org/10.3389/fcell.2021.651449.
87. Chaney, L.K., and Jacobson, B.S. (1983). Coating cells with colloidal silica for high yield isolation of plasma membrane sheets and identification of transmembrane proteins. J. Biol. Chem. *258*, 10062–10072. https://doi.org/10.1016/S0021-9258(17)44606-0.
88. Paparelli, L., Corthout, N., Pavie, B., Wakefield, D.L., Sannerud, R., Jovanovic-Talisman, T., Annaert, W., and Munck, S. (2016). Inhomogeneity based characterization of distribution patterns on the plasma membrane. PLoS Comput. Biol. *12*, e1005095. https://doi.org/10.1371/journal.pcbi.1005095.
89. Escamilla-Ayala, A.A., Sannerud, R., Mondin, M., Poersch, K., Vermeire, W., Paparelli, L., Berlage, C., Koenig, M., Chavez-Gutierrez, L., Ulbrich, M.H., et al. (2020). Super-resolution microscopy reveals majorly mono- and dimeric presenilin1/γ-secretase at the cell surface. eLife *9*, e56679. https://doi.org/10.7554/eLife.56679.
90. Schindelin, J., Arganda-Carreras, I., Frise, E., Kaynig, V., Longair, M., Pietzsch, T., Preibisch, S., Rueden, C., Saalfeld, S., Schmid, B., et al. (2012). Fiji: an open-source platform for biological-image analysis. Nat. Methods *9*, 676–682. https://doi.org/10.1038/nmeth.2019.
91. Kulak, N.A., Geyer, P.E., and Mann, M. (2017). Loss-less nano-fractionator for high sensitivity, high coverage proteomics. Mol. Cell. Proteomics *16*, 694–705. https://doi.org/10.1074/mcp.O116.065136.
92. R Core Team (2022). R: A Language and Environment for Statistical Computing (R Foundation for Statistical Computing). www.r-project.org.
93. Benjamini, Y., and Hochberg, Y. (1995). Controlling the false discovery rate: A practical and powerful approach to multiple testing. J. R. Stat. Soc. B *57*, 289–300. https://doi.org/10.1111/j.2517-6161.1995.tb02031.x.
94. Trümbach, D., Graf, C., Pütz, B., Kühne, C., Panhuysen, M., Weber, P., Holsboer, F., Wurst, W., Welzl, G., and Deussing, J.M. (2010). Deducing corticotropin-releasing hormone receptor type 1 signaling networks from gene expression data by usage of genetic algorithms and graphical Gaussian models. BMC Syst. Biol. *4*, 159. https://doi.org/10.1186/1752-0509-4-159.
95. Frisch, M., Klocke, B., Haltmeier, M., and Frech, K. (2009). LitInspector: literature and signal transduction pathway mining in PubMed abstracts. Nucleic Acids Res. *37*, W135–W140. https://doi.org/10.1093/nar/gkp303.
96. Berriz, G.F., King, O.D., Bryant, B., Sander, C., and Roth, F.P. (2003). Characterizing gene sets with FuncAssociate. Bioinformatics *19*, 2502–2504. https://doi.org/10.1093/bioinformatics/btg363.
97. Haytural, H., Benfeitas, R., Schedin-Weiss, S., Bereczki, E., Rezeli, M., Unwin, R.D., Wang, X., Dammer, E.B., Johnson, E.C.B., Seyfried, N.T., et al. (2021). Insights into the changes in the proteome of Alzheimer disease elucidated by a meta-analysis. Sci. Data *8*, 312. https://doi.org/10.1038/s41597-021-01090-8.
98. Väremo, L., Nielsen, J., and Nookaew, I. (2013). Enriching the gene set analysis of genome-wide data by incorporating directionality of gene expression and combining statistical hypotheses and methods. Nucleic Acids Res. *41*, 4378–4391. https://doi.org/10.1093/nar/gkt111.
99. L.M. Surhone, M.T. Tennoe, and S.F. Henssonow, eds. (2010). Uniprot (Betascript Publishing).

Please cite this article in press as: Lorenz et al., A fin-loop-like structure in GPX4 underlies neuroprotection from ferroptosis, Cell (2026), https://doi.org/10.1016/j.cell.2025.11.014

STAR★METHODS

KEY RESOURCES TABLE

REAGENT or RESOURCE	SOURCE	IDENTIFIER
Antibodies		
Rat anti-CTIP2	Abcam	Cat# ab18465; RRID:AB_2064130
Rat anti-xCT/SLC7A11	This paper	N/A
Rabbit anti-GFAP	Abcam	Cat# ab7260; RRID:AB_305808
Rabbit anti-IBA1	Genetex	Cat# GTX100042; RRID:AB_1240434
Rabbit anti-IBA1	Abcam	Cat# ab178846; RRID:AB_2636859
Rabbit anti-GPX4	Abcam	Cat# ab125066; RRID:AB_10973901
Rabbit anti-VCP	Abcam	Cat# ab109240; RRID:AB_10862588
Rabbit anti-NfL	Cell signaling	Cat# 2837S; RRID:AB_823575
Rabbit anti-VDAC	Cell signaling	Cat# 4866; RRID:AB_2272627
Rabbit anti-LAMP2 (D5C2P)	Cell signaling	Cat# 49067; RRID:AB_2799349
Rabbit anti-PMP70	ThermoFisher	Cat# PA1-650; RRID:AB_2219912
Rabbit anti-Oct4a (C30A3)	Cell Signaling	Cat# 2840S; RRID:AB_2167691
Rabbit anti-Sox2 (D6D9)	Cell Signaling	Cat# 3579S; RRID:AB_2195767
Rabbit anti-Nanog (D73G4)	Cell Signaling	Cat# 4903S; RRID:AB_10559205
Rabbit anti-Lin28A (A177)	Cell Signaling	Cat# 3978S; RRID:AB_2297060
Rabbit anti-NeuN	Cell Signalling	Cat# 24307S; RRID:AB_2651140
Rabbit anti-CUX1	Biomol	Cat# HPA003277; RRID:AB_10601804
Rabbit anti-TUJ	Cell Signalling	Cat# 5568S; RRID:AB_10694505
Mouse anti-TIM-1/KIM-1/HAVCR	R&D Systems	Cat# AF1817; RRID:AB_2116446
Mouse anti-Anti-4-Hydroxy-2-nonenal (4-HNE)	JaICA	Cat# MHN-020P; RRID:AB_3096486
Mouse anti-HuC/HuC	Invitrogen	Cat# A21271; RRID:AB_221448
Mouse anti-Calbindin	Sigma-Aldrich	Cat# C9848; RRID:AB_476894
Mouse anti-BiP/GRP78	BD Transduction Laboratories	Cat# 610978; RRID:AB_398291
Mouse anti-Sodium Potassium ATPase Alpha 1	Novus	Cat# NB300-146; RRID:AB_2060979
Mouse anti-MAP2	Chemicon	Cat# MAB3418, RRID:AB_94856
Mouse anti-NeuN	Sigma-Aldrich	Cat# MAB377; RRID:AB_2298772
Mouse anti-VCP	Abcam	Cat# ab11433; RRID:AB_298039
Chicken anti-GFAP	Invitrogen	Cat# PA110004; RRID:AB_1074620
Goat anti-rat IgG H&L Alexa Fluor® 488	Abcam	Cat# ab150157; RRID:AB_2722511
Goat anti-chicken Alexa Fluor® 488	ThermoFisher Scientific	Cat# A32931; RRID:AB_2762843
Goat anti-mouse Alexa Fluor® 488	Invitrogen	Cat# A11001; RRID:AB_2534069
Goat anti-mouse Alexa Fluor® 647	Abcam	Cat# ab150115; RRID:AB_2687948
Donkey anti-rabbit Alexa Fluor® 594	ThermoFisher Scientific	Cat# A21207; RRID:AB_141637
Donkey anti-rabbit Alexa Fluor® 555	ThermoFisher Scientific	Cat# A31572; RRID:AB_162543
Donkey anti-rabbit Alexa Fluor® 488	Invitrogen	Cat# 21206; RRID:AB_2535792
Donkey anti-mouse Alexa Fluor® 555	ThermoFisher Scientific	Cat# A31570; RRID:AB_2536180
Donkey anti-rat Alexa Fluor® 488	Invitrogen	Cat# A21208; RRID:AB_2535794
Donkey anti-goat IgG H&L (Biotin)	Abcam	Cat# ab208000; RRID:AB_2923158
Goat anti-rabbit-IgG (Biotin)	Vector Laboratories	Cat# BA-1000; RRID:AB_2313606
Goat anti-rabbit HRP-conjugated	Santa Cruz	Cat# SC-2030; RRID:AB_631747
Goat anti-mouse-IgG (Biotin)	Vector Laboratories	Cat# BA-9200; RRID:AB_2336171
Goat anti-mouse HRP-conjugated	Santa Cruz	Cat# SC-2031; RRID:AB_631737

(*Continued on next page*)

Please cite this article in press as: Lorenz et al., A fin-loop-like structure in GPX4 underlies neuroprotection from ferroptosis, Cell (2026), https://doi.org/10.1016/j.cell.2025.11.014

Continued

REAGENT or RESOURCE	SOURCE	IDENTIFIER
Chemicals, peptides, and recombinant proteins		
Tamoxifen (TAM)	Sigma	T5648; CAS: 10540-29-1
Normal Goat Serum	Cell Signaling	5425
Dulbecco's modified Eagle's medium (DMEM), high glucose, pyruvate, no glutamine	Gibco	21969035
Fetal bovine serum (FBS)	Gibco	2177353
Trolox	Thermo Scientific Acros	10782831; CAS: 53188-07-1
Liproxstatin-1 (Lip-1)	Selleckchem	S7699; CAS: 950455-15-9
4-hydroxytamoxifen (4-hydroxy-TAM)	Sigma-Aldrich	SIALH7904; CAS: 68047-06-3
StemMACS iPS-Brew medium	Miltenyi Biotec	130-104-368
StemMACS Passaging Solution XF	Miltenyi Biotec	130-104-688
Y-27632 dihydrochloride	Tocris	1254; CAS: 129830-38-2
Insulin solution human recombinant	Sigma-Aldrich	I9278
LDN	TargetMol Chemicals Inc.	001594962; CAS: 1062368-24-4
StemMACS SB431542 in Solution	Miltenyi Biotec	130-106-543
Mouse Laminin	Sigma Aldrich	SIALL2020; CAS: 114956-81-9
FGF2	Miltenyi Biotec	130-093-838
Human BDNF	Miltenyi Biotec	130-093-811
StemMACs iPS-Brew XF	Miltenyi Biotec	130-104-368
Accutase	Gibco	A1110501
Y-27632	Miltenyi Biotec	130-103-922
SB-431542	Hycultec	HY-10431
XAV939	Tocris	3748
B27-AO	Thermo Fisher Scientific	10889038
Neg-50	Epredia	6502B
PEI MAX®	Polysciences Europe GmbH	24765-100
AquaBluer	MultiTarget Pharmaceuticals, LLC	6015
BODIPY™ 581/591 C11	Invitrogen	D3861
RSL3 1S (RSL3)	TargetMol Chemicals Inc.	T3646; CAS: 1219810-16-8
L-glutathione reduced (GSH)	Sigma Aldrich	G6013; CAS: 70-18-8
NADPH/H^{+}	Roche	10107824001
Glutathione Reductase from baker's yeast (S. cerevisiae)	Sigma Aldrich	G3664; CAS: 9001-48-3
Phosphatidylcholine hydroperoxide (PCOOH)	gift from Junya Ito, Tohoku University, Sendai, Japan	N/A
Collagenase A	Roche	10103578001; CAS: 9001-12-1
Percoll® Density Gradient Media	Sigma Aldrich	17-0891-01
SPLASH® LIPIDOMIX®	Avanti	330707
Alexa Fluor™ 488 C5 Maleimide	Invitrogen	A10254
DiI Stain (1,1'-Dioctadecyl-3,3,3',3'-Tetramethylindocarbocyanine Perchlorate ('DiI'; DiIC18(3)))	Invitrogen	D282
1,2-Diheptanoyl-sn-glycero-3-phosphocholine (D7PC)	Avanti Polar Lipids (Alabaster, USA)	100124-676; CAS: 39036-04-9
1,2-Dimyristoyl-sn-glycero-3-phosphocholine (DMPC)	Avanti Polar Lipids (Alabaster, USA)	O-1135.0001BA; CAS: 18194-24-6
IGEPAL® CA-630	Sigma Aldrich	I8896; CAS: 9002-93-1
Tissue-Tek® mounting medium	Tissue-Tek® O.C.T. Compound, Sakura	4583
X-tremeGENE™ HP DNA Transfection Reagent	Roche	6366244001

(*Continued on next page*)

Please cite this article in press as: Lorenz et al., A fin-loop-like structure in GPX4 underlies neuroprotection from ferroptosis, Cell (2026), https://doi.org/10.1016/j.cell.2025.11.014

Continued

REAGENT or RESOURCE	SOURCE	IDENTIFIER
123count eBeads™ Counting Beads	Invitrogen	01-1234-42
MagStrep Typ3 Strep-Tactin-Beads	IBA Lifesciences	2-1613-002
BXT Buffer	IBA Lifesciences	2-1042-025
StemProEZPassage Disposable Stem Cell Passaging Tool	StemProEZPassage™	23181010
AccucoreTM C18 column (150 x 2.1 mm; 2.6 µm, 80 Å)	ThermoFisher Scientific	17126-032130
Critical commercial assays		
Roti-Histo Kit	Carl Roth	6638.1
LIVE/DEAD™ Fixable Blue Dead Cell Stain Kit	Invitrogen	L23105
ApopTag Fluorescein in Situ Apoptosis Detection Kit	Sigma-Aldrich	S7110
ApopTag Peroxidase In Situ Apoptosis Detection Kit	Sigma-Aldrich	S7100
Aqua-Poly/Mount	Polysciences	18606-20
VECTASTAIN® Elite® ABC-HRP Kit, Peroxidase (Standard)	Vector Laboratories	PK-6100
Simoa® NF-light Advantage Kit	Quanterix®	103186
Ella Simple Plex Human NF-L Cartridge	Bio-Techne GmbH	ST01B-PS-002448
StemRNA 3rd Gen Reprogramming Kit	Reprocell	00-0076
P3 Primary Cell 4D-Nucleofector® Kit	Lonza	V4XP-3024
RNeasy Mini Kit	QIAGEN	74104
Reverse Transcription System Kit	Promega	PR-A3500
PowerUp™ SYBR™ Green Master Mix	Applied Biosystems	A25742
Pierce™ BCA Protein Assay Kit	Thermo Fisher	23225
Clarity™ Western ECL Blotting Substrate	Bio-Rad	1705060
SuperSignal™ West Femto Maximum Sensitivity Substrate	Thermo Fisher	34094
Pierce™ 660nm Protein Assay Kit	Thermo Fisher Scientific	22662
Pierce™ Silver Stain for Mass Spectrometry	Thermo Fisher Scientific	24600
Proteome Purify 2 Mouse Serum Protein Immunodepletion Resin	Bio-techne R&D	MIDR002
PREOMICS INC iST sample preparation 96x	Preomics	NC1699272
Deposited data		
Crystal structure of human; GPX4-U46C	Scheerer et al.[32]	PDB: 2OBI
Crystal structure of human; GPX4-U46C-R152K	This paper	PDB: 9RF1
Crystal structure of human; GPX4-U46C-R152H	This paper	PDB: 8Q8J
Crystal structure of human; GPX4-U46C-I129S-L130S	This paper	PDB: 8Q8N
Backbone chemical shift assignments for human GPX4-U46C	This paper	BMRB: 52110
Backbone chemical shift assignments for human GPX4-U46C-R152H	This paper	BMRB: 52111
Amide backbone chemical shift assignments for human GPX4-U46C-I129S-L130S	This paper	BMRB: 52112
Amide backbone chemical shift assignments for human GPX4-U46C-R152K	This paper	BMRB: 52113
Bottom-up proteomics dataset	This paper	PRIDE: PXD071158

(*Continued on next page*)

Continued

REAGENT or RESOURCE	SOURCE	IDENTIFIER
Experimental models: Cell lines		
Human: RAG01 ($GPX4^{R152H/R152H}$)	CureGPX4.org (San Francisco, CA)	N/A
Human: RAG02 ($GPX4^{WT/R152H}$)	CureGPX4.org (San Francisco, CA)	N/A
Human: HT-1080 $GPX4^{KO}$	Doll et al.[46]	Doll et al.[46]
Mouse: Pfa1	Seiler et al.[13]	Seiler et al.[13]
Mouse: Pfa1 $GPX4^{KO}$ pLV GPX4 WT (OE)	This paper	N/A
Mouse: Pfa1 $GPX4^{KO}$ pLV GPX4 R152H	This paper	N/A
Human: HT-1080 $GPX4^{KO}$ pLV GPX4 WT (OE)	This paper	N/A
Human: HT-1080 $GPX4^{KO}$ pLV GPX4 R152H	This paper	N/A
iPSC: RAG01 rs763745871 R152H/R152H	This paper	N/A
iPSC: RAG02 WT/R152H	This paper	N/A
iPSC: RAG01 corrected WT/WT	This paper	N/A
Neuronal progenitor cells (NPC)	This paper	N/A
Human: HEK 293T	ATCC	ATCC CRL-3216
Experimental models: Organisms/strains		
Mouse: $Gpx4^{R152H/WT}$: C57BL6/J-$Gpx4^{R152H/WT}$	Cyagen, 2255 Martin Avenue, Suite E, Santa Clara, CA 95050-2709, US	N/A
Mouse: $Gpx4^{R152H/WT}$: C57BL6/J/129S2/SvPasCrl-$Gpx4^{R152H/WT}$	This paper	N/A
Mouse: $Rosa26CreER^{T2tg/tg}$: C57BL6/J-$Rosa26CreER^{T2tg/tg}$	Dr. Anton Berns, The Netherlands Cancer Institute, Amsterdam, Holland	Hameyer et al.[47]
Mouse: $Gpx4^{R152H/fl}Rosa26CreER^{T2+/tg}$: C57BL6/J-$Gpx4^{R152H/fl}Rosa26CreER^{T2+/tg}$	This paper	N/A
Mouse: $Camk2aCreER^{T2}$: C57BL6/J-$Camk2aCreER^{T2tg/tg}$	Dr. Günther Schütz, German Cancer Research Center, Heidelberg, Germany	Casanova et al.[48]
Mouse: $Gpx4^{fl/fl}$: C57BL6/J-$Gpx4^{tm2Marc}$	Seiler et al.[13]	Seiler et al.[13]
Mouse: $Gpx4^{fl/fl}Camk2aCreER^{T2+/tg}$: C57BL6/J- $Gpx4^{fl/fl}Camk2aCreER^{T2+/tg}$	This paper	N/A
Mouse: $Gpx4^{R152H/fl}Camk2aCreER^{T2+/tg}$: C57BL6/J- $Gpx4^{R1^{52}H/fl}Camk2aCreER^{T2+/tg}$	This paper	N/A
Mouse: $L7Cre^{tg/tg}$: C57BL6/J-$L7Cre^{tg/tg}$	The Jackson Laboratory	JAX: 004146
Mouse: $Gpx4^{fl/fl}L7Cre^{+/tg}$: C57BL6/J-$Gpx4^{fl/fl}L7Cre^{+/tg}$	This paper	N/A
Mouse: 129S2/SvPasCrl Strain Code: #287	Charles River	CR: 287
Oligonucleotides		
gRNA-A1: AGTTAACAGACTTTCGGTGC-TGG	This paper	N/A
gRNA-A2: GGTGACTACCTACGGTGAGT-AGG	This paper	N/A
gRNA-B1: AATTGGAGTTAACAGACTTT-CGG	This paper	N/A
gRNA-B2: CCACTCTACCTACTCACCGT-AGG	This paper	N/A
sgRNA: GAAGCACTACGGACCCATGG	This paper	N/A
RAG01_PAM: EZTCCTCATCGACAAGAACGG CTGCGTGGTGAAGCGCTACGGACCCATGGA AGAGCCCCTGGTAGGTCCTCTCTAGEEA	This paper	N/A
Primers for Genotyping, see Table Primers	This paper	N/A
Primers for qPCR, see Table Primers	This paper	N/A
R152H_for (human): GCTCACGTCCATGTGCTTCT	This paper	N/A
R152H_rev (human): CCACACACTTGTGGAGCTAG	This paper	N/A
Sequencing primer R152H (human): CCACAGTTTG GACACCGTCT	This paper	N/A
Gpx4_fwd: CTGGCAGGTACCACTTGTAAAC	This paper	N/A
Gpx4_rev: GCAGACCTTCATGAGTGCCG	This paper	N/A

(*Continued on next page*)

Continued

REAGENT or RESOURCE	SOURCE	IDENTIFIER
Sequencing primer R152H (mouse): GCAGACCTT CATGAGTGCCG	This paper	N/A
RAG0_for: gtgcttcttttccagtgcca	This paper	N/A
RAG0_rev: atctttctgcgtaggggctt	This paper	N/A
qPCR_Gpx4_fwd: GTGAGGCAAGACCGAAGTAAA	This paper	N/A
qPCR_Gpx4_rev: GAACTGGTTACACGGGAAGG	This paper	N/A
qPCR_GAPDH_fwd: GGTGTGAACCATGAGAAGTATGA	This paper	N/A
qPCR_GAPDH_rev: GAGTCCTTCCACGATACCAAAG	This paper	N/A
Recombinant DNA		
pLV-EF1a-IRES-Neo	A gift from Tobias Meyer	Addgene plasmid: #85139
pEcoEnv-IRES-puro	a gift from Prof. Timm Schroeder, ETH Zurich	N/A
pMDLg_pRRE	a gift from Prof. Timm Schroeder, ETH Zurich	N/A
pRSV_Rev	a gift from Prof. Timm Schroeder, ETH Zurich	N/A
psPAX2	a gift from Didier Trono	Addgene plasmid: #12260
pMD2.G	a gift from Didier Trono	Addgene plasmid: #12259
pET-M11	EMBL-GS	https://www.embl.org
pLV-EF1a-IRES-Neo-mScarlet-Gpx4	This paper	N/A
pLV-EF1a neo-FLAG-hGPX4-WT	This paper	N/A
pLV-EF1a neo-FLAG-GPX4-R152H	This paper	N/A
Software and algorithms		
ParaVision (ver. 6.0.1)	Bruker	https://www.bruker.com/
Small Animal Physiological Monitoring System	Small Animal Instruments Inc., New York, USA	https://i4sa.com/
SVRTK slice to volume reconstruction toolkit	Uus et al.[49]	https://github.com/SVRTK/SVRTK
3DSlicer (ver. 5.8.1)	Fedorov et al.[50]	https://www.slicer.org
ActiMot system	TSE Systems GmbH, Bad Homburg, Germany	https://www.tsesystems.com
MetaboAnalyst online platform v5.0	Pang et al.[51]	https://www.metaboanalyst.ca
XDS package	Kabsch[52]	Kabsch[52]
Aimless package	Evans and Murshudov[53]	Evans and Murshudov[53]
XSCALE	Kabsch[52]	Kabsch[52]
Phaser package	McCoy et al.[54]	McCoy et al.[54]
COOT	Emsley et al.[55]	Emsley et al.[55]
REFMAC5	Murshudov et al.[56]	Murshudov et al.[56]
Phenix	Afonine et al.[57]	Afonine et al.[57]
AZARA software package v. 2.8	Wayne Boucher and Department of Biochemistry, University of Cambridge, UK	https://cambridge2000.com/azara/
Cambridge CS software package	Department of Biochemistry, University of Cambridge, UK	Bostock et al.[58]
PYMOL	Schrödinger and DeLano	https://pymol.org/pymol.html
Topspin software	Bruker Biospin, Rheinstetten, Germany	https://www.bruker.com
CcpNmr Analysis 2.5	Vranken et al.[59]	https://ccpn.ac.uk/software/version-2/
Proteoscape environment	Bruker Daltonics, Bremen, Germany	https://www.bruker.com
Spectronaut 19 software	Biognosys	www.Biognosys.com
Perseus 2.0.11 software	MPI Martinsried: Tyanova et al.[60]	Tyanova et al.[60]

(*Continued on next page*)

Please cite this article in press as: Lorenz et al., A fin-loop-like structure in GPX4 underlies neuroprotection from ferroptosis, Cell (2026), https://doi.org/10.1016/j.cell.2025.11.014

Continued

REAGENT or RESOURCE	SOURCE	IDENTIFIER
Maxquant 31 version 1.5.5.2	MPI Planegg; Cox and Mann[61]	https://www.maxquant.org/; Cox and Mann[61]
MaxLFQ algorithum	Cox et al.[62]	Cox et al.[62]
FactoMineR package	Lê et al.[63]	Lê et al.[63]
ComplexHeatmap package (version 2.16.0)	Gu et al.[64]	Gu et al.[64]
BioMart (GRCm39)	Smedley et al.[65]	Smedley et al.[65]
GeneRanker	Precigen, Inc. (former copyright holder Genomatix, Germany)	https://precigen.com/
ElDorado 04-2021	Precigen, Inc. (former copyright holder Genomatix, Germany)	https://precigen.com/
Genomatix Literature Mining 01-2021	Precigen, Inc. (former copyright holder Genomatix, Germany)	https://precigen.com/
clusterProfiler (version 4.6.2)	Yu et al.[66]	Yu et al.[66]
Human MSigDB Collections web page	Liberzon et al.[67]	Liberzon et al.[67]
metacont function (package meta, version 6.1-2)	Balduzzi et al.[68]	Balduzzi et al.[68]
KEGG gmt file (version 2019)	Kanehisa et al.[69]	Kanhisa et al.[69]
WGCNA package	Langfelder and Horvath[70]	Langfelder and Horvath[70]
PanglaoDB	Franzén et al[71]	Franzén et al.[71]
Meta-analysis of AD proteomics data	N/A	https://github.com/hazhay/Meta-analysis_AD
clusterProfiler	Yu et al.[66]	Yu et al.[66]
Other		
9.4 T Biospec 94/20 USR	Bruker BioSpin GmbH, Germany	www.bruker.com
675 mT/m gradient system BG-12	Bruker BioSpin GmbH, Germany	www.bruker.com
Cryogenic transceiver quadrature RF surface probe	Bruker BioSpin GmbH, Germany	www.bruker.com
Minispec device LW65	Bruker BioSpin GmbH, Germany	www.bruker.com
Shimadzu ExionLC	Shimadzu Deutschland GmBH	www.shimadzu.de
Sciex Triple Quad™ 7500 LC-MS/MS	Sciex, MA, USA	www.sciex.com
TTP Labtech Mosquito LCP Crystallisation Robot	TTP (SPT) Labtech, Melbourn, UK	www.sptlabtech.com
SLS Beamline PXIII	Paul Scherrer Institut, Villigen, Switzerland	www.psi.ch
Avance III HD (AV600) NMR spectrometer, cryo-QCIP probe	Bruker BioSpin GmbH, Germany	www.bruker.com
Avance III (AV800) NMR spectrometer, cryo-TCI probe	Bruker BioSpin GmbH, Germany	www.bruker.com
Avance III HD (AV900) NMR spectrometer, cryo-TCI probe	Bruker BioSpin GmbH, Germany	www.bruker.com
Avance III HD (AV950) NMR spectrometer, cryo-TCI probe	Bruker BioSpin GmbH, Germany	www.bruker.com
Orbitrap Exploris 480 mass spectrometer	ThermoFisher Scientific	www.thermofisher.com
Evosep One LC-MS	Evosep Biosystems, Odense, Denmark	www.evosep.com
timsTOF HT	Bruker BioSpin GmbH, Germany	www.bruker.com
Thermo Scientific EASY-nLC 1000	ThermoFisher Scientific	www.thermofisher.com
Spectronaut Pulsar	Biognosys	Cat. No. Sw-3001, version 15.12.210819

EXPERIMENTAL MODEL AND METHOD DETAILS

Patients

Informed consent was obtained from all participants and their families. Human subjects research was approved by the University of California, San Diego Institutional Review Board and the Rady Children's Hospital Research Compliance.

Animals

All mice of both sexes were bred and housed in the Helmholtz Center Munich animal facility (CF-LAS) under SPF-IVC standard environmental conditions (22 ± 2 °C, 55 ± 5 % humidity, 12 h light/dark cycle) with free access to water and food in groups of 2-5 animals. Breeding conditions followed local animal welfare requirements. All animal experiments complied with the German Animal Welfare Law and have been approved by the institutional committee on animal experimentation and the government of Upper Bavaria (AZ 02-14-205, AZ 02-20-51, AZ 02-23-94). Offspring were weaned from the mothers around three weeks after birth and marked by ear punch for identification and subsequent DNA extraction for genotyping.

Generation of $Gpx4^{R152H}$ mice

$Gpx4^{R152H/WT}$ mice were generated by Cyagen (2255 Martin Avenue, Suite E, Santa Clara, CA 95050-2709, US) based on a CRISPR/Cas9 strategy. P.R152 of *Gpx4* is located on exon 6 of the murine chromosome 10. For the p.R152H KI model (CGC to CAT), a targeting vector with the specified nucleotides and homology arms was generated by PCR using a bacterial artificial chromosome as a template. The targeting vector was co-injected into fertilized mouse eggs with Cas9 and gRNA (gRNA-A1: AGTTAACAGACTTTCGGTGC-TGG; gRNA-A2: GGTGACTACCTACGGTGAGT-AGG; gRNA-B1: AATTGGAGTTAACAGACTTT-CGG; gRNA-B2: CCACTCTACCTACTCACCGT-AGG). Littermates were first genotyped, followed by sequencing analysis. To verify the genotype of $Gpx4^{R152H}$ mice, DNA was amplified by PCR using primers binding to exons 5 to 7 of *Gpx4* (fwd: CTGGCAGGTACCACTTGTAAAC; rev: GCAGACCTTCATGAGTGCCG) and the PCR product (438 bp) sequenced by Eurofins Genomics LLC. (rev: GCAGACCTTCATGAGTGCCG). For generating $Gpx4^{R152H}$ mice on a mixed background (C57BL/6J × 129S2/SvPasCrl), $\mathrm{Gpx4}^{R152H/WT}$ mice on C57BL6/J background were crossed with 129S2/SvPasCrl (#287, Charles River).

Generation of tamoxifen (TAM)-inducible $Gpx4^{R152H/fl}Rosa26CreER^{T2+/tg}$ mice

Since $Gpx4^{R152H/R152H}$ mice die during embryogenesis, TAM-inducible $ROSA26CreER^{T2}$ deleter strain kindly provided by A. Berns (The Netherlands Cancer Institute, Amsterdam, Holland)[47] was used and crossbred with $Gpx4^{R152H/fl}$ mice to generate conditional $Gpx4^{R152H/fl}Rosa26CreER^{T2+/tg}$*mice*. All cohorts contained an equal number of females/males (n > 3) of the same age between 10 and 15 weeks and were injected intraperitoneally (*i.p.*) with 2 mg (100 μL of 20 mg/mL, day 0 and 2) TAM (Sigma, #T5648) dissolved in miglyol.

Generation of TAM-inducible $Gpx4^{fl/fl}Camk2aCreER^{T2+/tg}$ and $Gpx4^{R152H/fl}Camk2aCreER^{T2+/tg}$ mice

For the specific deletion of *Gpx4* or the expression of $\mathrm{GPX4}^{\mathrm{R152H}}$ in glutamatergic neurons, $Gpx4^{fl/fl}$ mice ($Gpx4^{tm2Marc}$, previously described in Seiler et al.[13]) or $Gpx4^{R152H/fl}$ mice, respectively, were crossed with a TAM-inducible Cre line $Camk2aCreER^{T2}$ mice (Dr. Günther Schütz, German Cancer Research Center, Heidelberg, Germany).[48,72] Due to transient Cre recombinase expression in sperm cells, only Cre recombinase-positive females were mated with Cre-negative males. All cohorts contained an equal number of females/males (n > 3) of the same age between 10 and 15 weeks and were injected intraperitoneally (*i.p.*) with 2 mg TAM (100 μL of 20 mg/mL, on day 0, 2, and 4) dissolved in miglyol. The *in vivo* treatment study was performed using 30 mg/kg liproxstatin-1 (dissolved in PEG400/Solutol/PBS as vehicle) administered daily *i.p.* alongside TAM on days 0, 2, and 4 for the duration of 10 days.

Generation of $Gpx4^{fl/fl}L7Cre^{+/tg}$ mice

For the generation of mice with specific deletion of *Gpx4* in mostly Purkinje cells, $Gpx4^{fl/fl}$ mice ($Gpx4^{tm2Marc}$, previously described in Seiler et al.[13]) were first bred with $L7Cre^{tg/tg}$ (JAX stock #004146[73]). Subsequently, $Gpx4^{wt/fl}L7Cre^{+/tg}$ females were crossed with $Gpx4^{fl/fl}$ mice, resulting in $Gpx4^{fl/fl}L7Cre^{+/tg}$ mice. Mice were analyzed at the ages of 6 and 10 weeks.

Cell lines

The human fibroblast cell lines RAG01 ($GPX4^{R152H/R152H}$) and RAG02 ($GPX4^{WT/R152H}$) were kindly provided by CureGPX4.org (San Francisco, CA). Cells were cultured in Dulbecco's modified Eagle's medium (DMEM, Gibco, #21969035) supplemented with 15 % fetal bovine serum (FBS, Gibco, #2177353), 2 mM L-glutamine, 1 % penicillin/streptomycin, and 1 % nonessential amino acids. RAG01 required Trolox (ThermoScientific Acros, #10782831) or liproxstatin-1 (Lip-1, Selleckchem, #S7699) for normal growth. 50 μM Trolox or 1 μM of Lip-1 was added to the medium and only removed for testing various assays throughout the study.

The $GPX4^{KO}$ human fibrosarcoma HT-1080 cell line was described previously.[46] Cells were maintained in DMEM (glucose 4.5 g/L) supplemented with 10 % FBS, 2 mM L-glutamine and 1 % penicillin-streptomycin mix. 50 μM Trolox or 1 μM of Lip-1 was added to the medium and only removed for testing various assays throughout the study. Cells were cultured in a 37 °C incubator with a humidified atmosphere of 20 % O_2 and 5 % CO_2 (Binder).

The 4-hydroxy-TAM inducible murine embryonic fibroblasts cell line harboring two loxP-flanked (floxed) *Gpx4* alleles (Pfa1) was described previously.[13] Cells were maintained in DMEM supplemented with 10 % FBS, 2 mM L-glutamine, and 1 % penicillin-streptomycin mix. After induction with 1 μM 4-hydroxytamoxifen (4-hydroxy-TAM, Sigma-Aldrich, #SIALH7904), cells were maintained in the presence of 50 μM Trolox or 1 μM Lip-1, which was only removed for testing various assays throughout the study. Cells were cultured in a 37 °C incubator with a humidified atmosphere of 20 % O_2 and 5 % CO_2 (Binder).

Primary cell cultures

RAG01 and RAG02 iPSC lines generated from human primary fibroblasts were cultured on Matrigel-coated plates (Corning, #356234) in StemMACs iPS-Brew XF (Miltenyi Biotec, #130-104-368). RAG01 iPSCs were additionally supplemented with 0.5 μM Lip-1 (Selleckchem, #S7699). Cells were cultured in a 37 °C incubator with a humidified atmosphere of 20 % O_2 and 5 % CO_2 (Binder).

Please cite this article in press as: Lorenz et al., A fin-loop-like structure in GPX4 underlies neuroprotection from ferroptosis, Cell (2026), https://doi.org/10.1016/j.cell.2025.11.014

iPSC culture

RAG01 and RAG02 iPSC lines were cultured on Matrigel-coated plates (Corning, #356234) in StemMACs iPS-Brew XF (Miltenyi Biotec, #130-104-368). RAG01 iPSCs were additionally supplemented with 0.5 μM Lip-1 (Selleckchem, #S7699). Media was changed every 2 days and cells were passaged every 3-5 days as clumps with 0.5 M EDTA (0.5 M EDTA, 5 M NaCl, 1x PBS).

Forebrain organoids

RAG01 and RAG02 forebrain organoids were generated following a published protocol with minor modifications.[23]

METHOD DETAILS

Human participants analysis

A pediatric neurologist and geneticist clinically evaluated all affected individuals. Subjects underwent complete dysmorphology, neurological, and general examinations. Magnetic resonance or X-ray diagnostics were performed during routine clinical work-up, and some of these results were used in this study. Sanger Sequencing was performed to confirm the R152H allele. To verify the genotype of RAG01 ($GPX4^{R152H/R152H}$) and RAG02 ($GPX4^{WT/R152H}$), exon 6 of *GPX4* was amplified using PCR (fwd: GCTCACGTCCATGTGCTTCT; rev: CCACACACTTGTGGAGCTAG) and the PCR product (374 bp) sequenced by Eurofins Genomics LLC. (fwd: CCACAGTTTGGACACCGTCT).

MR Imaging

The MRI experiments were performed on a 9.4 T Biospec 94/20 USR (Bruker BioSpin GmbH & Co. KG, Germany) small animal system equipped with a 675 mT/m gradient system BG-12 (Bruker BioSpin GmbH & Co. KG, Germany) and operated with ParaVision (ver. 6.0.1). For signal acquisition, the vendor's cryogenic transceiver quadrature RF surface probe (Bruker BioSpin GmbH & Co. KG, Germany) was used.

Two-dimensional (2D) images covering the entire brain were acquired along the three orthogonal planes, axial, coronal, and sagittal, applying multi-slice fat-suppressed T2-weighted Rapid Acquisition with Refocused Echos (2D fs-RARE) sequences. The 2D fs-RARE parameters were as follows: TR = 2500 ms, TE = 33 ms, flip angle = 90° / 180°, rare factor = 6, averages = 2, bandwidth = 55.5 kHz, matrix size = 256 x 256, slice thickness of 0.4 mm, interslice distance = 0.1 mm, resolution = 78 x 78 μm^2, acquisition time = 3:30 min.

At the third time point, the vendor's mouse whole body volume coil was used together with the vendor's 2-channel quadrature surface coil for signal acquisition, as the cryogenic coil was not available at that time. The 2D fs-RARE parameters for this coil combination were similar to the cryogenic setting, except that the averages were increased to 4, resulting in an acquisition time of 7 min.

For *in vivo* studies, the mice were anesthetized under a mixture of 1–2 % isoflurane in 100 % oxygen. Anesthetized animals were placed in a prone position with their head firmly fixed using tooth and ear bars. A small animal physiological monitoring system (Small Animal Instruments Inc., New York, USA) was used to monitor animal physiology and depth of anesthesia. The respiration rate was measured by a pressure sensitive balloon, body temperature by rectal thermometer. Prior imaging body weight was measured of each individual animal.

Imaging experiments were performed at baseline, 4, 8, and 24 weeks after TAM injection (n = 3 males per group). After the last time point, mice were sacrificed and subjected to pathology.

Image Analysis

The SVRTK slice to volume reconstruction toolkit[74] was used to reconstruct for each mouse a 3D volumetric data with an isotropic resolution of 100 μm^3 derived from the acquired 2D sets at the three orthogonal planes. Based on these reconstructed isotropic data, volumes of the brain and the cerebrospinal fluid were obtained by manual segmentation using the 3DSlicer (ver. 5.8.1) software.[51]

Body composition

Body composition analysis of mice was performed at baseline, 1, 2, 4, 8, and 24 weeks after TAM induction using nuclear magnetic resonance (NMR). For this purpose, we employed a Minispec device (Bruker LW65, Ettlingen, Germany), which allows non-invasive determination of fat mass, lean tissue mass, and body fluid in conscious, unanesthetized mice. After weighing the mice, they were individually placed in a cylindrical chamber (inner diameter approx. 50 mm) and inserted into the device. Each measurement cycle lasted less than 2 min. The results are displayed as mean ± SEM/SD per body weight.

Tissue and embryo dissection

Vaginal mucous plug-positive female animals from heterozygous $Gpx4^{R152H/WT}$ breedings were sacrificed at embryonic (E) stages E7.5 and E9.5. Embryos isolated from the decidua were either used for whole-mount analysis or fixed in 4 % paraformaldehyde and embedded in paraffin for immunohistological analysis. Cohorts were grouped for analysis at different time points after knockout induction, with a comparable distribution of females and males. Animals were anesthetized for final blood collection by retrobulbar injection into plasma tubes. After centrifugation (1800×*g*, 15 min, room temperature), plasma samples were stored at -80 °C until further analysis. Thereafter, animals were perfused transcardially with 25 mL AntiOx buffer (100 μM DTPA, 100 μM BHT, 3.8 % trisodium citrate in PBS, pH 7.4). Freshly dissected tissue was frozen in liquid nitrogen and stored at -80 °C until use or post-fixed in 4 %

paraformaldehyde at 4 °C overnight, followed by overnight incubation in 30 % sucrose for cryo-embedding or 70 % ethanol for paraffin-embedded tissue blocks. Fixed tissue for cryo-sectioning was embedded in Tissue-Tek® mounting medium (Tissue-Tek® O.C.T. Compound, Sakura, #4583) on dry ice and stored at -80 °C.

Hematoxylin and eosin (HE) staining

Deparaffinization of 4 μm thick sections was performed by incubation in xylol and a hydration series of ethanol (100, 95, and 70%). After staining in Mayer's Hematoxylin (Carl Roth GmbH, #T865.1) for 70 s, sections were washed twice in water for 3 min and 10 min in running tap water. Sections were washed in water for 2 min and stained in 0.5 % eosin with a drop of glacial acetic acid for 20 s. Before being mounted in the Roti-Histo Kit (Carl Roth GmbH, #6638.1), sections were dehydrated through a graded series of ethanol (70, 96, and 100 %) and cleaned in xylol. Pictures were taken using a Nikon microscope (ECLIPSE Ni-E microscope, Nikon).

Periodic acid–Schiff (PAS) Reaction

Deparaffinization of 4 μm-thick sections was performed by incubation in xylol and a hydration series of ethanol (100, 95, and 70 %). After staining in Schiff's reagent (Sigma-Aldrich, #3952016) for 20 min, sections were washed for 3 min in running tap water and for 3 min in water. Counter-staining was done by incubating the sections for 3 min in Mayer's Hematoxylin (Carl Roth GmbH, #3952016), followed by incubation in water for 2 min and 7 min in running tap water. Before being mounted in the Roti-Histo Kit (Carl Roth GmbH, #6638.1), sections were dehydrated through a graded series of ethanol (70, 96, and 100 %) and finally cleaned in xylol. Pictures were taken by using a Nikon microscope (ECLIPSE Ni-E microscope, Nikon).

Terminal deoxynucleotidyl transferase dUTP nick end labelling (TUNEL) staining

ApopTag Fluorescein in Situ Apoptosis Detection Kit (Sigma-Aldrich, #S7110) was used for cryosections, and ApopTag Peroxidase in Situ Apoptosis Detection Kit (Sigma-Aldrich, #S7100) for paraffin-embedded tissue sections according to the manufacturer‘s instructions to detect TUNEL-positive cells. As pre-treatment, cryosections were immersed in preheated PBST and incubated at 85 °C for 20 min, followed by three washing steps with PBS. Immunofluorescence images were obtained by using a LSM880 confocal microscope (Zeiss) using the lasers 405 nm, 488 nm, and 595 nm, and brightfield images by a Nikon microscope (ECLIPSE Ni-E microscope, Nikon).

Nissl staining

Sagittal free-floating sections (40 μm) were washed with PBS overnight to remove cryoprotection solution (50 % PBS, 25 % glycerol, 25 % ethylene glycol). Nissl staining was performed using 0.5 % cresyl violet (Sigma-Aldrich, #C5042) for 1 min, followed by dehydration through a graded ethanol series (100, 95, and 70 %) and final cleaning in xylol. Slides were mounted using Roti-Histo Kit. Pictures were taken using an AxioScan microscope (Axioplan 2 microscope, Zeiss).

Transmission electron microscopy

Samples were fixed with 2.5 % glutaraldehyde in 0.1 M sodium cacodylate buffer, pH 7.4 (Electron Microscopy Sciences, USA) for 24 h at a minimum. Thereafter, glutaraldehyde was removed, and samples were washed three times with 0.1 M sodium cacodylate buffer, pH 7.4. Post fixation and prestaining was done for 45 to 60 min with 1 % osmium tetroxide (Electron Microscopy Sciences, USA), Samples were washed three times with ddH_2O and dehydrated with an ascending ethanol series (15 min with 30 %, 50 %, 70 %, and 90 % respectively and two times 10 min with 100 %). Subsequently, samples were embedded in Epon (Serva Electrophoresis GmbH). 60-70 nm thick ultrathin sections were cut at the Reichard-Jung Ultracut E microtome (Darmstadt, Germany) microtome. Ultrathin sections were collected on formvar-coated copper grids (Plano, Germany) and automatically stained with UranyLess EM Stain (Electron Microscopy Sciences) and 3 % lead citrate (Leica, Wetzlar, Germany) using the contrasting system Leica EM AC20 (Leica, Wetzlar, Germany). Imaging was carried out using the JEOL -1200 EXII transmission electron microscope (JEOL, Akishima, Tokyo) at 70 kV. Images were captured using a digital camera (KeenView II; Olympus, Germany) and processed with the iTEM software package (analysis Five; Olympus, Germany).

Immunohistochemistry

For brain

Sagittal free-floating sections (40 μm) of brains were washed with PBS overnight to remove cryoprotection solution (50 % PBS, 25 % glycerol, 25 % ethylene glycol). After blocking with 5 % goat serum in PBS/0.3 % Triton-X, sections were incubated with primary antibody at 4 °C overnight. As primary antibodies were used anti-GFAP (1:500, Invitrogen, #PA110004), anti-IBA1 (1:1000, Abcam, #ab178846), anti-HuC/HuC (1:400, Invitrogen, #A21271) and Anti-Calbindin (1:500, Sigma-Aldrich, #C9848-100UL). After three washing steps in PBS, sections were incubated for 1 h at room temperature with fluorescence-labelled secondary antibodies (Goat anti-chicken Alexa Fluor® 488, ThermoFisher Scientific, #A32931; Donkey anti-rabbit Alexa Fluor® 594, ThermoFisher Scientific, #A21207, Goat Anti-Mouse Alexa Fluor® 647, Abcam, #ab150115). Finally, sections were stained with 1 % 4'-6-diamidino-2-phenylinodole (DAPI) solution for 5 min and mounted with Aqua-Poly/Mount (Polysciences, #18606-20). Immunofluorescence images were obtained by using a LSM880 confocal microscope (Zeiss).

For kidney

Kidney 4 μm thick tissue sections were deparaffinized in xylol with the following hydration series of ethanol (100, 95, and 70 %). For antigen retrieval sections (for anti-KIM-1 and anti-GPX4 staining) were heated in a microwave oven in 10 mM citrate buffer pH 6.0 for 10 min. After washing in TBS/0.01 % tween-20 (TBS-T) for 5 min, the sections were blocked with 10 % goat serum (Cell Signalling, #5425) in TBS-T and incubated with primary antibody diluted in 5 % goat serum containing TBS-T at 4 °C overnight. As primary antibodies were used anti-GPX4 (1:100, Abcam, #ab125066), anti-KIM-1 (1:200, R&D Systems, #AF1817) and anti-HNE (0.5 μg/mL, JaICA, #HNEJ-2). The next day slides were washed in TBS-T, incubated for 20 min in 0.3 % H_2O_2 in methanol, washed again three times in TBS-T, and then incubated for 30 min with biotinylated goat anti-mouse-IgG (1:200 for 4-HNE, Vector Laboratories, #BA-9200), goat anti-rabbit-IgG (1:250, for GPX4, Vector Laboratories, #BA-1000), and donkey anti-goat-IgG (1:500 for KIM-1, Abcam, #208000). Staining was performed using the VECTASTAIN Elite ABC system and nickel-enhanced Vector DAB kit (Vector Laboratories, #PK-6100) according to the manufacturer‘s instructions. Finally, sections were dehydrated through a graded series of ethanol (70, 96, and 100 %) and finally cleaned in xylol before being mounted in Roti-Histo Kit.

For forebrain organoids

Organoids were washed with PBS and fixed overnight at 4 °C in 4 % PFA (Santa Cruz Biotechnology, #sc-281692). The following day, organoids were washed twice with PBS and cryoprotected in 30 % sucrose (Sigma Aldrich, #84097) in PBS overnight on a tube rotator at 4 °C, before being embedded in Neg-50 (Epredia, #6502B) and stored at -80 °C. Organoids were sectioned at 30 μM with a cryostat (Leica, CM3050 S). Sections were permeabilized using 0.3 % Triton X-100 (Fisher Scientific, #BP151-100) in PBS for 15 min on a shaker at room temperature, before being blocked in 0.15 % Triton X-100/5 % BSA (Sigma Aldrich, #A7906) in PBS for 1.5 h on a shaker at room temperature. Sections were then incubated overnight on a shaker at 4 °C in a 1:100 dilution of primary antibody against CTIP2 (Abcam, #ab18465) in 0.15 % Triton X-100/5 % BSA in PBS. The following day, sections were washed three times with 0.15 % Triton X-100 in PBS before being incubated on a shaker at room temperature in a 1:500 dilution of secondary antibody (Abcam, #ab150157) for 1.5 h. Sections were washed two times with 0.15 % Triton X-100 in PBS before being mounted onto slides and imaged using a Zeiss fluorescence microscope (LSM980).

Immunocytochemistry

IPSCs were grown on Matrigel matrix coated image dishes until they reached 70-100 % confluency and fixed directly with 4 % PFA for 10 min at room temperature. Differentiated cortical neurons (CN) were replated on poly-L-ornithine/laminin-coated plates (ibidi, #80841) and fixed with 10 % formalin for 15 min at room temperature. After three washing steps with PBS, cells were incubated with the respective primary antibody in PBS with 2 % FBS, 0.2 % Triton-X overnight at 4 °C (hiPSCs: Oct4a, Cell Signalling, #2840S; Sox2, Cell Signalling, #3579S; Lin28A, Cell Signalling, #3978S; Nanog, Cell Signaling, #4903S; CN: NeuN, Cell Signalling, #24307S; CTIP2 abcam, #ab18465; MAP2, Chemicon, #MAB3418; CUX1, Biomol, #HPA003277.100; TUJ, Cell Signalling, #5568S). On the next day, cells were washed three times with PBS before fluorescence-labelled secondary antibodies (Alexa Fluor 488 donkey anti-rat IgG (H+L), Invitrogen #A21208; Alexa Fluor 488 donkey anti-rabbit IgG (H+L) Invitrogen #21206; Alexa Flour 555 donkey anti-rabbit IgG (H+L), Thermo Fisher, #A31572; Alexa Fluor 555 donkey anti-mouse IgG (H+L), Thermo Fisher, #A31570) were applied for 1 h at room temperature. Finally, cells were stained with Hoechst 33342 solution (Invitrogen, #H3570) for 5 min and mounted with Aqua-Poly/Mount. Immunofluorescence images were obtained by using a EVOS FL Cell Imaging System (Thermo Fisher Scientific).

Behavioral tests

Behavior and gait analysis were assessed with the cohort of *Gpx4*$^{fl/fl}$ and *Gpx4*$^{fl/fl}$*Camk2aCreER*$^{T2+/tg}$ mice at 2 weeks after TAM treatment.

Open field

The Open Field (OF) was assessed 2 weeks after TAM injection of *Gpx4*$^{fl/fl}$*Camk2aCreER*$^{T2+/tg}$ mice and *Gpx4*$^{fl/fl}$ control mice and carried out as described previously.[75] The arena was made of transparent and infrared light-permeable acrylic with a smooth floor (internal measurements: 45.5 x 45.5 x 39.5 cm). Illumination levels for the measurement were set at approx. 150 lux in the corners and 200 lux in the middle of the test arena. Data were recorded and analyzed using the ActiMot system (TSE, Germany) over a 20-minute period.

Rotarod

The rotarod (Bioseb, Chaville, France), which is used to measure motor coordination and balance, is equipped with a computer-controlled, motor-driven rotating rod. The unit has a rotating spindle and five individual lanes for each mouse. The mice were placed perpendicular to the axis of rotation at an accelerating speed from 4 to 40 rpm for 300 sec, with 15 min between each trial. Mice were given three trials at an accelerating speed for one day. The mean latency to fall off the rotarod during the trials was recorded and used in subsequent analysis. In addition, the reason for the trial end (falling, jumping, or rotating passively) was recorded.

Y-maze

This test evaluates spatial working memory and was performed as previously described.[76,77] In brief, the Y-maze test apparatus consists of three identical arms (30 x 5 x 15 cm) placed at a 120° angle from each other, made of opaque light grey PVC. To assess spontaneous alternation, defined as consecutive entries into all three maze arms, mice are placed individually at the end of one arm and allowed to explore the Y-Maze for 5 min freely. A trained observer monitors arm entries. The ratio of actual to possible arm

Please cite this article in press as: Lorenz et al., A fin-loop-like structure in GPX4 underlies neuroprotection from ferroptosis, Cell (2026), https://doi.org/10.1016/j.cell.2025.11.014

alternations (total number of triplets) multiplied by 100 is calculated as % spontaneous alternations, and a ratio of alternate arm returns, and same arm returns is calculated likewise if more than 5 entries were made.

Balance beam

Mice were trained to traverse a one-meter-long round wooden beam. After training, animals were placed on the beam for three testing trials. The time needed to traverse the beam, the number of foot slips (both front and hind paw slips), and the number of falls from the beam were measured.

Hanging wire

Mice were placed with front paws on a bar (clothes hanger) 26 cm above the surface for a maximum duration of 1 min. The time to fall is recorded, providing insights into the motor function of mice.

Catalepsy

Forelimbs are placed on a wooden bar (0.7 cm in diameter) elevated 4.5 cm above the surface to test muscle rigidity and catalepsy as an externally imposed posture. The time to correct this position was measured (max time: 3 min).

Measurement of functional blood parameters

Animals were anesthetized for final blood withdrawal by retrobulbar bleeding into plasma or serum tubes. After centrifugation (1800 × *g*, 15 min, room temperature for plasma; 2500 x *g*, 10 min, 4 °C for serum), samples were stored at -80 °C until further analysis.

Serum samples were measured using the Beckman Coulter AU480 and test-specific Beckman Coulter (albumin, alkaline phosphatase, alanine aminotransferase, aspartate aminotransferase, total bilirubin, calcium, glucose, urea, high-density lipoprotein, creatinine, lactate dehydrogenase, phosphate, triglycerides) and WAKO (non-esterified fatty acids) reagents according to manufacturer's protocol.

Single molecule array (Simoa® / Ella-NfL)

Plasma neurofilament light (NfL) analysis was conducted on a single molecule array HD-1 Analyzer using single molecule array (Simoa) NF-light reagent kit (Quanterix®, #103186) or Ella Simple Plex Human NF-L Cartridge (Bio-Techne GmbH, #ST01B-PS-002448, SPCKB-MP-003168), according to the manufacturer's instructions. Mouse plasma samples were centrifuged (2000 x *g*, 5 min, room temperature) and diluted 1:6.67 with sample diluent before measurement.

Subcellular fractionation

Subcellular fractionation was performed according to the protocol Kabiri et al.[78] with an additional ultracentrifugation step at 100,000 x *g* for 1 h at 4 °C to collect the membrane-enriched fraction. In brief, HT-1080 *GPX4*^{KO} cells harboring either pLVneo-GPX4_WT or pLVneo-GPX4_R152H were collected at 80-95% density, pelleted by centrifugation for 5 min at 200 x *g* and resuspended at 6-7 x 10^6 cells/mL in a cold isolation buffer (300 mM sucrose, 5 mM TES, and 200 μM ethylene glycol-bis(2-aminoethylether)-N,N,N′,N′-tetra acetic acid (EGTA), containing protease and phosphatase inhibitor cocktail (cOmplete, Roche, #11873580001 and phosSTOP, Roche, #4906837001 pH 7.2), followed by homogenization by a pump-controlled cell rupture system with a clearance of 6 μm and 3 strokes at a speed rate of 1000 μL/min. The cell homogenate was centrifuged at 800 x *g* for 5 min at 4 °C, followed by two centrifugation steps at 10,000 x *g* (10 min, 4 °C) and 100,000 x *g* (1 h, 4 °C) to collect mitochondria- and membrane-enriched pellets, respectively. An equal amount of protein (10-20 μg) from each fraction was loaded onto 12 % or 15 % SDS-PAGE to evaluate quality of fractionation. Immunoblotting was performed using following primary antibodies: anti-VDAC (1:1000, Cell Signaling, #4866), anti-PMP70 (1:1000, ThermoFisher, #PA1-650), anti-VCP (1:5000, Abcam, #ab109240), anti-BiP/GRP78 (1:1000, BD Transduction Laboratories, #610978), anti-xCT/SLC7A11 (1:10, Helmholtz Core Facility), and anti-LAMP2 (1:1000, Cell Signaling, #49067). To calculate GPX4 abundance in mitochondria- or membrane-enriched fractions, the GPX4 intensity in the corresponding fractions was divided by the GPX4 intensity of each GPX4 variant from the homogenate fraction. Results are representative of three independent experiments.

Reprogramming of *GPX4*-mutated donor fibroblasts

Human primary fibroblasts RAG01 (*GPX4* with homozygous mutation rs763745871 R152H/R152H) and RAG02 (*GPX4* with heterozygous mutation WT/R152H) were subjected to daily transfections with a combination of synthetic, non-modified reprogramming factors (OCT4, SOX2, KLF4, cMYC, NANOG and LIN28) and immune evasion mRNAs (E3, K3, B18), in conjunction with reprogramming-enhancing mature, double-stranded microRNAs from the 302/367 cluster (Reprocell, #00-0076) in accordance with the manufacturer's protocol. The iPSC clones were manually selected based on their morphology from the original reprogramming plate. The established lines exhibited a standard compact shape, with clearly defined borders, when propagated in StemMACS iPS-Brew medium (Miltenyi Biotec, #130-104-368) and passaged using StemMACS Passaging Solution XF (Miltenyi Biotec, #130-104-688). The medium was supplemented with 5 μM Y-27632 dihydrochloride (Tocris, #1254) for a period of 24 h to facilitate the passaging and thawing steps. The medium was constantly supplemented with 500 nM Lip-1 (Selleckchem, #S7699).

Generation of an isogenic control line for the RAGO1 hiPSC line via CRISPR knock-in

The correction of the mutation rs763745871 (CGC –> CAC) for the *GPX4* gene, based on *Homo sapiens* hg38/GRCh38, was carried out in the RAG01 hiPSC line using the Cas9-sgRNA-donor DNA complex. The sgRNA (GAAGCACTACGGACCCATGG) and donor DNA introducing allele correction for rs763745871 and silent mutation of PAM sequence (EZTCCTCAT CGACAAGAACGGCTGCGTGGTGAAGCGCTAC GGACCCATGGAAGAGCCCCTGGTAGGTCCTCTCTAGEEA) were procured from ThermoFisher Scientific. RAG01 parental cells were nucleofected with a Cas9-sgRNA-donor DNA complex using the P3 Primary Cell 4D-Nucleofector® Kit (Lonza, #V4XP-3024) following the manufacturer's instructions. A one-week selection (in which Lip-1 was withdrawn) was conducted prior to the analysis of single clones, which had been obtained via limited dilution. The clones were analyzed for successful genomic correction by PCR (forward primer: gtgcttcttttccagtgcca and reverse primer: atctttctgcgtaggggctt) followed by Sanger sequencing. Multiple cell clones with homozygous or heterozygous correction of the target sequence were successfully detected via PCR and confirmed via Sanger sequencing. The corrected clones were cultured with the previously described culture conditions, with the omission of Lip-1.

Differentiation to cortical neurons (CN)

RAG01, RAG02 and CRISPR control clone hiPSCs were differentiated to CNs via neuronal progenitor cells (NPC) using dual SMAD signaling inhibition adapted from Shi et al.[79] Neuronal induction medium is a 1:1 mixture of N2 media, containing DMEM/F12 (ThermoFisher Scientific, #31330-038), 1x N2 (ThermoFisher Scientific, #17502-048), 5 μg/mL Insulin (Sigma-Aldrich, #I9278), 1x GlutaMAX (Thermo Fisher Scientific, #35050-038), 100 μM non-essential amino acid (NEAA, ThermoFisher Scientific, #11140-35), 100 μM 2-mercaptoethanol (ThermoFisher Scientific, #31350-010), 1x Anti-Anti (Thermo Fisher, #15240062) and B-27 media, containing Neurobasal (Life Technologies, #21103049), 1x B27 +/- antioxidants (AO) (+AO# 17504044, -AO#, ThermoFisher Scientific, #10889038), 1x GlutaMAX (1x Anti-Anti (ThermoFisher) supplemented with 100 nM LDN (Miltenyi, #130-103-925) and 10 μM SB431542 (Miltenyi, #130-106-275) replaced daily for around 13 days. For re-seeding the neuroepithelial sheet, cells were passaged using StemProEZPassage™ (Invitrogen, #23181-010) and transferred as clumps to Poly-L-ornithine/Laminin-coated plates. Neuronal induction medium supplemented with 10 ng/mL FGF2 (Miltenyi, #130-093-838) was changed daily until day 20. After re-seeding of the neuronal progenitor cells (NPCs) medium was changed to neural maintenance medium, consisting of a 1:1 mixture of N2 and B-27 medium, supplemented with 200 μM ascorbic acid (Sigma-Aldrich, #A8960-5G) and 20 ng/mL BDNF (Miltenyi Biotec, #130-093-811) for maturation until the end of differentiation (day > 42). All cells were cultured in the presence of 0.5 μM Lip-1 (Selleckchem, #S7699) until re-plating for the assay.

Forebrain organoids

Forebrain organoid generation

On day 1, RAG01 and RAG02 iPSCs were incubated at 37 °C in Accutase (Gibco, #A1110501) for 20-30 min until dissociation to single cells, before centrifugation and resuspension in iPS-Brew XF medium (Miltenyi Biotec, #130-104-368). Embryoid bodies were generated by seeding 9,000 cells per well in a 96-well V-bottom ultra-low attachment plate (Sbio, #MS-9096 VZ) in iPS-Brew XF containing 10 μM Y-27632 (Miltenyi Biotec, #130-103-922), while 0.5 μM Lip-1 was also included for all wells. In total, 150 μL was added to each well. Plates were then centrifuged at 800 x *g* for 5 min and incubated overnight in a 5 % CO_2 incubator at 37 °C. On day 0 (24 h after seeding), 120 μL of media was aspirated from each well and 120 μL of Essential 6 media (E6, ThermoFisher Scientific, #A1516401) containing 5 μM SB-431542 (Hycultec, #HY-10431), 2 μM XAV939 (Tocris, #3748) and 0.5 μM Lip-1 was added for all organoids. Subsequently, 100 μL media changes were performed daily until day 18. From day 4 onwards, XAV939 was no longer added to the media; organoids were cultured in E6 + 5 μM SB + 0.5 μM Lip-1. On day 18, organoids were transferred to 10 cm^2 dishes on an orbital shaker in basal organoid media: 50 % DMEM F-12 (ThermoFisher Scientific, #31330-038), 50 % Neurobasal media (ThermoFisher Scientific, #21103-049), 0.5 x N2 supplement (ThermoFisher Scientific, #17502-048), 0.025 % Insulin (Sigma-Aldrich, #I9278), 1x GlutaMAX (ThermoFisher Scientific, #35050-038), 0.5x MEM-NEAA (ThermoFisher Scientific, #11140-35), 100 U/mL Penicillin-Streptomycin (ThermoFisher Scientific, #15140-122), 55 μM 2-mercaptoethanol (ThermoFisher Scientific, #21985-023). Basal organoid media was additionally supplemented for the two different conditions: 1.) B27-AO+ Lip-1 condition: with 0.5x B27-AO (ThermoFisher Scientific, #12587010) and 0.5 μM Lip-1 and 2.) B27-AO- Lip-1condition: 0.5x B27-AO (ThermoFisher Scientific, #10889038).

Generation of lentiviral particles for transduction of mammalian cells

Synthetic gene fragments encoding for the N-terminal FLAG-tagged human GPX4 (FLAG-hGPX4) mutants of interest were designed and subsequently assembled and cloned by Twist Bioscience (Twist Bioscience HQ, 681 Gateway Blvd, South San Francisco, CA 94080) into a third-generation lentiviral transfer plasmid pLV-EF1a-IRES-Neo (Addgene plasmid #85139). HEK 293T cells were used to generate replication-incompetent lentiviral particles pseudotyped with the ecotropic envelope protein of the murine leukemia virus (MLV) or the pantropic envelope protein VSV-G. To produce ecotropic virus particles, cells were co-infected with pEcoEnv-IRES-puro, pMDLg_pRRE, pRSV_Rev (a kind gift from Prof. Timm Schroeder, ETH Zurich), pLV-EF1a-IRES-Neo transfer plasmid, and X-tremeGENE™ HP DNA Transfection Reagent (Roche, #6366244001) at a 1:3 ratio according to the manufacturer's protocol. To produce pantropic particles, cells were co-infected with psPAX2 (Addgene plasmid #12260), pMD2.G (Addgene plasmid #12259), and pLV-EF1a-IRES-Neo transfer plasmid, and X-tremeGENE™ HP DNA Transfection Reagent at a 1:3 ratio according to the manufacturer‘s protocol. After 72 h, cell culture supernatants containing viral particles were harvested, sterile filtered using a 45 μm low protein binding syringe filter and used to transfect cells with the FLAG-hGPX4 mutant of interest.

Stable expression of N-terminally FLAG-tagged human GPX4 mutants

GPX4^{KO} HT-1080 cells were infected with VSV-G pseudotyped lentiviral particles and Pfa1 cells with ecotropic lentiviral particles supplemented with 8 μg/mL protamine sulfate. After 48 h, the viral particle containing supernatant was removed, and geneticin selection was performed to validate stable transfection at a final concentration of 750 μg/mL. Thereafter, the deletion of endogenous *Gpx4* in Pfa1 cells was achieved by adding 1 μM of 4-hydroxy-TAM. Immunoblotting confirmed the deletion of endogenous *GPX4* and stable expression of FLAG-hGPX4 mutants.

Cell viability assay

Cells were seeded on 96-well plates (2,000 cells per well), and viability was assessed on the following day using AquaBluer (MultiTarget Pharmaceuticals, LLC, #6015) according to the manufacturer’s instructions. For differentiated cortical neurons (CN), 40.000 cells per well were seeded on a poly-L-ornithine/Laminin-coated 96-well plate in maturation medium (+/- Lip-1), containing 10 μM Y-27632 (Miltenyi Biotec, #130-103-922). Cells were fed daily, and readout was performed 72 h after re-plating. Fluorescence measurement at 562 nm was done according to the manufacturer’s instructions using a SpectraMax plate reader (Molecular Device GmbH).

Live-cell imaging

1 x 10^5 RAG01 and RAG02 cells were seeded on a μ-Dish (i-bidi, #3952016) and attached to the plate overnight. Cells were washed twice with PBS and cultured in Trolox-free media for imaging. For differentiated cortical neurons (CN), 3 x 10^5 cells were seeded on a poly-L-ornithine/Laminin-coated using maturation medium (without Lip-1) containing 10 μM Y-27632 for 24 h. After daily feeding of the cells, live cell imaging starts after an additional 24 h incubation with Lip-1 withdrawal. During imaging in 3D Cell Explorer, cells were maintained at 37 °C with a humidified atmosphere of 5 % CO_2. Video analysis was performed using Eve software v1.8.2 (Nanolive) and ImageJ.

Fluorescence microscopy

Cells expressing GPX4-mScarlet were seeded on 25 mm glass coverslips 24 h before the imaging experiment. The cells were washed once in PBS and fixed in 4 % PFA for 15 min. The cells were imaged using a Nikon Ti2 microscope with a NikonApo TIRF 100x Oil DIC N2 NA 1.49 objective. The samples were excited using a 561 nm laser (Coherent), and the emitted light was detected on a pco.edge 4.2 sCMOS camera (Excellitas). The cells were observed using WF and TIRF illumination. Super-resolution microscopy was performed on an LSM980 Airyscan2 confocal microscope (Zeiss) with a 63x Plan-Apochromat NA 1,4 oil objective. Images were analyzed using ImageJ/FiJi.

Quantitative real-time PCR

Total RNA isolation and cDNA synthesis were performed according to the manufacturer’s instructions using the RNeasy Mini Kit (QIAGEN, #74104) and the Reverse Transcription System Kit (Promega, #PR-A3500). mRNA expression levels were determined by quantitative real-time PCR (qTOWER, Analytik Jena) using PowerUp™ SYBR™ Green Master Mix (Applied Biosystems, #A25742) according to the manufacturer’s instructions. The following primers were used: *GPX4* (fwd: 5‘-GTGAGGCAAGACCGAAG TAAA-3‘; rev: 5‘-GAACTGGTTACACGGGAAGG -3‘); and *GAPDH* (fwd: 5‘-GGTGTGAACCATGAGAAGTATGA -3‘; rev: 5‘-GAG TCCTTCCACGATACCAAAG-3‘) as housekeeping control. Data analysis and quantification was done using the qPCRsoft software (Analytik Jena).

Determination of lipid peroxidation

1 × 10^5 cells were seeded on a 6-well plate and were allowed to attach overnight. Cells were incubated for 20 min with 1 μM C11-BODIPY 581/591 (Invitrogen, #D3861). Afterwards, cells were trypsinized, washed twice, and resuspended in Hank‘s Balanced salt solution. Lipid peroxidation levels were determined by measuring the C11-BODIPY 581/591 fluorescence signal change in 10,000 cells using a CytoFLEX S flow cytometer (Beckman Coulter). Data analysis was conducted using FlowJo v.10 analysis software (FlowJo LLC).

Immunoblotting

Cells or freshly dissected tissue were lysed in LCW lysis buffer (0.5 % Triton X-100, 0.5 % sodium deoxycholate salt, 150 mM NaCl, 20 mM Tris/HCl, 10 mM EDTA, 30 mM sodium pyrophosphate) containing protease and phosphatase inhibitor cocktail (cOmplete, Roche, #11873580001 and phosSTOP, Roche, #4906837001) using cell scraper for cells collection or a Eurostar RW16 stirrer for tissue homogenization. Lysates were centrifuged at 18,400 x *g*, 4 °C, 30 min for debris removal. The protein concentration in the supernatant was measured by quantification using the Pierce™ BCA Protein Assay Kit (Thermo Fisher, #23225). Equal amounts of protein (20 μg) were incubated for 5 min at 95 °C, separated on precast 12 % Mini-PROTEAN® TGX Stain-Free™ Protein Gels and transferred to PVDF membrane (both BioRad, semi-dry-transfer protocol: Standard SD, 30 min, 25 V, Bio-Rad). After blocking

Please cite this article in press as: Lorenz et al., A fin-loop-like structure in GPX4 underlies neuroprotection from ferroptosis, Cell (2026), https://doi.org/10.1016/j.cell.2025.11.014

in 5 % skim milk in TBST (25 mM Tris, 125 mM NaCl, 0.1 % Tween-20, pH 7.6), the membranes were incubated with the primary antibodies overnight at 4 °C. The following antibodies were used: anti-GPX4 (1:1000, #ab125066, Abcam), anti-GFAP (1:10000, Abcam, #ab7260), anti-IBA1 (1:500, Genetex, #GTX100042), anti-Calbindin (1:1000, Sigma-Aldrich, #C9848-100UL) anti-NeuN (1:500, Sigma-Aldrich), anti-NfL (1:1000, Cell Signaling, #Cat#2837S) and anti-VCP (1:1000, Abcam, #ab11433). The following day, membranes were washed and incubated with HRP-conjugated secondary antibodies (anti-rabbit, Santa Cruz, #SC-2030; anti-mouse, Santa Cruz, #SC-2031) for 1h at RT. Immunoconjugates were developed using Clarity™ Western ECL Blotting Substrate (Bio-Rad, #1705060) or ThermoScientific™ Super Signal West Femto (ThermoFisher, #34094) for antibodies with faint signal, and finally visualized by ChemiDocTM Imaging system (Bio-Rad).

GPX4 stability analysis

1×10^5 cells were seeded on a 6-well plate and allowed to attach overnight. The next day, cells were treated with 100 μg/mL cycloheximide and 4 μM RSL3 for 0, 2, 4, or 6 h. Harvesting was performed by scraping cells from the cell culture dish directly in lysis buffer (0.5 % Triton X-100, 0.5 % sodium deoxycholate salt, 150 mM NaCl, 20 mM Tris/HCl, 10 mM EDTA, 30 mM sodium pyrophosphate, 1 % protease and 1 % phosphatase inhibitor cocktail). GPX4 protein levels were determined by immunoblotting and analyzed with Image Lab 6.0 software (Bio-Rad).

Determination of GPX4 activity using affinity-purified enzyme

The activity of GPX4 and mutants was measured as previously described[29] with minor changes. Pfa1 cells stably expressing p442-FSH-tagged hGPX4^{WT}, GPX4^{U46C}, GPX4^{R152H}, GPX4^{R152K}, and GPX4$^{I129S;L130S}$ were expanded on 15 cm plates until they reached 80 % confluence. Cells were harvested by trypsinization followed by washing with PBS. Cell pellets were resuspended in 500 μL of the LCW lysis buffer containing protease inhibitor cocktail. Lysates were incubated on ice for 40 min and then centrifuged at 20,000 × *g* at 4 °C for 30 min. Meanwhile, MagStrep Type3 Strep-Tactin Beads (IBA Lifesciences, #2-1613-002) were washed three times with washing buffer (100 mM Tris-HCl, 150 mM NaCl, and 1 mM EDTA) and resuspended in the cell lysate according to the manufacturer's protocol. Beads were incubated with the lysates on a rotator for 1 hour at 4 °C and washed three times with the washing buffer. Strep-tagged proteins were natively eluted by incubating the beads for 15 min at room temperature in BXT Buffer (IBA Lifesciences, #2-1042-025). Protein concentration was estimated by comparing the band intensities of the samples to a standard curve generated from serial dilutions of bovine serum albumin (BSA), run on the same 12 % SDS-PAGE gel and visualized using silver staining (Pierce Silver Stain for Mass Spectrometry, ThermoFisher Scientific, #24600) following the manufacturer's instructions. Protein samples were then stored at -80 °C.

Affinity-purified hGPX4^{WT}, GPX4^{U46C}, GPX4^{R152H}, GPX4^{R152K}, and GPX4$^{I129S;L130S}$ (50 ng and 100 ng of the protein per reaction mix) were mixed with 10 μM PCOOH in the activity buffer (100 mM Tris base pH 8.0, 1.5 mM Sodium azide, 2 mM EDTA, 0.1 % Triton X-100, 1.5 U/mL Glutathione reductase, 1.5 mM GSH) for up to 30 min at 37 °C. To stop the reaction 5 μL of the mixture was sampled by mixing with 495 μL of LC-MS grade methanol.

These methanol samples were centrifuged, and the supernatant was subjected to an LC-MS/MS system consisting of a 7500 QTRAP tandem mass spectrometer (SCIEX) equipped with an Exion LC system (SCIEX). Chromatographic separation was performed using an Accucore C18 (2.1 x 150 mm; 2.6 μm particle size; ThermoScientific) at 50 C. The column was eluted with a mobile phase consisting of solvent A (acetonitrile/water 50:50 (v/v), 5 mM ammonium formate) and solvent B (2-propanol/acetonitrile/water 85:10:5 (v/v), 5 mM ammonium formate). The mobile phase gradient profile was as follows: 0–5 min, 55 % B to 80 % B linear; 5–5.1 min, 80 % B to 95 % B linear; 5.1-7 min 95 % B, 7-7.1 min 95 % B to 55 % B, 7.1-9.6 min 55 % B. The flow rate was 0.3 mL/min. The general LC-MS/MS conditions were as follows: entrance potential, 10.0 V; source temperature, 500 °C; spray voltage, 3000 V; source, ESI; and ion polarity, positive. PCOOH and PCOH (1-palmitoyl-2-13(S)-hydroperoxyoctadecadienoyl-*sn*-glycero-3-phosphocholine and 1-palmitoyl-2-13(S)-hydroxyoctadecadienoyl-*sn*-glycero-3-phosphocholine) was detected by multiple reaction monitoring (MRM) for the transition of precursor ions to products: (m/z 812.5 > 541.5, 796.5 > 613.5).

Determination of GPX4 activity in crude cell lysates

The activity of GPX4 was measured as previously described.[21] Cells were grown on 15 cm plates until 80 % confluence was achieved and stored at -80 °C after being harvested by trypsinization and washing twice with PBS. Frozen cell pellets were resuspended in 100 μL extraction buffer (100 mM KH_2PO_4/K_2HPO_4 (pH 7.4), 150 mM KCl, 1 mM EDTA, 0.05 % CHAPS, 2 mM β-mercaptoethanol, 1 % protease inhibitor cocktail (cOmplete, Roche)) by 50 pestle strokes using a Dounce tissue grinder, while frozen kidney tissue samples were ground to a fine powder in the presence of liquid nitrogen before being resuspended in 200 μL of extraction buffer. Both tissue and cell pellet samples were incubated on ice for 15 min before being centrifuged at 18,400 x *g* at 4 °C for 2 min. The supernatant was transferred to a fresh tube. For activity measurement, 50 μL of cell supernatant and 10 μL of tissue supernatant were added to a reaction buffer (100 mM KH_2PO_4/K_2HPO_4 (pH 7.8), 5 mM EDTA, 0.1 % Triton X-100 (peroxide-free)), 0.2 mM NADPH/H$^+$, 5 mM GSH, 0.6 U/mL glutathione reductase (GR) and 20-30 μM phosphatidylcholine hydroperoxide (PCOOH), and the spectrometric decrease of NADPH/H$^+$ by GR was measured at 340 nm. The protein concentration of each sample was determined using the Pierce 660 nm Protein Assay Kit (ThermoFisher Scientific) according to the manufacturer's protocol for normalization. Measurements were performed in a SpectraMax microplate reader (Molecular Device GmbH).

Please cite this article in press as: Lorenz et al., A fin-loop-like structure in GPX4 underlies neuroprotection from ferroptosis, Cell (2026), https://doi.org/10.1016/j.cell.2025.11.014

Isolation of CNS-Infiltrating immune cells and flow cytometry

Mice were perfused intracardially with ice-cold PBS immediately after being sacrificed by CO_2 to remove blood from the intracranial vessels. The brain was isolated with sterile instruments, minced with a scalpel and incubated with agitation in RPMI 1640 medium (PAA) containing 1 mg/mL collagenase A (Roche, #10103578001) and 0.1 mg/mL DNase I recombinant, RNase-free (Roche, #03724778103) for 45 min at 37 °C. Tissue was triturated through a 100-μm cell strainer and washed with PBS, with following centrifugation at 300 x *g* for 10 min at 4 °C. The homogenate was resuspended in 30 % isotonic Percoll (GE Healthcare, #17-0891-01) and carefully underlaid with 78 % isotonic Percoll. After gradient centrifugation (1500 x *g* for 30 min at 4 °C), CNS-infiltrating immune cells were recovered from the gradient interphase and washed in ice-cold PBS. Single-cell suspension was divided into two tubes for an immune-cell and microglia panel, and staining was performed in brilliant stain buffer (BD Biosciences, #563794) for 30 min at 4 °C. Fixable Dead Cell stain V500 (ThermoFisher, #L23105) was used for live/dead discrimination. Total cell numbers of infiltrating immune cells were measured from total brain hemispheres with 123 count eBeads (ThermoFisher, #01-1234-42). The expression levels of microglial activation markers were quantified in single live cells gated as $CD45^{low}$ and $CD11b^{+}$ populations. Data was acquired on an LSR II FACS analyzer (BD Biosciences). Data analysis was performed using the FlowJo v.10 software (FlowJo LLC).

(Oxy)lipidomics analysis

Lipids from mouse kidneys were extracted using the methyl-tert-butyl ether (MTBE) method.[80] Briefly, perfused mouse kidneys (approximately 70 mg wet tissue weight) were homogenized in ice-cold methanol (1 mL), containing 0.1 % (w/v) BHT and 1 μL of SPLASH® LIPIDOMIX® (Avanti, #330707). Samples were processed at 4 °C, using a Precellys® 24 homogenizer (5500 rpm, 3 cycles for 20 s with 30 s pause between cycles).

After ice-cold methanol (0.5 mL) and MTBE (5 mL) were added, samples were vortexed and incubated for 1 h at 4 °C (Orbital shaker, 32 rpm). The addition of water induced phase separation (1.25 mL). Next samples were vortexed, incubated for 10 min at 4 °C (Orbital shaker, 32 rpm), and centrifuged (10 min, 4 °C, 1500 x *g*). The upper layer was collected prior to sample re-extraction. The upper layer was dried in a vacuum evaporator (Labconco™), dissolved in 300 μL of isopropanol and stored in -80 °C before analysis by LC/MS/MS. All solvents were spiked with 0.01 % (w/v) BHT and cooled on ice prior lipid extraction. Reversed-phase liquid chromatography (RPLC) was carried out on a Shimadzu ExionLC equipped with an AccucoreTM C18 column (150 x 2.1 mm; 2.6 μm, 80 Å, ThermoFisher Scientific). Oxidized lipids were separated by gradient elution with solvent A (acetonitrile/water, 1:1, v/v) and B (isopropanol/acetonitrile/water, 85:10:5, v/v) both containing 5 mM NH_4HCO_2 and 0.1 % (v/v) formic acid. Separation was performed at 50 °C with a flow rate of 0.3 mL/min using the following gradient: 0-20 min – 10 to 86 % B (curve 4), 20-22 min – 86 to 95 % B, 22-26 min – 95 % isocratic, 26-26.1 min – 95 to 10 % B followed by 5 min re-equilibration at 10 % B.[27] Lipid extracts were analyzed using a Sciex Triple Quad™ 7500 LC-MS/MS system equipped with an electrospray (ESI) source and operated in negative ion mode. Products were analyzed in MRM mode monitoring transitions from the precursor ion to fragment ion, as described in Table S1 sheet 1, with the following parameters: TEM 500 °C, GS1 40, GS2 70, CUR 45, CAD 9, IS − 3000 V. The area under the curve for the precursor mass to fragment mass was integrated and normalized by appropriate lipid species from SPLASH® LIPIDOMIX® Mass Spec Standard (Avanti), and the sample weights. Normalized peak areas were further log-transformed and auto-scaled in MetaboAnalyst online platform v5.0 (https://www.metaboanalyst.ca).[81] Zero values were replaced by 0.2×, the minimum values detected for a given oxidized lipid within the samples. Oxidized lipid species showing a significant difference (ANOVA, adjusted *p* value [false discovery rate (FDR)] cutoff: 0.05) between samples were used for the heat maps. The heat maps were created in R package. The color scheme corresponds to auto-scaled log fold change relative to the mean log value within the samples.

Expression of $GPX4^{U46C}$ and mutants

$Gpx4^{U46C}$ (UNIPROT – P36969-2) and the mutants' cDNA (optimized for *E. coli* expression) were cloned into a pET-M11 vector, containing a 6-Histidine N-terminal cleavable tag and transformed into *E. coli* BL21 cells. Cells were grown in TB media or minimal media supplemented with ^{15}N ammonium chloride and ^{13}C glucose for producing isotope-labelled protein samples for NMR measurements. After reaching the target OD, cells were maintained at 20 °C overnight and supplied with 0.5 mM IPTG to boost the protein expression. Harvested cells were resuspended in PBS buffer, lysed by sonication, and centrifuged. The soluble fraction was applied to a nickel resin and washed with PBS before eluting the protein in PBS supplemented with 350 mM imidazole. The tag was cleaved by adding TEV protease, and the solution was dialyzed overnight back into PBS buffer. The solution was then applied to a nickel column, and the flow-through was collected and concentrated before a final size exclusion chromatography purification step. A S75-high load column was pre-equilibrated with PBS supplemented with 1 mM DTT, for proteins that were used for NMR measurements or 10 mM HEPES, 100 mM NaCl and 1 mM ß-mercaptoethanol, for proteins that were used for crystallization. A single peak of monomeric GPX4 was obtained, and the identity of the protein was confirmed by SDS-PAGE gel. Proteins were concentrated to 20 mg/mL, flash-frozen in liquid nitrogen and kept at -80 °C until further usage.

Structural analysis

Crystallization of GPX4

Purified protein was concentrated to 23-47 mg/ml and screened in sitting-drop vapor diffusion format using commercially available crystallization kits. Samples were prepared by mixing protein with buffer in a 1:1 ratio, using a Mosquito robot (TTP Labtech). $GPX4^{U46C;R152H}$ was crystallized at room temperature in a buffer containing 20 % w/v PEG monomethylether 5000 and 200 mM

Please cite this article in press as: Lorenz et al., A fin-loop-like structure in GPX4 underlies neuroprotection from ferroptosis, Cell (2026), https://doi.org/10.1016/j.cell.2025.11.014

lithium sulphate. GPX4$^{U46C;I129S;L130S}$ was crystallized at room temperature in 6% v/v Tacsimate pH 6.0. GPX4$^{U46C;R152K}$ was crystallized at room temperature in a buffer containing 0.2 M Ammonium acetate, 0.1 M BIS-Tris pH 5.5 and 25 % w/v PEG 3350. Crystals were flash-frozen with 25 % ethylene glycol as the cryoprotectant in the mother liquor. Data was collected at cryogenic temperatures at the PXIII beamline at the Swiss Light Source (Paul Scherrer Institut, Villigen, Switzerland) and ESRF Synchrotron, (Grenoble, France) using 1.000 Å wavelength at 100 K.[82] The XDS package was used to index and integrate the data.[52] Data was scaled and merged using the Aimless package and XSCALE.[52,53,83] Phasing was achieved using molecular replacement with the Phaser[54] package with GPX4^{U46C} (PDB: 2OBI) as the search model. The crystals show significant anisotropy of diffraction limiting the completeness of the data. Despite this, the yielded electron density was perfectly interpretable. COOT was used to manually rebuild the models[55] and cycles of alternating manual and automated refinement using COOT and the REFMAC5/Phenix programs[56,57] were carried out. Five percent of the reflections were used to generate a free-R set for cross-validation analysis, and R_{free} was used to monitor the progress of the refinement. Water molecules were added using the COOT program and manual inspection. The Ramachandran statistics for GPX4$^{U46C;R152H}$ and GPX4$^{U46C;I129S;L130S}$ were 97.55 % (160 residues in favored regions (98.16 %), 3 residues in allowed regions (1.84 %) and 0 outliers) and 97.55 % (134 residues in favored regions (93.7 %), 9 residues in allowed regions (6.3 %) and 0 outliers) respectively, for GPX4$^{U46C;R152K}$ were 99.69 % (321 residues in favored regions (97.87 %), 6 residues in allowed regions (1.82 %) and 2 outliers (0.61 %). Datasets of GPX4$^{U46C;R152H}$ indicated different modes of distortion of the fin-loop but no WT, extended conformation was observed. For analysis, we have chosen a crystal form that is not disturbed by crystal contacts in the fin-loop and H155 region. For GPX4$^{U46C;R152K}$ crystal structure, there were two molecules in the asymmetric unit with different loop conformations. Final models were deposited in the Protein Data Bank (PDB) under the accession codes 8Q8J, 8Q8N, and 9RF1. Refinement statistics are shown in Table S1, sheet 2.

Structural analysis (NMR spectroscopy)

NMR experiments were recorded at 298 K on Bruker Avance III spectrometers operating at 600, 800, 900, and 950 MHz (^{1}H frequency) equipped with cryogenic TCI or QCI probes. NMR samples were prepared in PBS buffer pH 6.5 with 1-5 mM DTT and 10 % D_2O for the lock signal. Backbone assignments for GPX4 WT and GPX4^{R152H} used standard 3D triple resonance experiments, including HNCACB/CBCACONH, HNCA/HNCOCA, HNCO/HNCACO, (H)CC(CO)NH-TOCSY and ^{15}N-NOESY experiments.[84] NMR spectra were processed using the AZARA software package (v. 2.8, © 1993-2023; Wayne Boucher and Department of Biochemistry, University of Cambridge, UK). Triple resonance spectra were acquired using non-uniform sampling and reconstructed using the Cambridge CS software package.[58] Sample schedules were generated using the default scheduler in Topspin software (Bruker Biospin, Rheinstetten, Germany). All spectra were analyzed using CcpNmr Analysis 2.5.[59] Chemical shift perturbation (CSP) analysis used the formula:

$$\Delta\delta = \sqrt{\left(\Delta\delta_{HN}\right)^2+\left(0.15\times\Delta\delta_{15_N}\right)^2}$$

{^{1}H}-^{15}N heteronuclear NOE (hetNOE) experiments used a saturation period of 3 s with interleaved reference and saturation planes,[85] with hetNOE values calculated from the ratios of intensities between the saturation and reference planes. The standard deviation of the noise was used to calculate the errors. NMR assignments were deposited in the Biological Magnetic Resonance Data Bank (BMRB) with accession codes: GPX4^{U46C} 52110; GPX4$^{U46C\text{-}R152H}$ 52111; GPX4$^{U46C\text{-}I129S;L130S}$ 52112; GPX4$^{U46C\text{-}R152K}$ 52113.

Binding of GPX4 to giant unilamellar vesicles (GUV)

500 µL of GPX4^{WT}, GPX4$^{I129S;L130S}$ or GPX4^{R152H} at 1 mg/mL in PBS were incubated with Atto 488 maleimide (Invitrogen) at 1:1 molar ratio for 2 h at RT under constant shaking. Unbound dye was removed by filtration (10 kDa cut-off). The degree of labelling was calculated for each protein in independent experiments and ranged from 25 to 30 %. GUVs were prepared by the electroformation procedure. 3 µL of corresponding lipid mixture (2 mg/mL) containing 0.1 mol % DiI (Invitrogen) in chloroform were deposited on the platinum wires of the electroformation chamber. After solvent evaporation, the wires were immersed in 300 µL of sucrose (300 mM) and electroformation proceeded for 2 h (10 Hz, 1.4 V) at room temperature followed by 45 min at 2 Hz, 1.4 V to ensure proper detachment of GUVs from the wires. 100 µL of the corresponding GUVs suspension containing DiI (0.1 mol %) were added to a LabTec chamber (Nalge Nunc International, EUA) containing 200 µL of the labelling protein in PBS to reach a final concentration of 5 µM and incubated for 1 h at room temperature. LabTec chambers were previously incubated with BSA (10 mg/mL) for 30 min to prevent nonspecific binding of proteins to the chamber. GUVs were observed at 23 ± 2 °C on a Leica confocal fluorescence microscope using a 1.2 C-Apochromat 40X water immersion objective. Excitation light came from an Ar-ion laser (488 nm) and He-Ne laser (633 nm). Protein binding to vesicles was estimated at the surface of the vesicles using the Radial Profile Angle plugin (Fiji, NIH, EUA).

Bicelle titrations

Bicelles can be prepared with various lipid types, and the ratio between the long- and short-chain lipids, indicated by the q-value, can be used to modulate the size of bicelles. For solution NMR, bicelles consisting of long-chain 1,2-dimyristoyl-*sn*-glycero-3-phosphocholine (DMPC, C14:0) and short-chain 1,2-diheptanoyl-*sn*-glycero-3-phosphocholine (D7PC, C7:0) with a q-value of 0.2–0.5 are well-validated, providing an optimum balance between membrane-like properties and small size suitable for high-resolution studies. Lipids 1,2-Diheptanoyl-*sn*-glycero-3-phosphocholine (D7PC) and 1,2-Dimyristoyl-*sn*-glycero-3-phosphocholine (DMPC) were purchased from Avanti Polar Lipids (Alabaster, USA). A 870 µM bicelle solution in NMR buffer was prepared as described previously.[86] All NMR experiments were recorded in 20 mM PBS pH 6.4 containing 4 mM DTT at 298 K on Bruker Avance III spectrometers

Please cite this article in press as: Lorenz et al., A fin-loop-like structure in GPX4 underlies neuroprotection from ferroptosis, Cell (2026), https://doi.org/10.1016/j.cell.2025.11.014

operating at 800 or 900 MHz (^{1}H frequency). NMR titration experiments of preformed bicelles to ^{15}N-labeled GPX4^{U46C} and mutants were performed at 100 μM protein concentration with increasing bicelle concentrations in steps of 0.05x, 0.1x, and 0.2x. Spectra were processed in the AZARA software package (v. 2.8, © 1993-2023; Wayne Boucher and Department of Biochemistry, University of Cambridge, UK) and analyzed using CcpNmr Analysis 2.5.[59] The standard deviation of the noise was used to calculate the errors.

Structured illumination microscopy (SIM)

Synthetic red fluorescent protein mScarlet was N-terminally fused to human GPX4 by PCR. The mutants of choice were then introduced with overlap PCR and cloned into pLV-EF1a-IRES-Neo. Individual mutations were confirmed via Sanger sequencing.

Plasma membrane (PM) sheets were prepared as previously described[87–89] with minor modifications. In brief, cells were grown on 1.5 mm coverslips to 80 % confluence. Coverslips were transferred to ice, washed twice with ice-cold PBS+/+ and twice with coating buffer (20 mM MES, 135 mM NaCl, 0.5 mM $CaCl_2$, 1 mM $MgCl_2$, pH 5.5), and incubated with 1 % silica beads in coating buffer for 30 min on ice. After rinsing with deionized water (10 min), a shear force was applied using a syringe held at a 45° angle, followed by thorough washing with PBS+/+. Supported PM sheets were fixed in 4 % formaldehyde and incubated with selected primary (anti-Sodium Potassium ATPase Alpha 1, 1:100, Novus, #NB300-146) and secondary (anti-mouse Alexa Fluor 488, 1:500, Invitrogen, #A11001) antibodies in 1X PBS/1 % BSA. PM sheets were imaged directly after staining. PM sheets were imaged by widefield microscopy and SIM on the Zeiss Elyra S1 (Carl Zeiss) microscope equipped with a 63x 1.4 NA oil objective lens and an Andor iXon 885 EM-CCD camera. Image acquisition was made with five grid rotations, and image reconstruction was made with ZEN software. For density measurements, SIM images were post-processed for the removal of structured artefacts by manual adjustment of the histogram. In FIJI,[90] one fixed-size ROI was made per cell, followed by thresholding and spot analysis in batch. An unpaired t-test was done using GraphPad. For intensity measurements, widefield images were processed in batches using a macro in FIJI to remove background, threshold, and measure spot intensities. Data were transformed to Log10. Its distribution was analyzed, plotted into a histogram, and fit to a sum of two Gaussians in GraphPad.

Neuroproteomic analyses

Serum proteome analysis

Serum samples of TAM-induced *Gpx4*$^{fl/fl}$ and *Gpx4*$^{fl/fl}$*Camk2aCreER*$^{T2+/tg}$ mice were collected on weeks 1, 2 and 4 after TAM and stored as a 100 μL aliquot at -80 °C. In brief, samples were thawed on ice, diluted in lysis buffer (10 mM CAA, 40 mM TCEP, 100 mM Tris pH 8.5), heated at 95 °C for 10 min, and digested with trypsin and LysC proteases (1:100) overnight at 37 °C. Peptides were then acidified with 0.2 % trifluoroacetic acid (TFA) to a final concentration of 0.1 %. Samples were loaded onto C18 Evotips and desalted according to the manufacturer's instructions. Serum samples contain extremely abundant amounts of albumin and IgG, which hinders the capture of low-abundant proteins. We performed the depletion of albumin and immunoglobulins using immunodepleting Resin (R&D, #MIDR002) as instructed in the manufacturer's protocol. Post depletion, samples were processed as mentioned above. Deep serum proteome and spectral library generation samples were desalted on a two-layer 14-micron-gauge styrene divinylbenzene-reversed phase sulfonated (SDB-RPS) StageTips. WT and neuron-specific *Gpx4* knockout samples were pooled separately and fractioned into 16 fractions using a high pH-reversed-phase spider fractionator as described previously.[91] All the samples were measured on an Evosep One LC coupled online to an Exploris 480 mass spectrometer (Thermo Fischer). Peptides were separated on an in-house prepared 8 cm × 150 μm column with 1.9 μm ReproSil-Pur C18-AQ particles (Dr. Maisch) using the 30 SPD method with a gradient length of 44 min. As described, the instrument was operated in DDA mode for library generation and DIA mode for measurements. Further, to quantify circulating serum neurofilaments, we performed affinity purification. In brief, serum samples were thawed on ice, BCA quantified, and 500 μg was diluted in AP buffer (150 mM NaCl, 50 mM Tris (pH 7.5), 5 % glycerol, 1 % IGPAL-CA-630 (Sigma, #I8896), protease inhibitors (EDTA-free, Roche). To the samples, neurofilament antibody (Cell Signalling, #2837) was added and incubated at room temperature for 4 h. Post-incubation protein A/G Sepharose beads were added, incubated further for 2 h on a rotating wheel at 4 °C. To remove non-specific binders, samples were washed three times with wash buffer I (150 mM NaCl, 50 mM Tris (pH 7.5), 5 % glycerol, 0.05 % IGPAL-CA-630) and wash buffer II (150 mM NaCl, 50 mM Tris (pH 7.5)). The proteins bound to beads were digested with Trypsin and Lys-C overnight. Finally, the peptides were desalted on 3-layer C_{18} StageTips, stored at -20 °C until analyzed by LC-MS/MS, and measured as described below in the acquisition strategy.

Label-free cortex proteome sample preparation

Gpx4$^{fl/fl}$ and *Gpx4*$^{fl/fl}$*Camk2aCreER*$^{T2+/tg}$ mouse cortex brain regions were lysed in 1 % SDC buffer (1 % SDC, 100 mM Tris pH 8.5, 40 mM CAA and 10 mM TCEP), incubated on ice for 20 min, boiled at 95 °C, sonicated for 10 min on a Biorupter plus and heated again for 5 min at 95 °C as described previously.[91] Proteins in the sample were digested with LysC (1:100 ratio) for 2 h followed by trypsin (1:100 ratio) for overnight at 37 °C. For the proteome, a 5x volume of isopropanol/1 % TFA was added to the protease-digested samples and vortexed to stop the digestion. The peptides were desalted on equilibrated styrene divinylbenzene-reversed phase sulfonated (SDB-RPS) StageTips, washed once in isopropanol/1 % TFA and twice with 0.2 % TFA. Purified peptides were eluted with 60 μL of elution buffer (80 %, 1.25 % NH_4OH). The dried elutes were resuspended in MS loading buffer (3 % ACN, 0.3 % TFA) and stored at -20 °C until MS measurement. Mouse brain samples, including *Gpx4*$^{R152H/fl}$*Camk2aCreER*$^{T2+/tg}$ mice, were lysed in 1x iST lysis buffer (Preomics, #NC1699272) using the Precellys homogenizer (Bertin Technologies). 20 μg of cell lysate were digested applying the iST Kit from Preomics according to manufacturer's protocol. Acidified samples were speed-vac dried and stored at -20 °C until mass spectrometric measurement.

Please cite this article in press as: Lorenz et al., A fin-loop-like structure in GPX4 underlies neuroprotection from ferroptosis, Cell (2026), https://doi.org/10.1016/j.cell.2025.11.014

Data-dependent acquisition (DDA) of proteome samples

A nanoflow HPLC (EASY-nLC1000, ThermoFisher Scientific) coupled online to an Exploris 480-Orbitrap Mass Spectrometer (ThermoFischer Scientific) via a nanoelectrospray ion source was utilized for the sample analysis. For proteome measurements, 300 ng of peptides were loaded onto a 50-cm column with 75-μM diameter, packed in-house with 1.9 μM C18 ReproSil particles (Dr. Maisch GmbH). 500 ng were loaded for AP-MS samples. The column temperature was maintained using a homemade column oven at 60 °C. The peptides were separated using a binary buffer system consisting of 0.1% formic acid (buffer A) and 60 % ACN plus 0.1 % formic acid (buffer B) at a flow rate of 300 nL/min. Peptides were eluted for 120 min with a 30% buffer B gradient over 95 min, followed by a 5-min increase to 60%. This was followed by a quick ramp up to 95 % over 5 min and declined back to 5 % over 5 min to re-equilibrate the column. Mass spectra were acquired in a data-dependent mode. Briefly, with one full scan at a target of $3e^6$ ions (300-1650 m/z, R = 60,000 at 200 m/z), followed by Top15 MS/MS scans with HCD (high energy collisional dissociation) (target $1e^5$ ions, maximum filling time 28 ms, Isolation window 1.4 m/z, and normalized collision energy 27), detected in the Orbitrap at a resolution of 15,000. Dynamic exclusion 30 s and charge inclusion (2-5) were enabled.

Data-independent acquisition (DIA) of mouse cortex samples

Tryptic peptides were solubilized in 0.1 % formic acid, and equal amounts per sample were measured on a TimsTOF HT mass spectrometer (Bruker) equipped with a CaptiveSpray 2 source online coupled to a Vanquish Neo HPLC (ThermoScientific). Peptides were trapped on a nano-trap column (300-μm inner diameter (ID) × 5 mm, packed with Acclaim PepMap100 C18, 5μm, 100 Å from LC Packings) before separation by reversed-phase chromatography on the analytical column (Aurora 75 μm ID × 250 mm, 1.8 μm from Ionoptics) at 40 °C. Peptides were eluted from the column at a flow of 250 nL/min using a nonlinear 45 min acetonitrile gradient from 3 to 40 % in 0.1 % formic acid. The DIA-Pasef method covered a mass range from 300 to 1,250 m/z and a mobility range from 0.65 to 1.35 1/ko, with a ramp and accumulation time of 100 ms. Precursor peptides were isolated using 34 variable MS/MS windows and 17 MS/MS ramps, resulting in a cycle time of 1.91 sec. Collision energy for 0.6 1/ko was set to 20, and for 1.6 1/ko to 59.

DDA-MS raw data analysis

MS raw files were processed using Maxquant[61] version 1.5.5.2 supported by Andromeda search engine. The data was searched for proteins and peptides using a target-decoy approach with a reverse database against Uniprot mouse (version July 2020, containing 32,273 entries) FASTA file with a false discovery rate of less than 1 % at protein and peptide levels. No changes were made to the enabled default settings, such as carbamidomethyl (C), oxidized methionine (M), and acetylation (protein N-term) as fixed modifications. We set trypsin as the enzyme specificity. A maximum of 2 missed cleavages was allowed, and a minimum peptide length of 7 amino acids was set. The proteins were assigned to the same protein groups if unique peptides could not discriminate between two proteins. The label-free quantification was performed using the MaxLFQ algorithm,[62] and match between run feature was enabled for identifying peptides across runs based on mass accuracy and normalized retention times; for label-free protein quantification minimum ratio count was set to 2. The Maxquant output table was analyzed in Perseus[60]; before the analysis, contaminants marked as reverse hits, contaminants, and only identified by site-modification were filtered out.

DIA-MS raw data analysis

DIA raw files were analyzed using Spectronaut Pulsar (Biognosys, #Sw-3001, version 15.12.210819) using the default settings for a direct DIA analysis or targeted DIA analysis was performed. For plasma samples, a project-specific spectral library encompassing 7828 precursors, corresponding to 1620 proteins and 959 protein groups, was generated utilizing pulser against the mouse Uniprot reference proteome database. The *Mus musculus* Uniprot reference proteome database (version July 2020, containing 32,273 entries) was used. In the case of spectral library matching, Data export was filtered by ‘No Decoy’ and ‘Quantification Data Filtering’ for peptide and protein quantifications.

DIA-MS raw data analysis for the TimsTOF data

Generated measurement files were quantitatively analyzed in the Proteoscape environment (Bruker) using the Spectronaut 19 software (Biognosis) in directDIA using BGS factory settings, allowing for quantification on only proteotypic peptides. Search was performed using the canonical Swissprot Mouse (17061 sequences) database. Normalized protein group quantities were imported in Perseus 2.0.11 software (MPI Martinsried). Abundances were log2-transformed, and the data were filtered to include at least three valid values per protein in the dataset. Missing values were imputed from a normal distribution using default settings. The average quantities per protein per group were calculated and used for ratio calculations. Groups were compared applying a Student’s t-test with (q) and without (p) Benjamini-Hochberg correction.

Proteomic data analysis

The MaxQuant and Spectronaut output files were processed using Perseus version 1.5.2.11 software. Where imputed data is required, the expression data were first filtered to have at least three valid values in each categorical group or at least 80 % valid values. Missing values were imputed using a normal distribution (for serum and global proteome: Gaussian distribution width = 0.5, downshift = 1.5) to provide signals for low-abundance proteins, under the postulation that the low signals are due to the detection limit of the MS measurement. Proteomics data reported in this manuscript is available in the supplement datasheets and raw data is available at ProteomeXchange Consortium with the data identifier PXD071158.

Pre-processing of LC-MS/MS data from Gpx4 knockout

Normalization, filtering and imputation on the log2 scale as well as annotation of LC-MS/MS intensities was performed with help of the Perseus computational platform for proteomics data.[60]

Please cite this article in press as: Lorenz et al., A fin-loop-like structure in GPX4 underlies neuroprotection from ferroptosis, Cell (2026), https://doi.org/10.1016/j.cell.2025.11.014

Preselection of significantly regulated proteins by ANOVA

One-way ANOVA was applied to normalized log2 transformed intensities of proteins from single shot LC-MS/MS measurements of *Gpx4*$^{fl/fl}$*Camk2aCreER*$^{T2+/+}$ (WT) and *Gpx4*$^{fl/fl}$*Camk2aCreER*$^{T2+/tg}$ (KO) mice cortical tissue samples from 1, 2, and 4 weeks after knockout induction containing four replicates for each condition. ANOVA was performed by using the lm function in R statistical software[92] (www.r-project.org), version 4.0.5. Subsequently, the false discovery rate (FDR) calculation according to Benjamini and Hochberg with the R function p.adjust was applied.[93] Proteins with p adj. < 0.05 were preselected for the subsequent PCA analysis and hierarchical clustering.[94] One-way ANOVA was applied to normalized log2 transformed intensities of proteins from measurement in DIA on TimsTOF HT mass spectrometer of *Gpx4*$^{fl/fl}$*Camk2aCreER*$^{T2+/+}$ (WT) and *Gpx4*$^{fl/fl}$*Camk2aCreER*$^{T2+/tg}$ (KO) and *Gpx4*$^{R152H/fl}$*Camk2aCreER*$^{T2+/tg}$ (mutant) mice cortical tissue samples from 4 weeks after knockout induction containing six replicates for each condition. ANOVA was performed by using the lm function in R statistical software[92] (www.r-project.org), version 4.4.1. Subsequently, the false discovery rate (FDR) calculation according to Benjamini and Hochberg with the R function p.adjust was applied.[93] Proteins with p adj. < 0.05 were preselected for the subsequent PCA analysis.

PCA of proteomic samples

Based on the protein levels from shot LC-MS/MS measurements of significantly regulated proteins according to the one-way ANOVA of *Gpx4* KO and WT cortex samples (p adj. < 0.05), a principal component analysis (PCA) was performed using the FactoMineR package in R.[63] For the PCA the data were scaled to unit variance. Based on the protein levels from TimsTOF HT mass spectrometer of significantly regulated proteins according to the one-way ANOVA of *Gpx4* KO, mutant and WT cortex samples 4 weeks after TAM (p adj. < 0.05), a PCA was performed by usage of the FactoMineR package in R. For the PCA the data were scaled to unit variance.

Hierarchical clustering and heat map

Significantly changed protein levels over all experimental conditions (p adj. < 0.05) were represented by a heat map. For the generation of the heat map, we used the Heatmap function within the ComplexHeatmap package (version 2.16.0) in R.[64] Protein levels (rows) were scaled and centered before with the scale function in R and k-means clustering was set on rows (km = 2 within the Heatmap function). Agglomerative hierarchical clustering by the hclust function (method = “ward.D2”) was applied to group experimental conditions (columns) as well as to each row slice of protein intensities (rows) for the heat map. A dendrogram is shown for columns and rows, whereby the dendrogram was reordered.

Enrichment analysis of significantly regulated proteins across all time points

UniProtKB identifier of significantly changed proteins from the one-way ANOVA of *Gpx4* KO and WT cortex samples (p adj. < 0.05) were converted into NCBI gene identifier by using BioMart (GRCm39).[65] Gene IDs were used as input for the GeneRanker program that is based on the ElDorado 04-2021 and Genomatix Literature Mining 01-2021 database.[95] p values, which were calculated according to Fisher’s Exact test, of terms from the category MeSH Disease are shown in Table S1, sheet 4. In the output of the GeneRanker program also the adjusted p value is given which is estimated by the determination of the false positive rate from 1,000 randomly selected genes according to Berriz et al.[96]

T-test of Gpx4 KO versus WT samples

Unpaired two-sided t-test assuming unequal variance was performed on log2 transformed protein intensities of *Gpx4* KO versus WT samples (cortex) from 1, 2, and 4 weeks after TAM, respectively, by using the t.test function in R with the parameter alternative = “two-sided” and var.equal = “FALSE”. Multiple testing correction was applied with the p.adjust function in R to adjust individual p value of each protein by the Benjamini and Hochberg method.[93]

Bar plots

Top-expressed genes were sorted based on their log2 fold change values, and visualized using ggplot2 (version 3.5.2, RRID: SCR_014601) for genes associated with processes (Neurodegeneration, Alzheimer’s disease, and Ferroptosis). The genes associated with these processes are retrieved from the Molecular Signatures Database (MSigDB, RRID: SCR_016863).

Homologous mapping from mouse to human

UniProtKB identifiers of mouse proteins were assigned to UniProtKB identifiers of human by applying homologous mapping with BioMart (GRCm39, GRCh38.p13) via the Protein stable ID.[65] To support the mapping procedure, custom-written Perl scripts were successively applied to exported lists of identifiers from BioMart.

Enrichment analysis of significantly regulated proteins for each time point

Homologous human UniProtKB gene symbols of significantly changed mutant mouse proteins (p adj. < 0.05) from the t-test of *Gpx4* mutant versus WT samples were input into the enricher function of the clusterProfiler (version 4.6.2)[66] for the 4 weeks timepoint. Thereby, the enrichment of significantly regulated proteins in KEGG 2024 pathways, retrieved from the Human MSigDB Collections web page,[67,69] was determined. The resulting p value from a hypergeometric test for each pathway was adjusted by Benjamini and Hochberg using the parameter pAdjustMethod = "BH".

Meta-analysis of published AD proteomic studies

For comparison of significantly changed proteins of *Gpx4*$^{fl/fl}$*Camk2aCreER*$^{T2+/+}$ (WT) versus *Gpx4*$^{fl/fl}$*Camk2aCreER*$^{T2+/tg}$ (KO) cortex samples (2 weeks after TAM) with altered proteins of Alzheimer’s disease patients, a published meta-analysis selecting label-free proteome data from the brain regions frontal and temporal cortices was used.[97] The meta-analysis was performed using the metacont function (package meta, version 6.1-2)[68] based on eight label-free pre-processed datasets of AD patients downloaded from GitHub (https://github.com/hazhay/Meta-analysis_AD), i.e., Datasets 5-8, 12-14, and 16, according to the methodological description by Haytural et al.[97] the meta-analysis was reanalyzed in the following way: a random-effects model was applied, using the DerSimonian and Laird

Please cite this article in press as: Lorenz et al., A fin-loop-like structure in GPX4 underlies neuroprotection from ferroptosis, Cell (2026), https://doi.org/10.1016/j.cell.2025.11.014

method, to consider differences between selected studies, e.g., clinical characteristics of *post mortem* human samples, brain region, and sample preparation. The effect size, defined as the standardized mean difference (SMD) according to Hedges' g between AD and control, was calculated considering the mean of protein intensities for each group, the standard deviation for each group, and the sample size for each group. *p* values were adjusted for multiple testing using the Benjamini-Hochberg method and considered significant at FDR < 0.05.

Comparison of human and mouse data

To investigate the relationship between the proteome of *Gpx4* KO in the cortex of mice and the proteome of AD patients in frontal and temporal cortices, represented by the result of the meta-analysis, a series of comparing analyses were performed: The overlap of significantly changed human proteins (*p* adj. < 0.05) and homologues mouse proteins was determined by Venn diagrams for 1, 2 and 4 weeks after TAM (*p* adj. < 0.05), respectively. The overlap of significantly changed human proteins (*p* adj. < 0.05) and homologues mutant mouse proteins was determined by a Venn diagram for 4 weeks after TAM (*p* adj. < 0.05).

To examine if significantly regulated mouse proteins are overrepresented in the human dataset of the meta-analysis, a pre-ranked fast gene set enrichment analysis (FGSEA) was used.[98] This analysis was carried out separately for up- and downregulated proteins using the fgsea function (package fgsea, version 1.26.0) applied to data ranked by log2(FC)*(-log10(*p*)) of 1, 2, and 4 weeks after TAM (*p* adj. < 0.05), respectively. In addition, the fgsea function was applied to data ranked by log2(FC)*(-log10(*P*)) from up- and downregulated proteins of mutant mice 4 weeks after TAM (*p* adj. < 0.05). Also, the gene set (pathway) file in gmt format for the GSEA function containing the list of differentially expressed proteins from the meta-analysis was restricted to either up- or downregulated proteins (*p* adj. < 0.05).

To study which proteins are commonly significantly up- and downregulated in the *Gpx4* KO according to the t-test, as well as in AD, corresponding to the meta-analysis, scatter plots were generated showing the log2 fold change AD versus control on the y-axis and the log2 fold change *Gpx4* KO versus WT or *Gpx4* mutant versus WT on the x-axis. The log2 fold change is defined as the base 2 logarithm of the ratio of means.

To directly compare the fold change of proteins that are continuously up- or downregulated across the *Gpx4* KO mouse dataset (2 weeks) and the eight human AD datasets, a heatmap was constructed. Proteins that showed opposite directional changes between datasets were excluded from the analysis through application of a custom-written Perl script. For the heat map the pheatmap function of the pheatmap package (version 1.0.12) was used with the parameters clustering_distance_rows = "euclidean" and clustering_method = "ward.D2" resulting in hierarchical clustering of the protein fold changes.

For a deeper insight into changes in the signature of protein expression regarding metabolic and disease pathways between an initial state of the *Gpx4* KO in the mouse, i.e., 2 weeks after induction, and the AD pathogenesis in human, represented by the meta-analysis, GSA was applied separately using the piano package (version 2.16.0).[98] The preparation of both datasets for GSA was treated in the same way concerning the removal of isoforms that did not show the same direction of mean difference. For the human data set, conversion of protein identifier to gene symbols was done through the UniProt Retrieve/ID mapping tool,[99] for the mouse data set the Perseus assigned gene symbols program. In the case of the mouse datasets *Gpx4* KO versus WT (2 weeks) or *Gpx4* mutant versus WT (4 weeks) the log2 fold changes and the *p* values calculated by the t-test per protein were entered into the runGSA function. In contrast, for the human dataset, the mean differences and *p* values computed by the random effects model were used. The KEGG GMT file (version 2019), downloaded from the Enrichr webpage, was used in both cases. Networks with gene sets (nodes) were drawn for the human and the mouse datasets separately using the function networkPlot from the piano package. To investigate which pathways are dysregulated in AD and in consequence of the *Gpx4* KO (2 weeks) or *Gpx4* mutant (4 weeks), the top significantly enriched up and downregulated categories were selected.

Cell type annotation of proteomics data

Weighted gene correlated network analysis (WGCNA) was conducted to identify co-correlating modules that could be assigned to cell types using the *WGCNA* package in R (v4.0.3). Only proteins that were detectable in more than three samples were used. Modules were constructed by signed Pearson's correlation using a soft threshold power 12 corresponding to a scale-free model fit > 0.9 with a minimal module size of 10 proteins per module. Subsequent cell type annotation was performed using enrichment analysis using markers provided by the PanglaoDB. FDR-corrected *p* value < 0.05 was considered significant. Cell type annotation was further confirmed by gene set enrichment analysis (GSEA) of the modules using *clusterProfiler*. Differences in module enrichment among different genotypes were determined by comparing the module eigenvalues at each time point using a generalized linear model, which was corrected for age and sex.

QUANTIFICATION AND STATISTICAL ANALYSIS

The numbers of technical and biological replicates are provided in the figure legends. The *p* values obtained from the one-way ANOVA (Analysis of Variance) followed by Tukey's comparison test are reported. Statistical tests were performed using Python SciPy package v1.9.3. All fields of view from the same fish were pooled together, and each fish is considered as an independent repeat. We used a two-sided unpaired t-test for comparisons between groups with normal distributions or small sample sizes, a two-sided paired t-test for comparisons of the density of CD8+ cells in CRATERs and tumors within the same fish, and a two-sided Mann-Whitney U-test for comparisons between groups with non-normal distributions. $p < 0.05$ was considered significant; *$p < 0.05$, **$p < 0.01$, ***$p < 0.001$.

Supplemental figures

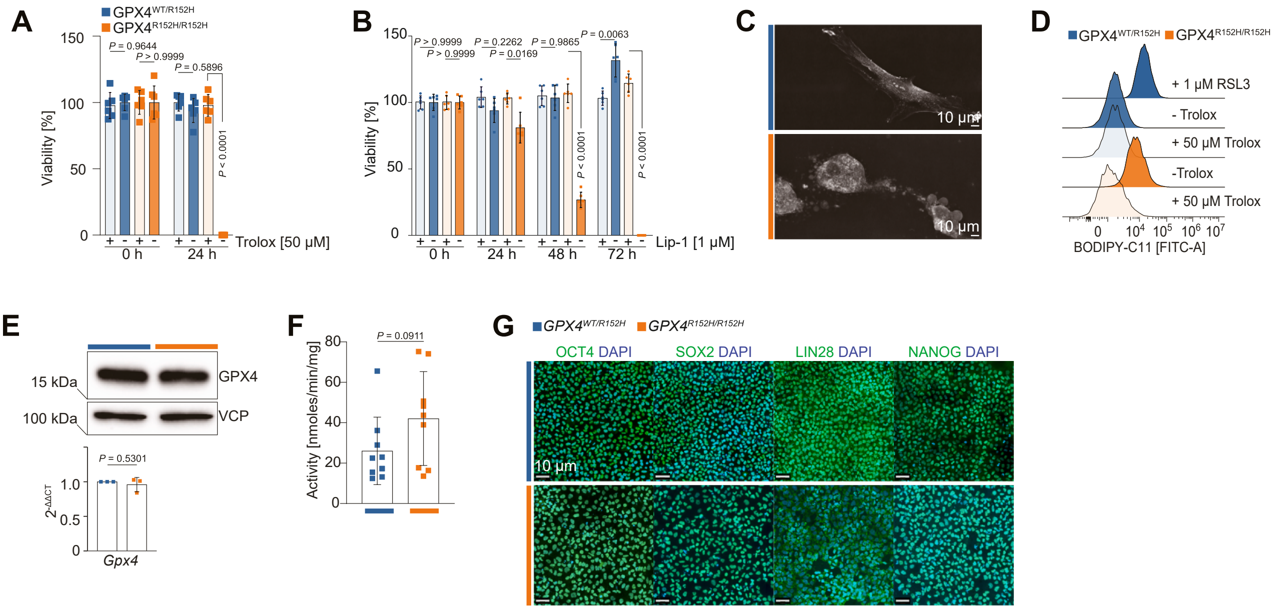

Figure S1. GPX4^{R152H} fails to prevent ferroptosis in cells, related to Figure 1

(A) Viability of primary cells originated from one patient (RAG01) and his parent (RAG02) in the presence or absence of Trolox (50 μM). Results represent at least three independent experiments. A two-way ANOVA followed by a Tukey's post hoc test was performed for statistical analysis. The shaded colors indicate treatment with Trolox, as shown in the figure caption.

(B) Viability of primary cells originated from one patient (RAG01) and his parent (RAG02) in the absence or presence of liproxstatin-1 (Lip-1) (1 μM). The results are representative of at least three independent experiments, and a two-way ANOVA followed by a Tukey's post hoc test was performed. The shaded colors indicate the treatment with Lip-1, as shown in the figure caption.

(C) Representative live-cell imaging recordings from homozygous *GPX4^{R152H}* (RAG01) and heterozygous *GPX4^{R152H}* RAG02 cells. Scale bars (10 μm) are denoted in the figure.

(D) Lipid peroxidation as evaluated by BODIPY 581/591 C11 staining of homozygous *GPX4^{R152H}* (RAG01) and heterozygous *GPX4^{R152H}* (RAG02) cells treated with or without Trolox (50 μM) and RSL3 (1 μM) as a ferroptosis inducer, including control in heterozygous *GPX4^{R152H}* (RAG02) cells.

(E) Representative immunoblot analysis comparing the protein expression of GPX4 and loading control VCP in homozygous *GPX4^{R152H}* (RAG01) and heterozygous *GPX4^{R152H}* (RAG02) cells, and quantitative real-time PCR comparing the relative gene expression of GPX4 in relation to the housekeeping gene *GAPDH* in homozygous *GPX4^{R152H}* (RAG01) and heterozygous *GPX4^{R152H}* (RAG02) cells. Statistical testing was performed using an unpaired Student's *t* test.

(F) GPX4-specific activity measurement in homozygous *GPX4^{R152H}* (RAG01) and heterozygous *GPX4^{R152H}* RAG02 cells as measured using PCOOH as a substrate. Statistical testing was performed using an unpaired Student's *t* test.

(G) Immunofluorescent staining of hiPSCs from homozygous *GPX4^{R152H}* (RAG01) and heterozygous *GPX4^{R152H}* (RAG02) cells for the pluripotency markers octamer-binding protein 4 (OCT4), SRY-box transcription factor 2 (SOX2), Lin-28 homolog A (LIN28), and NANOG. Scale bar indicates 10 μm.

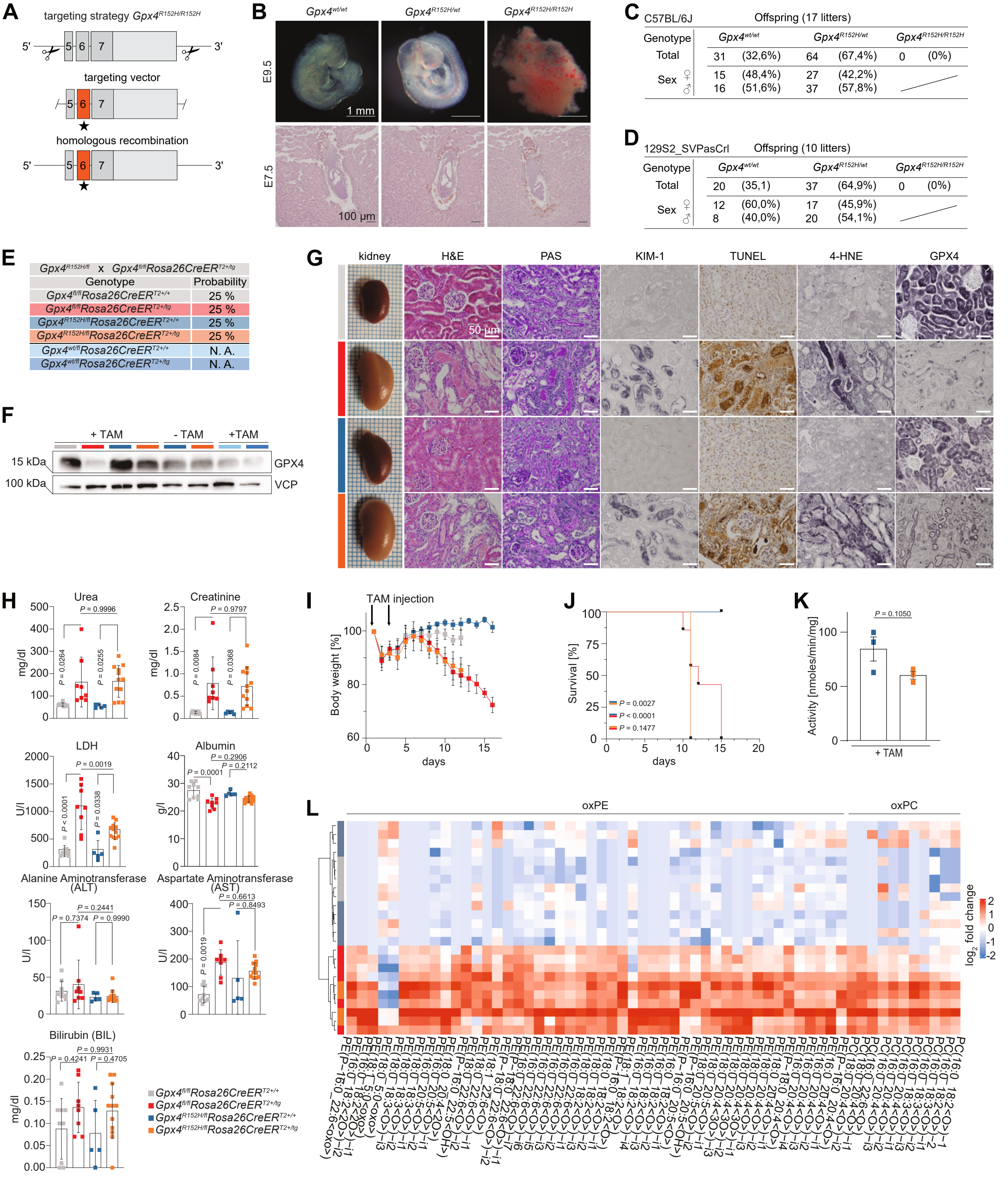

Figure S2. GPX4^{R152H} fails to prevent ferroptosis *in vivo*, related to Figure 1

(A) Gene-targeting strategy to generate mice carrying the murine point mutant (*Gpx4^{R152H}*) corresponding to the human index patients *GPX4^{R152H}*. The exact localization of the murine point mutation is indicated as a star below exon 6.

(B) Analysis of WT, heterozygous, or homozygous *Gpx4^{R152H}* embryos at gestational day 9.5. Homozygous embryos at E9.5 show intrauterine resorption indicating embryonic lethality at an earlier time point. Scale bar depicts 1 mm, as indicated in the figure. Histopathological analysis of H&E-stained paraffin-embedded tissue of embryos at E7.5 confirmed malformations phenocopying embryonic lethality, as observed in *Gpx4$^{-/-}$* embryos.[13]

(legend continued on next page)

(C) Observed absolute and relative numbers of offspring obtained from breedings using *Gpx4*$^{R152H/wt}$ to obtain homozygous *Gpx4*$^{R152H/R152H}$ mice in C57BL/6J background.

(D) Observed absolute and relative numbers of offspring obtained from breedings using *Gpx4*$^{R152H/wt}$ to obtain homozygous *Gpx4*$^{R152H/R152H}$ mice on a 129S2/SvPasCrl/C57BL/6J F1 strain background.

(E) Breeding strategy illustrating the mating of *Gpx4*$^{R152H/fl}$ and *Gpx4*$^{fl/fl}$*Rosa26CreER*$^{T2+/tg}$ to obtain TAM-inducible *Gpx4*$^{R152H/fl}$*Rosa26CreER*$^{T2+/tg}$ KO mice and *Gpx4*$^{R152H/fl}$*Rosa26CreER*$^{T2+/+}$ mice as control.

(F) Representative immunoblot analysis comparing the protein expression of GPX4 and loading control VCP in primary murine renal tissue from the genotypes denoted in the figure, with or without TAM induction of the transgenic allele.

(G) Histopathological analysis of murine kidneys at day 9 after TAM treatment (endpoint analysis). Genotypes are depicted in the figure. From left to right: hematoxylin and eosin (H&E), periodic acid-Schiff (PAS) reaction, kidney injury molecule-1 (KIM-1), TdT-mediated dUTP-biotin nick-end labeling (TUNEL), 4-hydroxynonenal (4-HNE), and GPX4. Scale bars, indicating 10 μm, are denoted within the micrographs.

(H) Evaluation of kidney injury as analyzed by serum levels of urea and creatinine in *Gpx4*$^{fl/fl}$*Rosa26CreER*$^{T2+/+}$, *Gpx4*$^{R152H/fl}$*Rosa26CreER*$^{T2+/+}$, *Gpx4*$^{fl/fl}$*Rosa26CreER*$^{T2+/tg}$, and *Gpx4*$^{R152H/fl}$*Rosa26CreER*$^{T2+/tg}$ mice. Statistical analysis was performed using a one-way ANOVA ($p = 0.0011$) using sample sizes of at least 5 animals per group. Evaluation of kidney injury as analyzed by serum levels of lactate dehydrogenase (LDH), albumin, and liver damage markers aspartate transferase (AST) and alanine aminotransferase (ALT) in *Gpx4*$^{fl/fl}$*Rosa26CreER*$^{T2+/+}$, *Gpx4*$^{R152H/fl}$*Rosa26CreER*$^{T2+/+}$, *Gpx4*$^{fl/fl}$*Rosa26CreER*$^{T2+/tg}$, and *Gpx4*$^{R152H/fl}$*Rosa26CreER*$^{T2+/tg}$ mice. Statistical analysis was performed using a one-way ANOVA using sample sizes of at least 5 animals per group.

(I) Body weight as measured after TAM induction and normalized to the initial body weight. Mice of both sexes were used with $n > 5$ per animal group. *Gpx4*$^{fl/fl}$*Rosa26CreER*$^{T2+/+}$, *Gpx4*$^{R152H/fl}$*Rosa26CreER*$^{T2+/+}$, *Gpx4*$^{fl/fl}$*Rosa26CreER*$^{T2+/tg}$, and *Gpx4*$^{R152H/fl}$*Rosa26CreER*$^{T2+/tg}$.

(J) Survival analysis as depicted by a Kaplan-Meier plot comparing the survival between *Gpx4*$^{fl/fl}$*Rosa26CreER*$^{T2+/+}$, *Gpx4*$^{R152H/fl}$*Rosa26CreER*$^{T2+/+}$, *Gpx4*$^{fl/fl}$*Rosa26CreER*$^{T2+/tg}$, and *Gpx4*$^{R152H/fl}$*Rosa26CreER*$^{T2+/tg}$. Results from statistical analysis are denoted in the figure.

(K) GPX4-specific activity measurement in renal tissue samples obtained from *Gpx4*$^{R152H/fl}$*Rosa26CreER*$^{T2+/+}$ ($n = 3$) and *Gpx4*$^{R152H/fl}$*Rosa26CreER*$^{T2+/tg}$ ($n = 3$) mice using PCOOH as substrate. Statistical testing was performed using an unpaired Student's t test.

(L) Heatmap showing relative amounts of oxidized phosphatidylethanolamines (oxPE) and phosphatidylcholine (oxPC) in renal samples obtained from TAM-induced *Gpx4*$^{fl/fl}$*Rosa26CreER*$^{T2+/+}$ ($n = 5$), *Gpx4*$^{R152H/fl}$*Rosa26CreER*$^{T2+/+}$ ($n = 15$), *Gpx4*$^{fl/fl}$*Rosa26CreER*$^{T2+/tg}$ ($n = 4$), and *Gpx4*$^{R152H/fl}$*Rosa26CreER*$^{T2+/tg}$ ($n = 6$) mice.

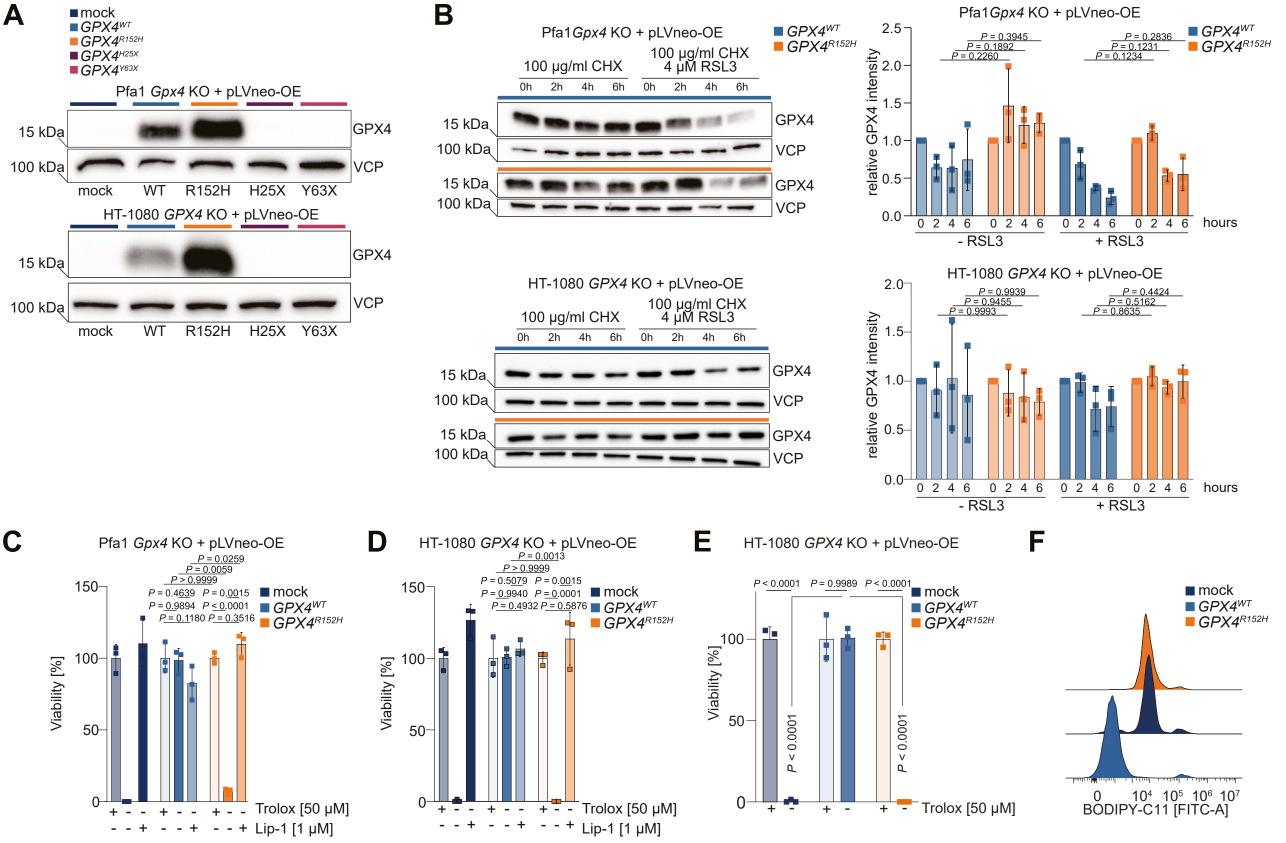

Figure S3. GPX4^{R152H} fails to prevent ferroptosis *in vitro*, related to Figure 1

(A) Representative immunoblot analysis comparing the protein levels of GPX4 and loading control VCP in murine Pfa1 *Gpx4*^{KO} cells transfected with a pLVneo expression vector carrying either a scrambled vector (mock), human WT *GPX4*, human mutant *GPX4*^{R152H}, or constructs of truncating mutations identified in patients with SSMD (*GPX4*^{H25X} mutant or *GPX4*^{Y63X}) lacking GPX4 expression. Representative immunoblot analysis comparing the protein expression of GPX4 and loading control VCP in human HT-1080 *GPX4*^{KO} cells transfected with a pLVneo expression vector carrying either a scrambled vector (mock), WT *GPX4*, mutant *GPX4*^{R152H}, or truncating mutations identified in patients with SSMD (*GPX4*^{H25X} mutant or *GPX4*^{Y63X}), lacking GPX4 expression.

(B) Immunoblot of time-lapsed protein samples obtained during protein stability chase assay incubating murine Pfa1 *Gpx4*^{KO} cells transfected with a pLVneo expression vector carrying either a human WT *GPX4* or human mutant *GPX4*^{R152H} in the presence of cycloheximide, with and without RSL3 (4 μM) as a control. Cells were cultured in the presence of Trolox (50 μM) to prevent cell death. Relative quantification of GPX4 was performed by using the band size of VCP as a loading control. Statistical analysis was performed using a two-way ANOVA and post hoc analysis using Tukey's test.

(C) Viability of murine Pfa1 *Gpx4*^{KO} cells carrying either a scrambled vector (mock), WT *GPX4*, or mutant *GPX4*^{R152H} in the presence or absence of Trolox (50 μM) or Lip-1. Results are representative of at least three independent experiments and statistical analysis was performed using a two-way ANOVA and post hoc analysis using Tukey's test. Shaded colors indicated treatment with Trolox or treatment with Lip-1 after washout of Trolox, as indicated in the figure caption.

(D) Viability of HT-1080 *GPX4*^{KO} cells carrying either a scrambled vector (mock), WT *GPX4*, or mutant *GPX4*^{R152H} in the presence or presence of Trolox (50 μM) or Lip-1. Results are representative of at least three independent experiments and statistical analysis was performed using a two-way ANOVA and post hoc analysis using Tukey's test. Shaded colors indicated treatment with Trolox or treatment with Lip-1 after washout of Trolox, as indicated in the figure caption.

(E) Viability of HT-1080 *GPX4*^{KO} cells carrying either a scrambled vector (mock), WT *GPX4*, or mutant *GPX4*^{R152H} in the presence or absence of Trolox (50 μM). Results are representative of at least three independent experiments and statistical analysis was performed using a two-way ANOVA and post hoc analysis using Tukey's test. Shaded colors indicated treatment with Trolox, as indicated in the figure caption.

(F) Lipid peroxidation was evaluated by BODIPY 581/591 C11 staining of HT-1080 *GPX4*^{KO} cells carrying a scrambled vector (mock), WT *GPX4*, and mutant *GPX4*^{R152H}.

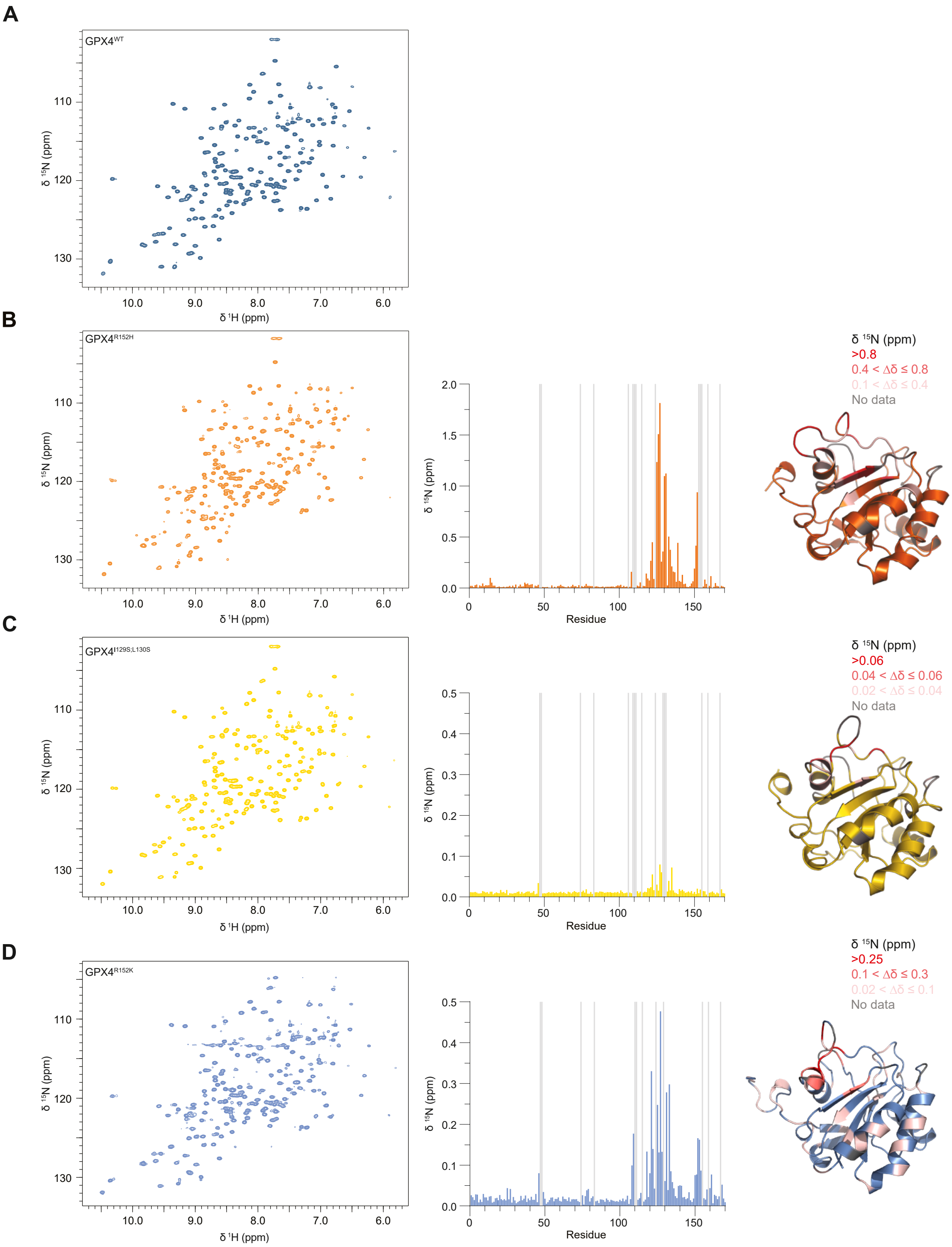

Figure S4. ^{1}H-^{15}N HSQC spectra for WT and mutant GPX4 indicate all proteins are well folded, related to Figures 2 and 3

^{1}H-^{15}N HSQC spectra are shown for (A) $GPX4^{WT}$, (B) $GPX4^{R152H}$, (C) $GPX4^{I129S;L130S}$, and (D) $GPX4^{R152K}$ (left). Chemical shift perturbation (CSP) plots, Δδ, for backbone amide residues are shown relative to $GPX4^{WT}$, indicating that most CSPs map to the polypeptide backbone of the fin-loop region (middle). Gray bars indicate unassigned residues. CSPs are mapped onto the crystal structures of the respective mutants (right). PDB: 2OBI is used for the $GPX4^{WT}$ structure.

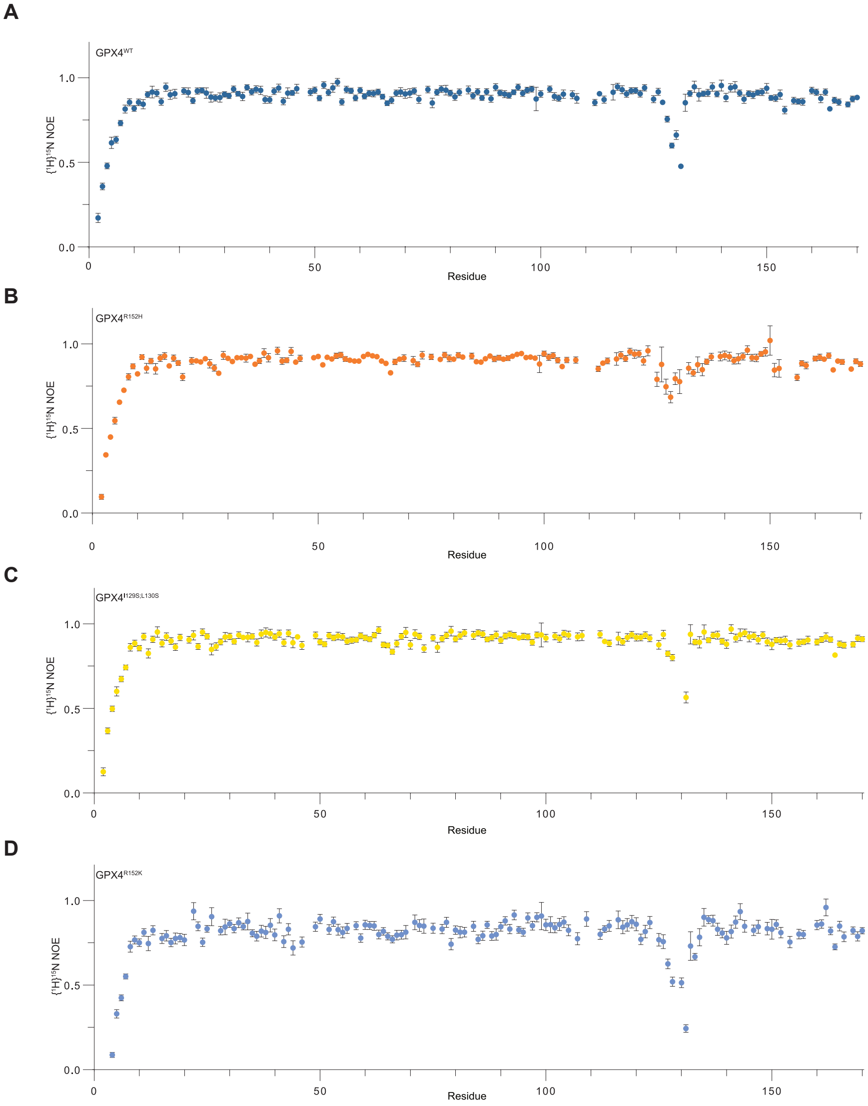

Figure S5. Heteronuclear NOE data indicate a well-structured protein with some regions of fast ps-ns timescale dynamics, related to Figures 2 and 3

$\{^1H\}$-^{15}N Heteronuclear NOE data for backbone amide residues of (A) *GPX4*^{WT}, (B) *GPX4*^{R152H}, (C) *GPX4*$^{I129S;L130S}$, and (D) *GPX4*^{R152K}. The data reveal that all constructs of GPX4 are well structured, showing reduced ps-ns timescale motions (>0.8). Increased flexibility (<0.8) is observed in the fin-loop region of *GPX4*^{WT}, *GPX4*$^{I129S;L130S}$, and *GPX4*^{R152K}. Loop dynamics are reduced in *GPX4*^{R152H} compared with *GPX4*^{WT}, although some faster timescale motions remain.

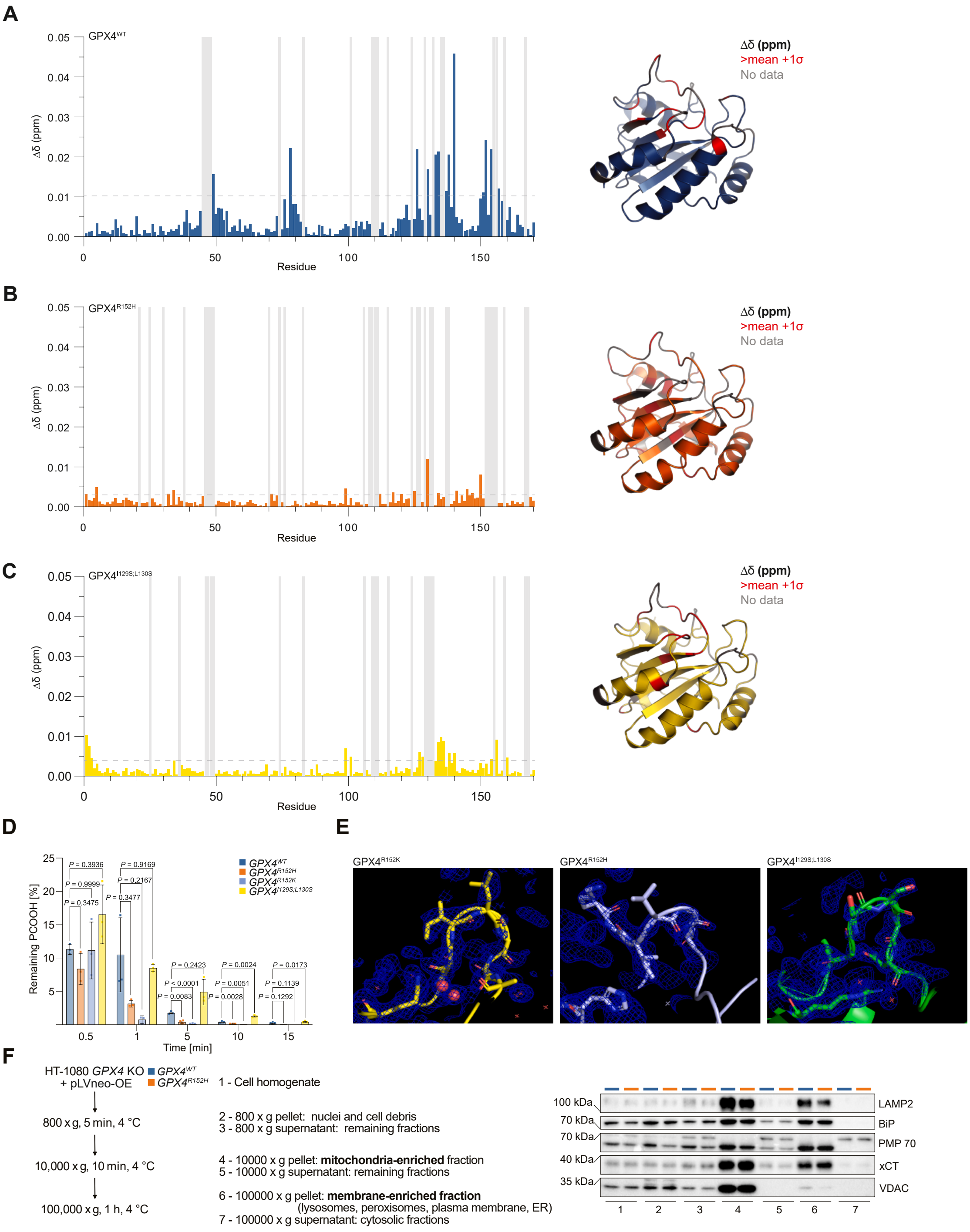

Figure S6. ***GPX4*^{R152H} and *GPX4*$^{I129S;L130S}$ demonstrate inferior bicelle and PM interaction while preserving catalytic activity *in vitro*, related to Figures 2 and 3**

Chemical shift perturbations (CSPs), Δδ, for backbone amide residues between samples with and without 0.05x c7:c14-PC bicelles.

(A–C) (A) GPX4^{WT}, (B) *GPX4*^{R152H}, and (C) *GPX4*$^{I129S;L130S}$. Residues showing a CSP greater than the mean plus one standard deviation are shown on the X-ray crystal structures. PDB: 2OBI is used for the *GPX4*^{WT} structure. The dashed horizontal line on the CSP plots marks the mean + 1σ. Gray bars indicate unassigned residues.

(D) Normalized quantification of remaining PCOOH in the activity reaction mix after indicated incubation time in the presence of *GPX4*^{WT}, *GPX4*^{R152H}, *GPX4*^{R152K}, and *GPX4*$^{I129S;L130S}$ enzymes. All GPX4 mutants show comparable PCOOH-reducing activity to the *GPX4*^{WT} control. Results are representative of three independent experiments, and statistical analysis was performed using a two-way ANOVA and post hoc analysis using Tukey's test.

(legend continued on next page)

(E) Maps showing the electron density at 1 sigma, indicating that the loop can be unambiguously modeled for all the GPX4 mutants.

(F) Graphical representation of subcellular fractionation (left) and immunoblot characterization of the different fractions (right). LAMP2 (lysosomes), BiP (endoplasmic reticulum), VCP (predominantly cytoplasm), PMP70 (peroxisomes), xCT (PM), and VDAC (mitochondria) are characteristic markers of different cellular compartments.

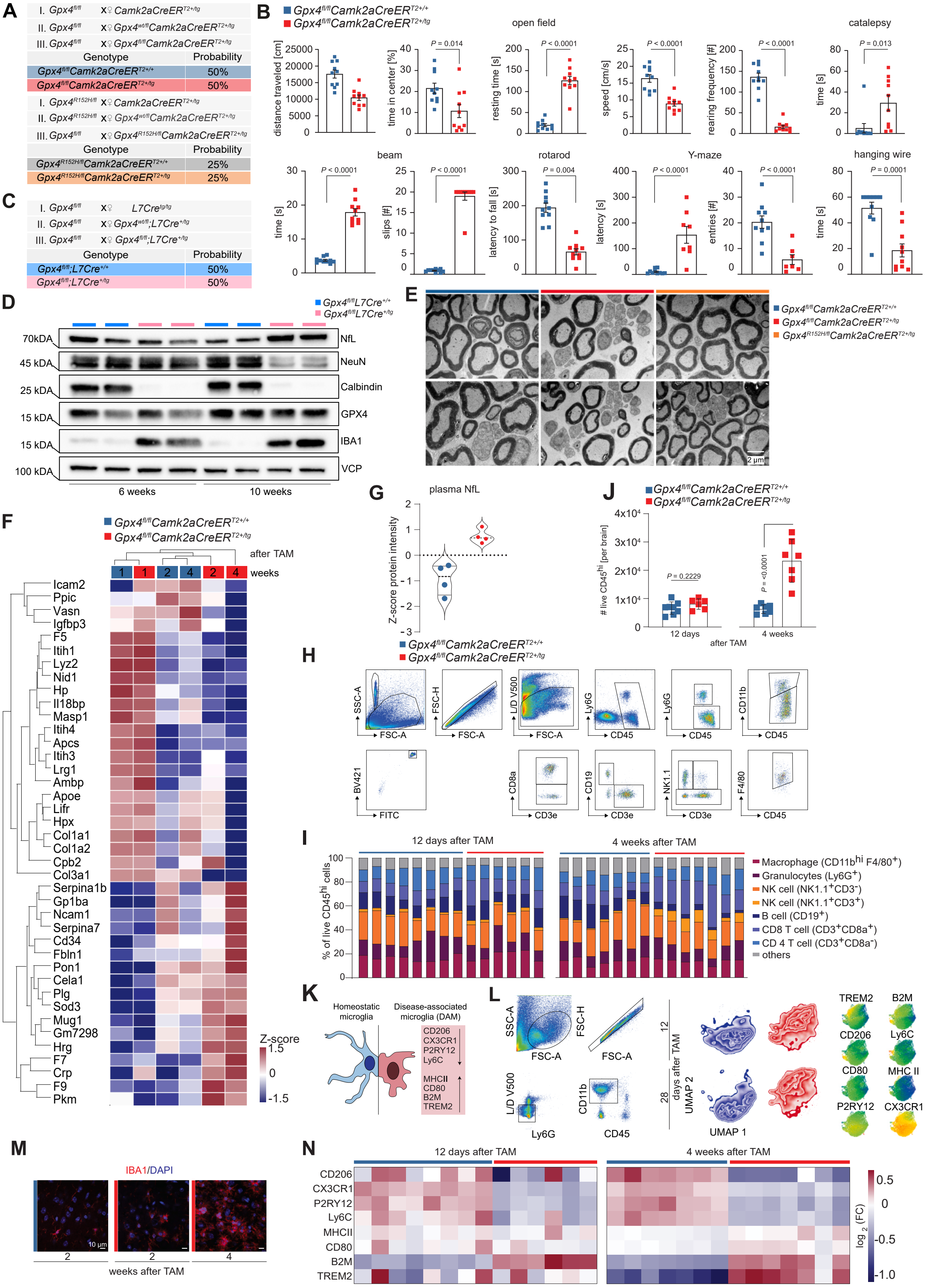

(legend on next page)

Figure S7. Cortical-neuron-specific *Gpx4* loss causes progressive cortical atrophy and neuroinflammation, related to Figures 4 and 5

(A) Breeding strategy to obtain *Gpx4*$^{fl/fl}$*Camk2aCreER*$^{T2+/tg}$ mice and controls by using only CreER^{T2+} females to avoid deletion of the *loxP*-flanked *Gpx4* alleles in the male germline.

(B) Quantification of behavioral parameters of *Gpx4*$^{fl/fl}$*Camk2aCreER*$^{T2+/+}$ and *Gpx4*$^{fl/fl}$*Camk2aCreER*$^{T2+/tg}$ mice 2 weeks after TAM treatment. All data shown represent the mean ± SEM of $n = 10$ animals per genotype. Statistical analysis was performed using unpaired Students' *t* test. Open field analysis includes total traveled distance, time spent in center, resting time, average speed, and rearing frequency. Differences in correcting the positions were recorded by catalepsy bar test. Motoric functions were analyzed by beam test through total time required, and the number of slips, by rotarod performance, measured over three trials as latency to fall and hanging wire test. Y-maze analysis was measured with respect to an increased latency time and numbers of entries.

(C) Breeding strategy to obtain *Gpx4*$^{fl/fl}$*L7Cre*$^{+/tg}$ mice and controls by using only CreER^{T2+} females to avoid deletion of the *loxP*-flanked *Gpx4* alleles in the male germ line.

(D) Representative immunoblot analysis comparing the protein expression of NfL, NeuN, calbindin, GPX4, IBA1, and loading control VCP in *Gpx4*$^{fl/fl}$*L7Cre*$^{+/tg}$ mice compared with WT controls of 6 and 10 weeks of age.

(E) Representative transmission electron microscopy (TEM) images from sciatic nerve samples obtained from *Gpx4*$^{fl/fl}$*Camk2aCreER*$^{T2+/+}$ and *Gpx4*$^{fl/fl}$ *Camk2aCreER*$^{T2+/tg}$ mice, and *Gpx4*$^{R152H/fl}$*Camk2aCreER*$^{T2+/tg}$, showing no apparent damages to peripheral nerve integrity.

(F) Significantly changed protein levels in a heatmap represent overall conditions (one-way ANOVA). The hierarchical clustering of conditions is displayed by the dendrogram on the top, while the dendrogram on the left shows the clustering of the protein levels.

(G) Quantification of proteomic measure of NfL levels in serum of *Gpx4*$^{fl/fl}$*Camk2aCreER*$^{T2+/+}$ and *Gpx4*$^{fl/fl}$*Camk2aCreER*$^{T2+/tg}$ mice.

(H) Gating strategy for the identification of infiltrating immune cells in total hemispheres of *Gpx4*$^{fl/fl}$*Camk2aCreER*$^{T2+/+}$ and *Gpx4*$^{fl/fl}$*Camk2aCreER*$^{T2+/tg}$ mice. After duplet exclusion by scatter properties, viable leukocytes were classified as V500 viability stain CD45^{hi}. 123 count eBeads were detected using their fluorescence in the BV421 and FITC detector. Uniform manifold approximation and projection (UMAP) algorithm-aided clustering of microglia cell population based on the surface expression of TREM2, B2M, CD206, Ly6C, CD80, MHC class II, P2RY12, and CX3CR1. Gating strategy for the identification of microglia in total hemispheres of *Gpx4*$^{fl/fl}$*Camk2aCreER*$^{T2+/+}$ and *Gpx4*$^{fl/fl}$*Camk2aCreER*$^{T2+/tg}$ mice. After duplet exclusion by scatter properties, viable microglia were classified as V500 viability stain CD11b^{+} CD45^{low}.

(I) Distribution of immune cell populations in total hemispheres isolated from *Gpx4*$^{fl/fl}$*Camk2aCreER*$^{T2+/+}$ and *Gpx4*$^{fl/fl}$*Camk2aCreER*$^{T2+/tg}$ mice, as measured by flow cytometry and shown as percentual fraction based on the total leukocytes (CD45^{hi}). Time points of analysis after TAM induction are indicated in the figure caption. Immune cell populations, as defined by the gating strategy, are denoted in the figure.

(J) Total numbers of viable CD45^{+} cells isolated from *Gpx4*$^{fl/fl}$*Camk2aCreER*$^{T2+/+}$ and *Gpx4*$^{fl/fl}$*Camk2aCreER*$^{T2+/tg}$ mice, as measured by flow cytometry from total hemispheres. Statistical analysis was performed using unpaired Students' *t* test, $n > 5$ per genotype.

(K) Graphical illustration of the change in marker gene expression of microglia transitioning from unchallenged homeostatic microglia to disease-associated activated microglia (DAM).

(L) Flow cytometry gating strategy to assess microglial polarization.

(M) Representative confocal images of the cortical region stained with the microglia marker IBA1. Scale bar indicates 10 μm.

(N) Heatmap showing the relative intensity of expression of microglia activation markers related to homeostatic microglia or DAMs, as measured according to (K).

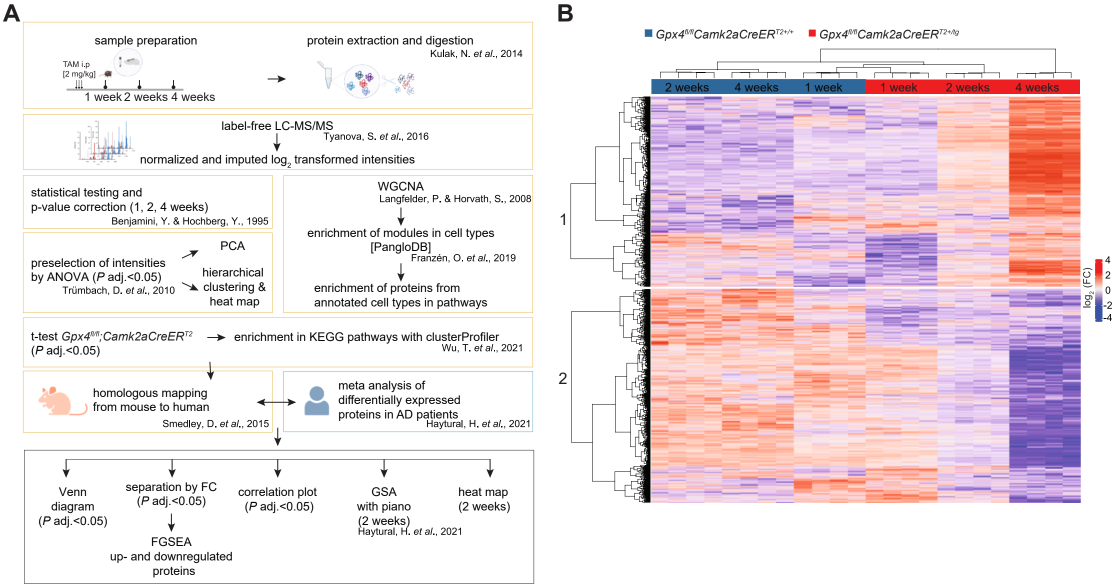

Figure S8. A longitudinal neuroproteomic survey of neuron-specific *Gpx4* KO brains, related to Figure 5

(A) Flowchart depicting the workflow of neuroproteomic analysis of cortical tissues of *Gpx4*$^{fl/fl}$*Camk2aCreER*$^{T2+/+}$ and *Gpx4*$^{fl/fl}$*Camk2aCreER*$^{T2+/tg}$ mice at the indicated time points. In brief, after sample preparation, label-free proteomic analysis was performed, yielding absolute protein expression values, which were normalized and transformed before statistical analysis, as indicated in the figure. Murine-based proteomic results (marked in red) were compared with proteomic signatures in human cortical samples (marked in blue), as shown.

(B) 2,952 significantly changed protein levels across all conditions (one-way ANOVA) are shown in a heatmap. Hierarchical clustering of conditions is shown in the dendrogram at the top, while clustering of protein levels is shown in the dendrogram on the left. Samples of *Gpx4*$^{fl/fl}$*Camk2aCreER*$^{T2+/tg}$ mice 4 weeks after TAM injection clearly separate from all other conditions. The corresponding high protein levels (indicated by red color) of *Gpx4*$^{fl/fl}$*Camk2aCreER*$^{T2+/tg}$ at 4 weeks group together within subtree 1, while low protein levels (indicated by blue color) group together within subtree 2 of the dendrogram shown on the left.

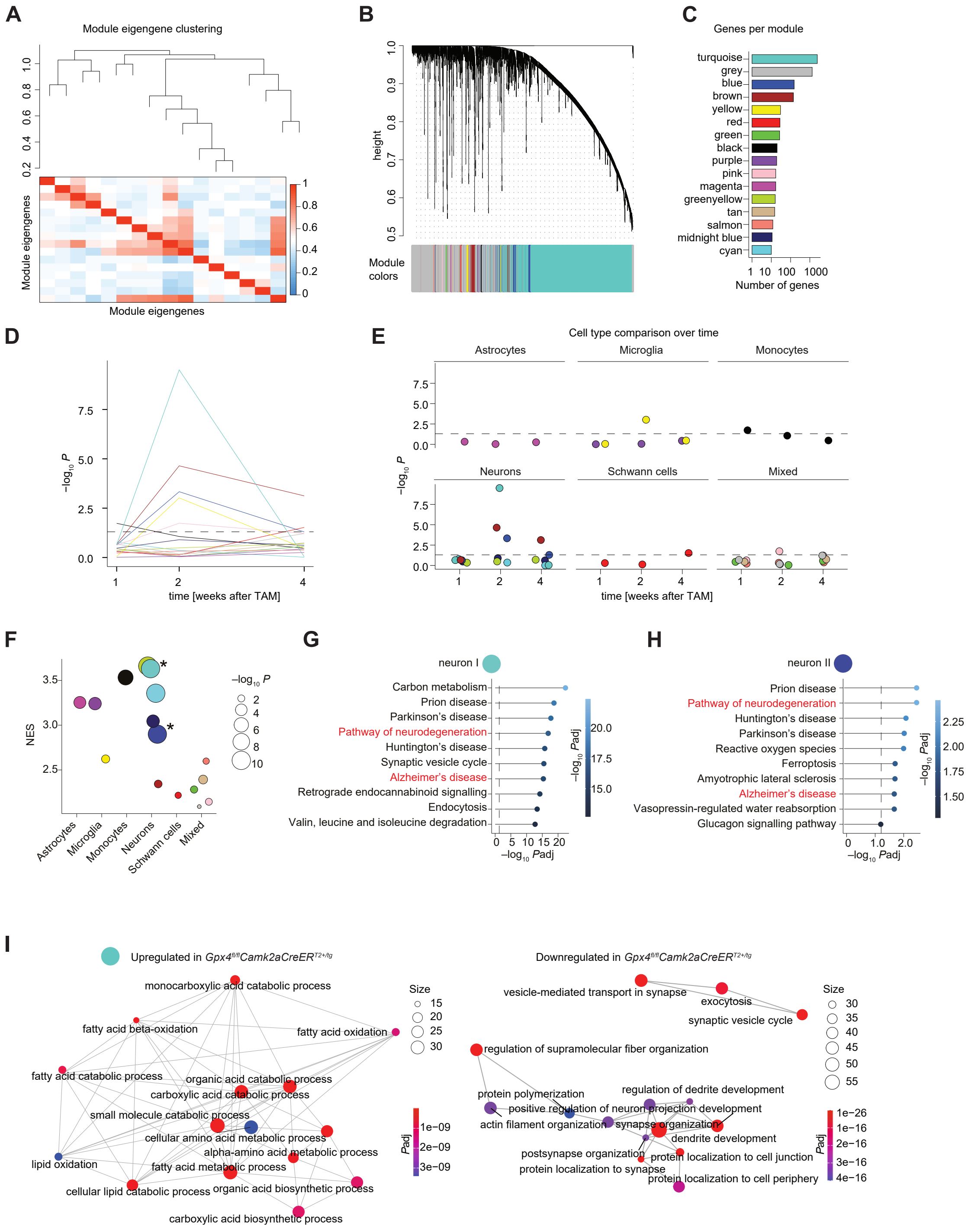

Figure S9. WGCNA analysis reveals neuron-specific changes reminiscent of neurodegeneration, related to Figure 5

(A) Weighted gene correlation analysis (WGCNA) was performed using whole-brain proteomics of *Gpx4*$^{fl/fl}$*Camk2aCreER*$^{T2+/+}$ and *Gpx4*$^{fl/fl}$*Camk2aCreER*$^{T2+/tg}$ mice at different time points after TAM injection. The eigengene correlation matrix and hierarchical tree clustering are shown.

(B) Module color annotation and gene hierarchical tree clustering of the WGCNA analysis are depicted.

(C) The number of genes per module is shown. Only modules that could be clearly annotated by cell types and that are differentially regulated between *Gpx4*$^{fl/fl}$*Camk2aCreER*$^{T2+/+}$ and *Gpx4*$^{fl/fl}$*Camk2aCreER*$^{T2+/tg}$ mice are shown.

(D) Comparison of modularity for each module, which could be clearly annotated by cell types between *Gpx4*$^{fl/fl}$*Camk2aCreER*$^{T2+/+}$ and *Gpx4*$^{fl/fl}$*Camk2aCreER*$^{T2+/tg}$ mice at different time points after TAM injection. *y* axis shows −log10 *p* values of linear models, which were used to determine differences between genotype modularity.

(legend continued on next page)

(E) Comparison of modularity for each module between *Gpx4*$^{fl/fl}$*Camk2aCreER*$^{T2+/+}$ and *Gpx4*$^{fl/fl}$*Camk2aCreER*$^{T2+/tg}$ mice at different time points after TAM injection, separated by cell types. *y* axis shows −log10 *p* values, dashed lines represent −log10 *p* value of 0.5.

(F) Differences in cell type enrichments from bulk cortical proteomics data of *Gpx4*$^{fl/fl}$*Camk2aCreER*$^{T2+/+}$ and *Gpx4*$^{fl/fl}$*Camk2aCreER*$^{T2+/tg}$ mice. Modules were determined by weighted gene correlated network analysis (WGCNA); *y* axis shows normalized enrichment scores (NESs) of cell type signatures; size represents −log10 *p* values of linear models that were used to determine differences between genotype modularity. Only modules with significant enrichment for cell types are shown.

(G) KEGG pathway enrichment analysis of the neuronal module "dark turquoise," which is significantly driven due to the absence of *Gpx4*. Color and *y* axis show −log10 *p* values.

(H) KEGG pathway enrichment analysis of the neuronal module "dark blue," which is significantly driven due to the absence of *Gpx4*. Color and *y* axis show −log10 *p* values.

(I) Gene Ontology (GO) term analysis of proteins that were included in the neuronal module dark turquoise and were upregulated (left) or downregulated (right) in the initial proteomics screening in cortices of *Gpx4*$^{fl/fl}$*Camk2aCreER*$^{T2+/tg}$ mice in comparison to *Gpx4*$^{fl/fl}$*Camk2aCreER*$^{T2+/+}$ mice.

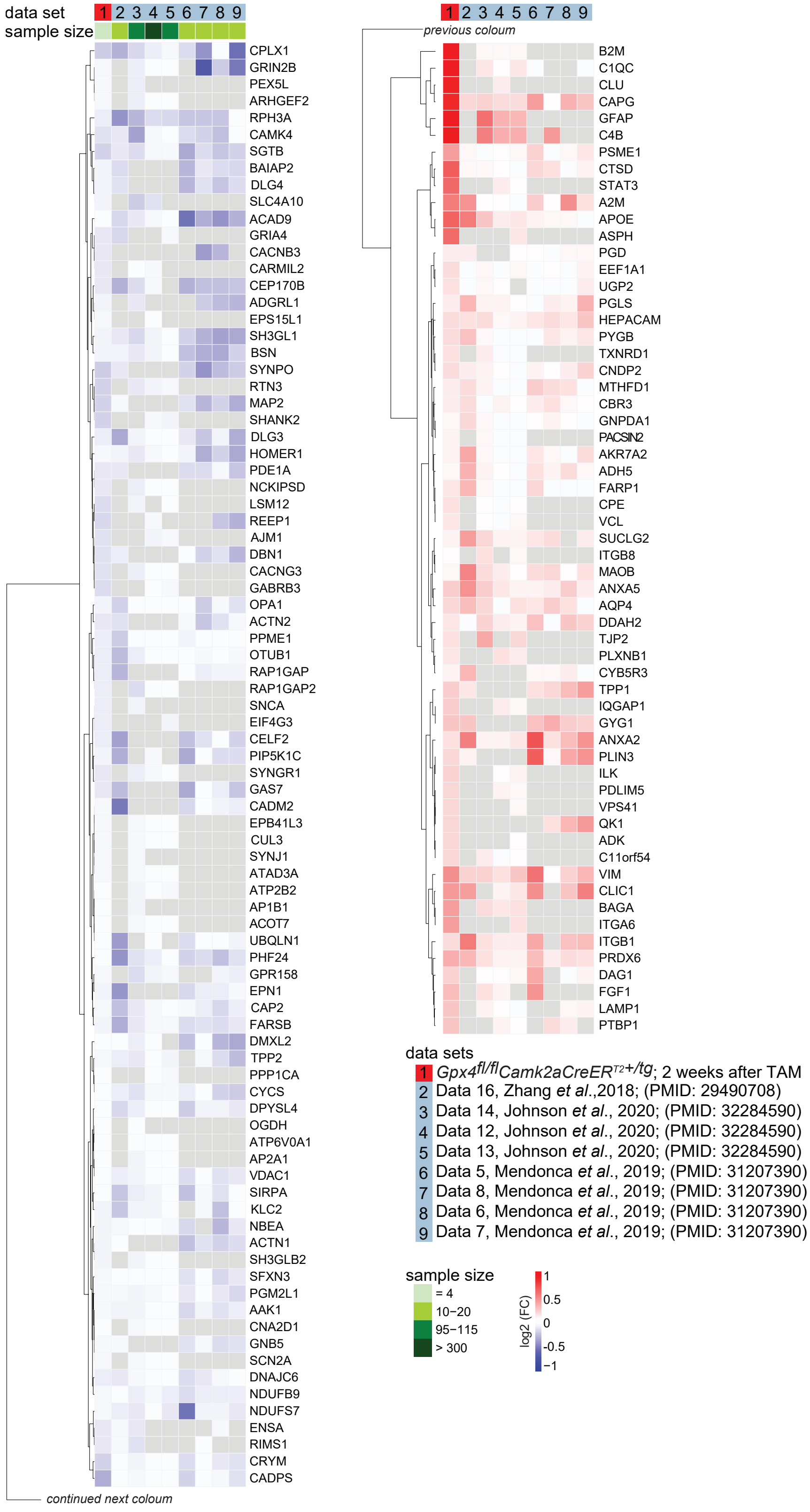

(legend on next page)

Figure S10. Meta-analysis of human and mouse proteomic data, related to Figure 5

Heatmap of the $\log_2$ FC (with p adj. < 0.05) for 145 proteins that are continuously up- or downregulated across the *Gpx4*$^{fl/fl}$*Camk2aCreER*$^{T2+/tg}$ mouse dataset, 2 weeks after KO induction, and eight humanAD versus control datasets from the meta-analysis.